POLITECNICO DI TORINO

Department of Mechanical Engineering

Master's Degree Thesis

Numerical simulation of turbulent non-premixed flames

Supervisors

Prof.ssa Daniela Anna Misul

Prof. Mirko Baratta

Prof. Simone Salvadori

Candidate

Miraidin Safavi

A.Y. 2019/2020

Abstract

It is almost two centuries that we are using fossil fuels as our main energy source. Within the last fifty years, the consumption of fossil fuels, and consequently the pollution caused by the combustion process increased drastically which and led to serious environmental and health issues. Controlling these pollutants and reducing them is our only key to survival.

The main goal of this thesis is to create a comprehensive 3D CFD model using the commercial software ANSYS FLUENT based on the available database of the University of Sidney on a bluff-body burner using CH_4/H_2 as fuel. The computed results have been compared with measured temperature, mean mixture fraction, and species mass fraction. The model is based on the non-premixed combustion by getting advantage of the steady flamelet model and the chemical equilibrium combustion model. The realizable $k-\varepsilon$ model is modified by changing the ε equations constant, and the results are compared with the Standard model to investigate the turbulence model's effect on the numerical predictions. In order to model the combustion, a detailed kinetic library of methane is used to mimic the methane combustion and NOx formation as close as possible to the real combustion process, and the combustion model sensitivity is measured. The whole developed model is applied to another flame with different blow-off velocity, and the results are compared with experimental data.

The studies performed and reported in this work suggest that the realizable $k-\varepsilon$ combined with the steady flamelet model can predict the combustion with a high degree of accuracy.

Contents

1. Introduction 1

1.1 An Overview of non-premixed Combustion 1

1.2 Bluff-body Burner 3

1.3 The Objective of This Thesis Work 3

2. Theory 4

2.1 Mass Conservation Equation 4

2.2 Momentum Conservation Equations 4

2.3 Energy Conservation Equation 5

2.3.1 Energy Equation in Solid Regions 6

2.4 Turbulence 7

2.4.1 Reynolds Averaging 8

2.4.2 $\boldsymbol{k-\varepsilon}$ Model 9

2.5 Combustion Modeling 13

2.5.1 Chemical Equilibrium 13

2.5.2 Steady Diffusion Flamelet Model 14

2.5.3 Mixture Fraction 14

2.5.4 Transport Equations for the Mixture Fraction 15

2.5.5 Flamelet Concept 16

2.5.6 The Energy Equation for the Non-Premixed Combustion Model 16

2.5.7 Relationship of Mixture Fraction to Species Mass Fraction, Density and Temperature 17

2.5.8 Description of the Probability Density Function 17

2.5.9 Derivation of Mean Scalar Values from the Instantaneous Mixture Fraction 18

2.5.10 Reaction Mechanism 20

2.5.11 Chemical Kinetics 20

2.6 Methane Combustion 21

2.7 NOx Model 22

2.8 Boundary Conditions 23

2.9 Solver 24

2.9.1 Coupled Pressure-Velocity 24

2.9.2 Least Square Cell-Based 26

2.9.3 Second-Order Upwind 26

2.10 Temporal Solution 27

2.10.1 Implicit Time Stepping (Pseudo Transient) 27

2.11 Meshing 28

3. Bluff-Body Burner 30

3.1 Geometry and Boundary Conditions 31

3.2 Flame Characteristic 33

3.3 Measurements 36

3.4 Measurements Uncertainty 37

4. CFD Model and Results 39

4.1 Geometry and Mesh 39

4.2 Mesh optimization 40

4.3 The velocity profile in the jet outlet 45

4.4 Study using the default realizable k-e model 46

4.5 Optimization of the realizable k-e model 47

4.6 Comparison between the Standard and Realizable k-e model 53

4.7 Comparing The Flamelet Model With The Equilibrium Model 60

4.8 HM2 flame 75

4.9 Comparison of HM1 and HM2 flames 88

5. Conclusion and Recommendations 90

6. Bibliography 91

List of Figures

Figure 1.1 Visualization of the methane-air combustion. 2

Figure 2.1 Comparison of the temperature contours of RANS and LES models, against the experimental data from Sandia National Laboratory.[4] 8

Figure 2.2 Graphical Description of the Probability Density Function 18

Figure 2.3 Logical Dependence of Averaged Scalars on Mean Mixture Fraction, the Mixture Fraction Variance, and the chemistry Model (Adiabatic, Single-Mixture-Fraction Systems) 19

Figure 2.4 Coupled based algorithm 25

Figure 2.5 Cell centroid evaluation. 26

Figure 2.6 Graphical representation of an optimal cell (in green). 29

Figure 3.1 Schematic drawing of a bluff-body combustor and measuring locations. 31

Figure 3.2 View of the HM bluff-body burner 32

Figure 3.3 Flame characteristics 32

Figure 3.4 Flow characteristics of the natural gas diffusion flame stabilized by a bluff-body 34

Figure 3.5 Blow-off limits for the natural gas turbulent diffusion flame stabilized by a bluff body 35

Figure 3.6 Schematic of the experimental test setup for the piloted flame burner at the Sandia Combustion Research Facility 36

Figure 3.7 Errors associated to different species 37

Figure 4.1 Contours of the mesh size. 42

Figure 4.2 Convergence plots for the mesh optimization studies..... 42

Figure 4.3 Mesh size and the solving time. 43

Figure 4.4 Contours of mean mixture fraction for different mesh densities (coarse mesh left). 44

Figure 4.5 Contours of temperature for different mesh densities (coarse mesh left). 44

Figure 4.6 Contours of TKE for different mesh densities (coarse mesh left)..... 45

Figure 4.7 Velocity profile of the fuel jet for the HM1-HM2 flame. 46

Figure 4.8 Temperature contour of the default(left) and modified K-epsilon model. 48

Figure 4.9 Mean mixture fraction contour of the default(left) and modified K-epsilon model. 48

Figure 4.10 Radial profile of the mean mixture fraction.(modified and default turbulence model). 49

Figure 4.11 Radial profile of the temperature.(modified and default turbulence model)..... 50

Figure 4.12 Radial profile of axial velocity.(modified and default turbulence model). 51

Figure 4.13 Radial profile of the radial velocity.(modified and default turbulence model)..... 52

Figure 4.14 Radial means of mean mixture fraction..... 54

Figure 4.15 Readial mean of temperature. 55

Figure 4.16 Radial means of the axial velocity. 56

Figure 4.17 Radial means of the radial velocity. 57

Figure 4.18 Mean mixture fraction contour. Realizable-Standard k-epsilon model. 58

Figure 4.19 Temperature contour. Realizable-Standard k-epsilon model. 58

Figure 4.20 Turbulent energy dissipation contour. Realizable-Standard k-epsilon mode. 59

Figure 4.21 Turbulent kinetic energy contour. Realizable-Standard k-epsilon mode 59

Figure 4.22 Mean mixture fraction contour (left flamelet model and right chemical equilibrium model). 61

Figure 4.23 Temperature contour (left flamelet model and right chemical equilibrium model). 62

Figure 4.24 Radial profile of the mean mixture fraction in the HM1 flame. 63

Figure 4.25 Radial profile of the temperature in HM1 flame. 64

Figure 4.26 Radial profile of the axial velocity in HM1 flame. 65

Figure 4.27 Radial profile of the radial velocity in HM1 flame. 66

Figure 4.28 Radial profile of the O2 in HM1 flame. 67

Figure 4.29 Radial profile of the N2 in HM1 flame. 68

Figure 4.30 Radial profile of the H2 in HM1 flame. 69

Figure 4.31 Radial profile of the H2O in HM1 flame. 70

Figure 4.32 Radial profile of the CO in HM1 flame. 71

Figure 4.33 Radial profile of the CO2 in HM1 flame. 72

Figure 4.34 Radial profile of the OH in HM1 flame. 73

Figure 4.35 Radial profile of the NO (×100) in HM1 flame. 74

Figure 4.36 Temperature contour of the HM2 flame. 77

Figure 4.37 Temperature contour of the recirculation zone in HM2 flame. 77

Figure 4.38 Radial profile of the mean mixture fraction in the HM2 flame. 78

Figure 4.39 Radial profile of the temperature in the HM2 flame. 79

Figure 4.40 Radial profile of the O2 in the HM2 flame. 80

Figure 4.41 Radial profile of the N2 in the HM2 flame. 81

Figure 4.42 Radial profile of the H2 in the HM2 flame. 82

Figure 4.43 Radial profile of the H2O in the HM2 flame. 83

Figure 4.44 Radial profile of the CO in the HM2 flame. 84

Figure 4.45 Radial profile of the CO2 in the HM2 flame. 85

Figure 4.46 Radial profile of the OH in the HM2 flame. 86

Figure 4.47 Radial profile of the NO (×100) in HM2 flame 87

Figure 4.48 Recirculation zone. (HM2-HM1) 88

List of Tables

Table 2-1 Zeldovich mechanism in units of mol, cm, s, kJ and K. 22

Table 2-2 Solution methods. 24

Table 4-1 Different mesh profiles. 41

1. Introduction

Nowadays by increasing the mobilization, population, and industries the demand to produce energy is increased. This increase in energy production raised some serious concerns regarding the environment so parallel to it, the demand for optimizing and increasing the efficiency of the energy production process became crucial.

Most of the energy is produced from gaseous hydrocarbons. The advantage of using this type of fuel compared to others for example liquid fuels such as oil is their easy, and relatively clean combustion process. However, getting advantage of gaseous fuels causes some products with a negative impact on a global scale such as CO_2 as the main reason behind global warming and NO_x products which are responsible for acid rains and pollution.

A very detailed understanding of the turbulent combustion process is very useful to control these pollutants and increase efficiency.

1.1 An Overview of non-premixed Combustion

Non-premixed combustion is defined as a combustion process with two separate pathways of fuel and oxidizer. This type of flames is used in very vast fields of industrial and practical cases, mainly due to its characteristics which makes it easy to control and reduce life hazards. With existing concerns over pollutants, this advantage turns into a drawback due to the lower control over the combustion process for lower emissions. For example, in the industrial cases of heavy-duty gas turbines, a method is employed to create a partially premixed zone in the reactor.

Because of the advantages of non-premixed combustion, there are many different types of applications such as liquid spray burning in diesel engines, stabilized flames using the recirculation zone created by flow over a wall or bluff-body, and recently the application of H_2 as fuel.

The observations are showing that the non-premixed combustions are controlled by their turbulence behavior with fuzzy edges. Donbar et al. [1] have found that in the turbulent non-premixed flames the reaction zone separates with a very thin layer similar to those of laminar flames. Figure 1.1 Visualization of the methane-

air combustion. shows how the sheer layers are translating through the combustion zones. This behavior creates serious issues in controlling the pollutants. For this reason, having a good estimation of the flow field is the key to understanding the combustion behavior.

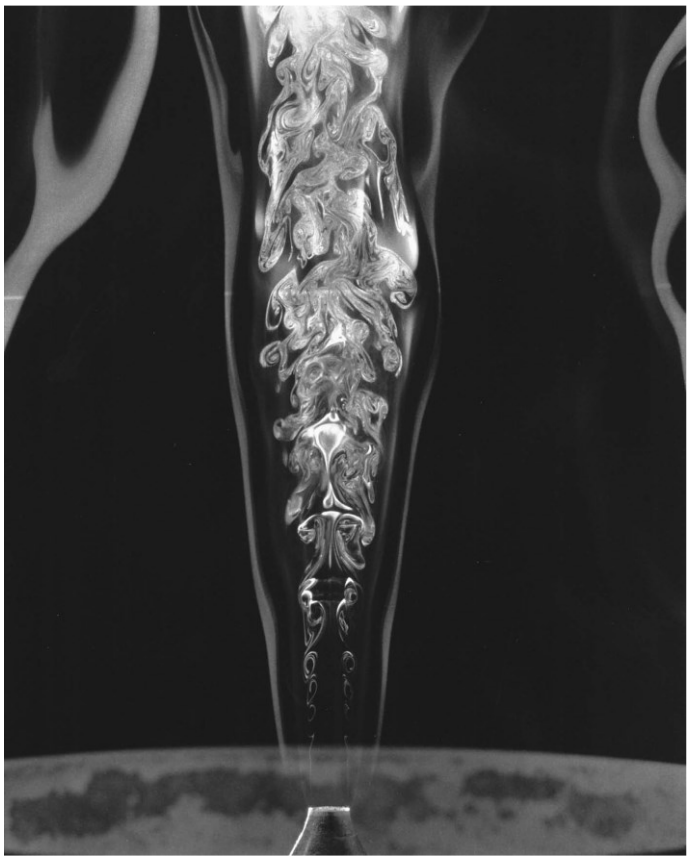

Figure 1.1 Visualization of the methane-air combustion.

if the velocity of the fuel increases the flames start to lift. To understand the criteria for blow-off limits in the case of stabilized non-premixed flames three main theories are provided:

1. The flow velocity at the blow-off position is high enough that the laminar flame is higher than the burning premixed flow.
2. The strain rate exceeds the extinction of the laminar flame.
3. The times required to mix, the fuel and oxidizer are lower than the governing kinetics of the combustion.

So having a good estimation of the decay rate which depends on the type of flames and the kinetic library has a noticeable significance.[2]

1.2 Bluff-body Burner

Numerical modeling of the turbulent flames at the first sight seems to be easy and straight forward. For all the flows there is a need to consider the governing transport, energy, and species equations next to a chemical kinetic library, but it is not as simple as it seems. Despite all, the main challenge is to modify and optimize the turbulence models. Modification and development of the CFD codes are not possible without the data derived from firm and acceptable experiments. Bluff-bodies are the best candidate for these developments.

Measuring the data from a combustion process is not an easy task to do. To develop a reliable measurement it is required o stabilize the flames. Due to the wake which is created over the face of the bluff-body, a stabilized flame can shape.

The University of Sidney created a good database of flames over bluff-bodies which is used in this thesis work.

1.3 The Objective of This Thesis Work

This thesis work has four main objectives:

1. Examine the previously provided turbulence models over a stabilized bluff-body burner.
2. Provide a better estimation of the flow field using the commercial CFD software ANSYS FLUENT.
3. Comparison of the results of different turbulence models and combustion models.
4. Use the results to model and examine the existing NOx model.

2. Theory

For every flow, conservation equations for mass and momentum in time and space must be solved. For flows that are involved in any type of energy change that can affect the flow, heat transfer, or flows with compressibility the energy equation must be solved. For flows with different species, the conservation of mass for each species, or any flow with non-premixed combustion the conservation of the mean mixture fraction equation must be solved. There are many other additional equations which can be solved to model very complicated physical phenomena such as Turbulent equations.

2.1 Mass Conservation Equation

The equation for conservation of mass, or continuity equation, can be written as:

$$\frac{\partial \rho}{\partial t} + \nabla \cdot (\rho v) = S_m \qquad 2.1)$$

Equation 2.1) is the general mass conservation equation and is valid for every flow. The source $S_m$is the mass source that can be taken into account for each volume. This source can represent physics such as phase change.[3]

2.2 Momentum Conservation Equations

Conservation of momentum in an inertial frame is described as:

$$\frac{\partial}{\partial t}(\rho \vec{v}) + \nabla \cdot (\rho \vec{v}\vec{v}) = -\nabla p + \nabla \cdot (\bar{\bar{\tau}}) + \rho \vec{g} + \vec{F} \qquad (2.2)$$

Where:

p : Static pressure

$\rho\vec{g}$ and F are the gravitational and body forces applied to the volume mass. respectively. F can also be considered as any other source term. [3]

$\bar{\bar{\tau}}$: Stress tensor described as:

$$\bar{\bar{\tau}} = \mu[(\nabla\vec{v} + \nabla\vec{v}) - \frac{2}{3}\nabla \cdot \vec{v}I] \tag{2.3}$$

Where:

μ : The molecular viscosity

I : The unit tensor

2.3 Energy Conservation Equation

The general energy conservation equation is:

$$\frac{\partial}{\partial t}(\rho E) + \nabla \cdot \left(\vec{v}(\rho E + p)\right) = \nabla \cdot \left(k_{eff}\nabla T - \sum_j h_j \vec{J_j} + \left(\bar{\bar{\tau}} \cdot \vec{v}\right)\right) + S_h \tag{2.4}$$

k_{eff} : The effective conductivity described as the sum of the thermal conductivity of the material and the turbulent conductivity that is defined according to the turbulent model $(k + k_t)$

$\vec{J_j}$: The diffusion flux of species j.

The terms on the right-hand side of Equation (2.4)(2.3) are representing the energy change due to fluid conductivity, species diffusion, and the dissipation of the viscous forces due to the motion. S_h is the source term which can represent any energy sources in the volume such as heat of the chemical reaction. [3]

In equation (2.4) energy is defined as:

$$E = h - \frac{p}{\rho} + \frac{v^2}{2} \tag{2.5}$$

where enthalpy h is defined for ideal gases as

$$h = \sum_j Y_j \, h_j \tag{2.6}$$

and for incompressible flows as

$$h = \sum_j Y_j h_j + \frac{p}{\rho} \tag{2.7}$$

In Equations (2.6) and(2.7), Y_j is the mass fraction of species j and

$$h_j = \int_{T_{ref}}^{T} c_{p,j} \, dT \tag{2.8}$$

where T_{ref} is considered as 298.15 K in the next calculations. [3]

2.3.1 Energy Equation in Solid Regions

In the solid volumes the energy equation is:

$$\frac{\partial}{\partial t}(\rho h) + \nabla \cdot (\vec{v}\rho h) = \nabla \cdot (k \nabla T) + S_h \tag{2.9}$$

Where:

ρ = Density

h = Sensible enthalpy, $\int_{T_{ref}}^{T} c_p dT$

k = Conductivity

T = Temperature

S_h = Volumetric heat source

The second term on the left-hand side of the Equation (2.9) represents convective energy transfer due to the motion of the solid. This velocity can be transitional or rotational and is computed from the specified motion. [3]

2.4 Turbulence

Turbulent flows have the main characteristic which is their fluctuating velocities. The fluctuations are affecting all the other flow characteristics except mass such as momentum, energy, and species concentration, and cause the transported quantities to fluctuate as well. These fluctuations are very small with a very high frequency which solving them directly (DNS: Direct numerical simulation) requires very small grids that can be computationally so expensive and impossible to perform. Instead, the governing equations can be time-averaged, ensemble-averaged, or otherwise modeled to skip that small scale, resulting in a set of equations that are considering the micro behavior of the flow as a black box with less computational costs. However, the modeled equations contain additional unknown variables, and turbulence models are needed to determine these variables in terms of known quantities. In this thesis work, our focus is on how two-equation models behave, specifically $k - \varepsilon$ model.[3]

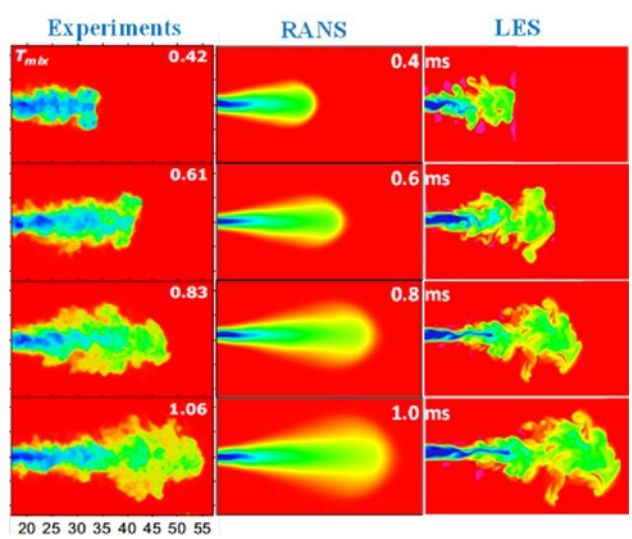

Figure 2.1 Comparison of the temperature contours of RANS and LES models, against the experimental data from Sandia National Laboratory.[4]

2.4.1 Reynolds Averaging

In Reynolds averaging, the terms used in Navier-Stokes are averaged both in time and in space for the fluctuating quantities.

For the velocity components:

$$u_i = \overline{u} + u_i' \tag{2.10}$$

where $\overline{u}$ and u_i' are the time-averaged velocity and the fluctuating velocity($i = 1,2,3$).

Likewise, for pressure, temperature, mixture fraction, and all other quantities:

$$\varphi = \overline{\varphi} + \varphi' \tag{2.11}$$

where φ is the representation of these scalars that are used in the main conservation equations.

After defining the quantities in this was, the Reynolds averaged term can be used to solve the equations. In the case of continuity and momentum:

$$\frac{\partial \rho}{\partial t} + \frac{\partial}{\partial x_i}(\rho u_i) = 0 \tag{2.12}$$

$$\frac{\partial}{\partial t}(\rho u_i) + \frac{\partial}{\partial_{x_j}}(\rho u_i u_j) = -\frac{\partial p}{\partial x_i} + \frac{\partial}{\partial_{X_j}}\left[\mu\left(\frac{\partial u_i}{\partial_{X_j}} + \frac{\partial u_j}{\partial x_i} - \frac{2}{3}\delta_{i_j}\frac{\partial u_l}{\partial x_l}\right)\right] + \frac{\partial}{\partial x_j}(-\rho\overline{u_i' u_j'}) \tag{2.13}$$

These two equations are called Reynolds-averaged Navier-Stokes (RANS) equations.

Generally, these equations are very similar to the Navier-Stokes equation except additional terms now appear that represent the effects of turbulence. In equation (2.13) $-\rho\overline{u_i'u_j'}$ is called Reynolds stresses and must be modeled in such a way to solve the equation.

These equations are mass averaged equations. In the case of variable density, the equations are called Favre-Averaged-Navier-Stokes.[1]

2.4.1.1 Convective Heat and Mass Transfer Modeling

By applying the Reynolds averaging the energy equation changes to:

$$\frac{\partial}{\partial t}(\rho E) + \frac{\partial}{\partial x_i}[u_i(\rho E + p)] = \frac{\partial}{\partial x_j}\left[\left(k + \frac{c_p\mu_t}{Pr_t}\right)\frac{\partial T}{\partial x_j} + u_i(\tau_{ij})_{eff}\right] + S_h \quad (2.14)$$

Where

k : The thermal conductivity

E : The total energy

$(\tau_{ij})_{eff}$ is the deviatoric stress tensor, defined as

$$(\tau_{ij})_{eff} = \mu_{eff}\left(\frac{\partial u_j}{\partial x_i} + \frac{\partial u_i}{\partial x_j}\right) - \frac{2}{3}\mu_{eff}\frac{\partial u_k}{\partial x_k}\delta_{ij} \quad (2.15)$$

2.4.2 $k - \varepsilon$ Model

To model the turbulence in the system with low computation cost, standard, RNG, and realizable $k - \varepsilon$ models are good. All three models have similar forms, with transport equations for k and ε. The main differences between these models are:

- Turbulent viscosity calculation equation.

- The turbulent Prandtl numbers governing the turbulent diffusion of k and ε.
- The ε equation.

Which going to make any of them suitable for different types of flows.

2.4.2.1 Standard $k-\varepsilon$ Model

The standard $k-\varepsilon$ model is based on the general concept of k and ε. The model transport equation for k is derived from the exact equation, while the equation for ε was designed using physical modeling and mathematical reasoning.

The turbulence kinetic energy (TKE), k, and its rate of dissipation, ε, are calculated using:

$$\frac{\partial}{\partial t}(\rho k)+\frac{\partial}{\partial x_i}(\rho k u_i)=\frac{\partial}{\partial_{x_j}}\left[\left(\mu+\frac{\mu_t}{\sigma_k}\right)\frac{\partial k}{\partial_{x_j}}\right]+G_k+G_b-\rho\varepsilon-Y_M+S_k \quad (2.16)$$

And

$$\frac{\partial}{\partial t}(\rho\varepsilon)+\frac{\partial}{\partial x_i}(\rho\varepsilon u_i)=\frac{\partial}{\partial x_j}\left[\left(\mu+\frac{\mu_t}{\sigma_\varepsilon}\right)\frac{\partial k}{\partial_{x_j}}\right]+C_{1\varepsilon}\frac{\varepsilon}{k}(G_k+C_{3\varepsilon}G_b)-C_{2\varepsilon}\rho\frac{\varepsilon^2}{k}+S_\varepsilon \quad (2.17)$$

In these equations:

G_k: TKE generation due to the change in mean velocity $(\overline{u})$:

$$G_k=-\rho\overline{u_i'u_j'}\frac{\partial u_j}{\partial x_i} \quad (2.18)$$

To reduce the cost of calculation and solving the equation (2.13) and, The G_k is calculated in a way to be consistent with the Boussinesq theory:

$$G_k=\mu_t S^2 \quad (2.19)$$

where S is the modulus of the mean rate-of-strain tensor, defined as:

$$S \equiv \sqrt{2S_{\mathrm{ij}}S_{\mathrm{ij}}} \tag{2.20}$$

G_b: The change in TKE due to the buoyancy forces:

$$G_b = \beta g_i \frac{\mu_t}{Pr_t}\frac{\partial T}{\partial x_i} \tag{2.21}$$

Where:

Pr_t: The turbulent Prandtl number for energy.

g_i: The projection of the mass of the components in the ith direction of gravity.

For the standard and realizable $k - \varepsilon$ models, the default value of Pr_t is 0.85.[3]

Y_M : The contribution of compressibility to the total dissipation:

$$Y_M = 2\rho\varepsilon M_t^2 \tag{2.22}$$

$C_{1\varepsilon}$, $C_{2\varepsilon}$, and $C_{3\varepsilon}$ are constants equal to 1.44, 1.92. The $C_{3\varepsilon}$ is affected by the buoyancy and the local constant calculated as:

$$C_{3\varepsilon} = tanh|\frac{v}{u}| \tag{2.23}$$

σ_k and σ_ε are the turbulent Prandtl numbers and are constants equal to 1.0 and 1.3.

S_k and S_ε are any sources to consider.

The turbulent viscosity, μ_t for the standard model is computed as:

$$\mu_t = \rho C_\mu \frac{k^2}{\varepsilon} \tag{2.24}$$

where C_μ is a constant equal to 0.09.

2.4.2.2 RNG $k-\varepsilon$ Model

RNG model is based on the instantaneous Navier-Stokes equation by the "renormalization group" which is a mathematical model. The mathematical model gives the possibility to predict swirling, low-Reynolds number flows, and rapid-strained flows much more robust. The k and ε equations are:

$$2 \tag{2.25}$$

and

$$\frac{\partial}{\partial t}(\rho\varepsilon)+\frac{\partial}{\partial x_i}(\rho\varepsilon u_i) = \frac{\partial}{\partial x_j}(\alpha_\varepsilon \mu_{eff}\frac{\partial \varepsilon}{\partial x_j}) + C_{1\varepsilon}\frac{\varepsilon}{k}(G_k + C_{3\varepsilon}G_b) - C_{2\varepsilon}\rho\frac{\varepsilon^2}{k} - R_\varepsilon + S_\varepsilon \tag{2.26}$$

The difference of this model with the standard one is in modeling the turbulent viscosity. Despite equation (2.24) the process in the RNG model requires solving another differential equation.

$$d\left(\frac{\rho^2 k}{\sqrt{\varepsilon\mu}}\right) = 1.72\frac{\hat{v}}{\sqrt{\hat{v}^3 - 1 + C_v}}d\hat{v} \tag{2.27}$$

$$\hat{v} = \frac{\mu_{eff}}{\mu} \tag{2.28}$$

$$\mu_t = \frac{\rho C_\mu k^2}{\varepsilon} \tag{2.29}$$

These equations are letting the RNG to predict low-Reynolds flow better.

$C_{1\varepsilon} = 1.42$, $C_{2\varepsilon} = 1.68$

2.4.2.3 Realizable $k-\varepsilon$ Model

The realizable $k-\varepsilon$ model has two differences from others. In this model the $C_\mu$is not constant and the dissipation transport equation is modified which is based on exact mean-square velocity fluctuations of the flow.

The transport equation for the k is the same as equation (2.16) and the transport equation for the dissipation energy is:

$$\frac{\partial}{\partial t}(\rho\varepsilon) + \frac{\partial}{\partial x_j}(\rho\varepsilon u_j) = \frac{\partial}{\partial x_j}\left[\left(\mu + \frac{\mu_t}{\sigma_\varepsilon}\right)\frac{\partial\varepsilon}{\partial x_j}\right] + \rho C_1 S\varepsilon - \rho C_2 \frac{\varepsilon^2}{k + \sqrt{v\varepsilon}} + c_{1\varepsilon}\frac{\varepsilon}{k}c_{3\varepsilon}c_b + S_\varepsilon \tag{2.30}$$

To model the C_μ it is required to solve another differential equation to model the Reynolds stress.

$$\overline{u^2} = \frac{2}{3}k - 2v_{\mathrm{t}}\frac{\partial U}{\partial x} \tag{2.31}$$

The C_μ is calculated through:

2.5 Combustion Modeling

To calculate and model the combustion there is a need to solve the transport equations, energy equation as well as additional equations to solve the combustion chemistry. In this thesis work, the main concentration is on the steady diffusion flamelet model and the equilibrium model. In the equilibrium model, it is assumed that the gas is in the chemical equilibrium at all the point of the flame. The advantage of this model is the comprehensive prediction of all the products despite considering the kinetics of the reaction.

These methods are based on solving one or more than one scalar equations (mean mixture fraction, mean mixture variance, …) instead of solving the transport equations for each species. Due to this reduction of the equations, these models are very robust and require less CPU power and time to achieve acceptable results in industrial studies

2.5.1 Chemical Equilibrium

As was explained before the significance of this model is, all the thermodynamic variables are as a function of the mean mixture fraction and the heat loss or gain.

If there is just one mixture fraction, f any value is calculated:

$$\varphi_i = \varphi_i(f, H) \tag{2.32}$$

A great example of the non-adiabatic model is in the case of the radiation or heat exchange in the domain of the reacting flows.

2.5.2 Steady Diffusion Flamelet Model

Similar to the previous model the results are based on equation (2.32) but instead it considers partially equilibrium species in the study using the detailed kinetics of the combustion.

The structure of this method is based on PDF tables. The different species and their mass fraction is computed in this table and later on, it is used by solving the mean mixture fraction.

2.5.3 Mixture Fraction

The fundamental of the non-premixed combustion is on simplification and modeling based on the mean mixture fraction, f. The definition is:

$$f = \frac{Z_i - Z_{i,ox}}{Z_{i,fuel} - Z_{i,ox}} \tag{2.33}$$

In equation (2.33):

Z_i: The mass fraction of element, i.

The values of the oxidizer and the fuel are the other important elements of the calculations that always $Z_{fuel} + Z_{ox} = 1$ in every point of the domain.

2.5.3.1 Mixture Fraction Vs Equivalence Ratio

The mixture fraction can be defined using a very simple equation with F (fuel) next to an oxidizer (o) that ends up to product(s) and air-to-fuel ratio based on the mass of the reactants (r):

$$F + rO \rightarrow (1 + r)P \tag{2.34}$$

By defining the equivalence ratio as φ, defined as:

$$\varphi = \frac{(fuel/air)_{actual}}{(fuel/air)_{stoichiometric}} \tag{2.35}$$

Using the above-mentioned formula the reaction can be considered as:

$$\varphi F + rO \rightarrow (\varphi + r)P \tag{2.36}$$

Looking into the left and right-hand-side of the equation, the mixture fraction can be defined as:

$$f = \frac{\varphi}{\varphi + r} \tag{2.37}$$

This equation allows the computation of the mixture fraction at

a) stoichiometric conditions (φ =1)
b) fuel-rich conditions ($\varphi > 1$)
c) fuel-lean conditions ($\varphi < 1$)

2.5.4 Transport Equations for the Mixture Fraction

Modeling the mean mixture fraction through the transport equation is based on equal diffusivity. The limit of this assumption is in the laminar flows, and the reason for this limitation is that in the Turbulence flows, unlike laminar counterpart the molecular diffusion is negligible compared to the convectional diffusion. The Favre mean (Density-Averaged) mixture fraction equation is:

$$\frac{\partial}{\partial t}(\rho\overline{f}) + \nabla \cdot (\rho\vec{v}\overline{f}) = \nabla \cdot (\frac{\mu_l + \mu_t}{\sigma_t}\nabla\overline{f}) + S \tag{2.38}$$

Where μ_l is the laminar viscosity and μ_t is the turbulent viscosity.

The source term can be considered for any change in the mass such as injection, change the phase (for instance liquid fuel to gas), and ....

Another term which must be taken into consideration is $\overline{f'^2}$ which is solved through:

$$\frac{\partial}{\partial t}\left(\rho\overline{f'^2}\right) + \nabla\cdot\left(\rho\vec{v}\overline{f'^2}\right) = \nabla\cdot\left(\frac{\mu_l+\mu_t}{\sigma_t}\nabla\overline{f'^2}\right) + C_g\mu_t\cdot\left(\nabla\overline{f}\right)^2 - C_{d\rho}\frac{\varepsilon}{k}f'^2 + \mathrm{S} \tag{2.39}$$

where $f' = f - \overline{f}$. The default value for the constants σ_t, C_g, and C_d are 0.85, 2.86, and 2.0.

The mixture fraction variance is represented by the turbulence chemistry.

2.5.5 Flamelet Concept

The flamelet concept models the turbulent flow as thin layers of 1D laminar flamelets. This model uses the linear decrease of the mean mixture fraction and the oxidizer and the strain rate to model the partially equilibrium species.

This reduction of the species equations to two-equation and store them in the look-up table allows us to model the partial-equilibrium species much easier with less complexity. The detailed method to calculate the flamelet is reported in the Bray and Peters work[6]

2.5.6 The Energy Equation for the Non-Premixed Combustion Model

When the non-adiabatic non-premixed combustion model is solving, the total enthalpy form of the energy equation:

$$\frac{\partial}{\partial t}(\rho H) + \nabla\cdot(\rho\vec{v}H) = \nabla\cdot\left(\frac{k_t}{c_p}\nabla H\right) + S_h \tag{1.1}$$

Under the assumption that the Lewis number (Le) = 1, the conduction and species diffusion terms combine to give the first term on the right-hand side of the above

equation while the contribution from viscous dissipation appears in the non-conservative form as the second term.

The total enthalpy H is defined as:

$$H = \sum_j Y_j H_j \tag{2.1}$$

where Y_j is the mass fraction of species j and:

$$H_j = \int^T c_{p,j}\, dT + h_j^0(T_{ref,j}) \tag{3.1}$$

$h_j^0(T_{ref,j})$ is the formation enthalpy of species j at the reference temperature $T_{ref,j} = 298.15\, K$.

2.5.7 Relationship of Mixture Fraction to Species Mass Fraction, Density and Temperature

As it is explained in the flamelet model, temperature and the species mass fraction depend on the mixture fraction, and to model its turbulent interaction with the combustion it is necessary to consider and calculate the variations from the mean values. How is it possible to get the variations using the mean values is using the turbulence chemistry interaction of the combustion. ANSYS Fluent uses the assumed-shape probability density function (PDF) approach as its closure model when the non-premixed model is used using the flamelet which contains the detailed kinetics of the reaction or thermodynamic variable of the species using the chemical equilibrium model. The assumed shape PDF closure model is described in this section.

2.5.8 Description of the Probability Density Function

The Probability Density Function, written as $p(f)$, can be defined as the time-fraction of species next to f. Figure 2.2 plots the time trace of mixture fraction at a point in the flow (right-hand side) and the probability density function of f (left-hand side). The fluctuating random value of f, plotted on the figure is modeled as statistic model, denoted as $\Delta f.p(f)$, plotted on the left side of the figure, has the

value exactly with such area under the curve, Δf, is equal to the fraction of time that f spends in this range. Written mathematically:

$$p(f)\Delta f = \lim_{T\to\infty} \frac{1}{T} \sum_i \tau_i$$

where T is the time scale and τ_i is the amount of time that f spends in the Δf band. The function of $p(f)$ depends on the combustion in f. In practice, $p(f)$ is unknown and is modeled as a mathematical function that approximates the actual PDF shapes that have been observed experimentally.

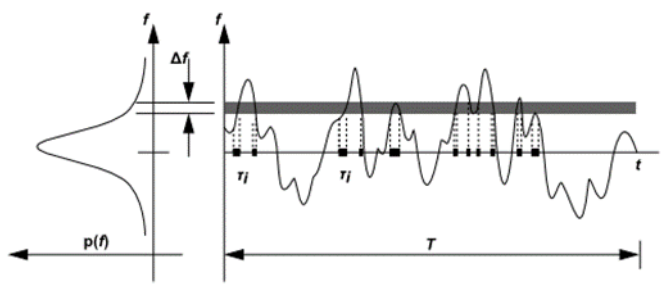

Figure 2.2 Graphical Description of the Probability Density Function

2.5.9 Derivation of Mean Scalar Values from the Instantaneous Mixture Fraction

The probability density function $p(f)$, in the turbulent flow, is used to compute averaged values of variables that depend on f. Density-weighted mean species mass fractions and the temperature is computed using:

$$\overline{\varphi_i} = \int_0^1 (f)\varphi_i(f)df \tag{2.40}$$

2.5.9.1 The Assumed-Shape PDF

The pdf function in the Ansys fluent is calculated using:

a) the double-delta function (two-mixture-fraction cases only)
b) the β-function (single- and two-mixture-fraction cases)

The β-function which is used for this work depends solely on the mean mixture fraction, $\overline{f}$, and its variance, $\overline{f'^2}$. A brief explanation of this method is below.

2.5.9.2 The β-Function PDF

The β-function PDF shape is calculated based on $\overline{f}$ and $\overline{f'^2}$ as:

$$p(f) = \frac{f^{\alpha-1}(1-f)^{\beta-1}}{\int f^{\alpha-1}(1-f)^{\beta-1}df} \tag{2.41}$$

where

$$\alpha = \overline{f}\left[\frac{\overline{f}(1-\overline{f})}{\overline{f'^2}} - 1\right] \tag{2.42}$$

And

$$\beta = (1-\overline{f})\left[\frac{\overline{f}(1-\overline{f})}{\overline{f'^2}} - 1\right] \tag{2.43}$$

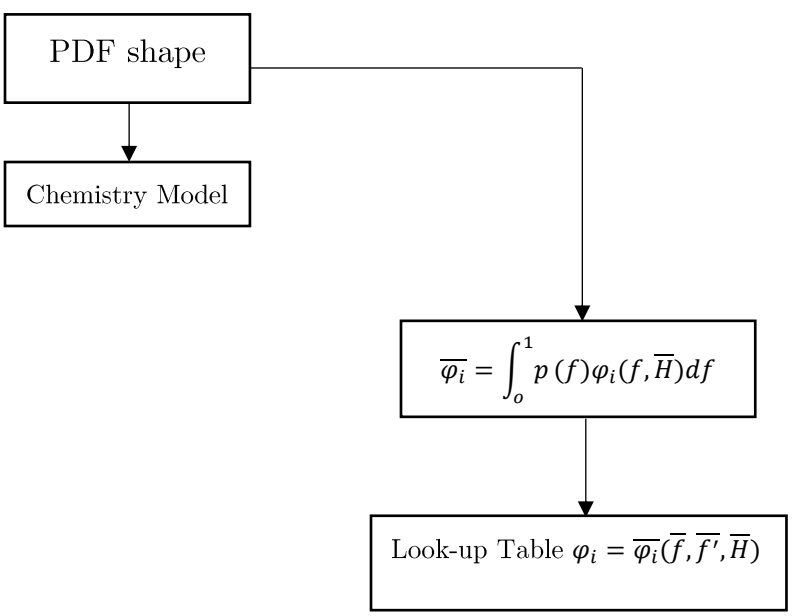

Figure 2.3 Logical Dependence of Averaged Scalars on Mean Mixture Fraction, the Mixture Fraction Variance, and the chemistry Model (Adiabatic, Single-Mixture-Fraction Systems)

2.5.10 Reaction Mechanism

The combustion products contain nitrogen oxides (NOx), carbon monoxides (CO), hydrocarbons (such as BTEX) and particulate matter (PM), etc. All these pollutants are responsible for some serious health issues for humans and nature with a very high effect on global warming. Motor vehicles greatly pollute the environment through emissions such as CO, CO2, NOx, SOx, unburnt or partially burnt HCs and particulates. The main reason for the pollution in urban areas is related to this type of pollutants. Due to their non-equilibrium behavior, it is not possible to understand their formation and estimate it unless detailed kinetics of the reaction is studied.[7]

2.5.11 Chemical Kinetics

From different experimental measurements the rate at which fuel is burnt calculates as:

$$\frac{d[X_F]}{dt} = -k_G(T)[X_F]^n[X_{Ox}]^m \tag{2.44}$$

Where:

$[X_j]$: Denote the molar concentration ($\frac{kmol}{m^3}$) of the ith species in the mixture.

Equation (2.44) states that the rate of dissipation of the fuel is proportional to each of the reactants raised to a certain experimental power. The constant of proportionality, k_G, is called the global rate coefficient, and it depends on the temperature. The minus sign states that the fuel is reducing. This approach can explain the formation of the species as a black-box approach.[2]

In the next two parts the study over the combustion process of

- H_2
- Methane

Is explained.

2.5.11.1 H2 Reaction

Consider the global reaction:[2]

$$2H_2 + O_2 \rightarrow 2H_2O$$

To affect this global conversion of hydrogen and oxygen to water, the following elementary reactions are important:

$$H_2 + O_2 \rightarrow HO_2 + H$$

$$H + O_2 \rightarrow OH + O$$

$$OH + H_2 \rightarrow H_2O + H$$

$$H + O_2 + M \rightarrow HO_2 + M$$

among others.

When oxygen and hydrogen molecules collide and react, they do not yield water, but, instead, form the intermediate species HO_2, the hydroperoxy radical and a hydrogen atom, H, another radical. These radicals are very reactive. To form HO_2 from H_2 and O_2, only one bond is broken, and one bond is formed. Alternatively, one might consider that H_2 and O_2 would react to form two hydroxyl radicals (OH). [2]

Understanding the reason behind the formation of OH is useful in modeling and comparing the results in the next chapters. For further explanation, Saxena's work is suggested[8]

2.6 Methane Combustion

Due to tetrahedral and strong C-H energy bonds, methane has a unique and complicated combustion behavior. For example, it has a high temperature and low flame speed compared to other hydrocarbon fuels.

There have been lots of researches on methane combustion to understand the detailed behavior of it. Kaufman, in a review of combustion kinetics, indicated that the methane combustion mechanism evolved in the period 1970-1982 from less than

15 elementary steps with 12 species to 75 elementary steps, plus the 75 reverse reactions, with 25 species[2].

The results of the researches done together has led into creation of a kinetic library. The mechanism GRI Mech, is based on the optimization techniques of Frenklach *et al.* GRI Mech is available for free over the internet and is updating and improving based on the researches that are going on. Version 3.0 takes into account 325 elementary reactions involving 53 species. Many of these reactions contribute to H, and CO oxidation mechanisms.[9]

2.7 NOx Model

The emission of the NO in the flames are controlled by three main pathways:

Prompt NO, Thermal NO, the N_2O intermediate mechanism. The thermal NO is calculated using the Zeldovich mechanism as it is presented in the Table 2-1.

Reaction	B_β	α_β	E_β
$N_2 + O = NO + N$	1.9E+14	0	318.7
$O + NO = N + O_2$	2.4E+09	1	161.6
$NO + H = N + OH$	1.3E+14	0	205.7

Table 2-1 Zeldovich mechanism in units of mol, cm, s, kJ and K.

As it is illustrated above the path is highly effected by the presence of the O and the OH and it is highly sensitive to the temperature field which makes it very important to couple it with good predicton of the temperature.

The N_2O pathway is an alternative to the thermal NO, according to the study by Bonturi [10] the intermediate pathway is not important in the low pressure combustion and in case of high pressure combustions it does not have more than 11% in contribution.

Due to slow formation of the NO it is not possible to calculate it using the flamelet library presented for methane and hydrogen, so there is a need to solve an extra transport equation for the NO modeling.

$$\frac{\partial}{\partial_{X_j}}\left(\overline{\rho}u_j\overline{Y_{NO}}\right) = \frac{\partial}{\partial x_j}\left(\frac{\mu_{eff}}{\sigma_{NO}}\frac{\partial\overline{Y_{NO}}}{\partial x_j}\right) + \overline{\dot{\omega}_{NO}} \tag{2.45}$$

Where σ_{NO} is the schmit number and the $\overline{\dot{\omega}_{NO}}$ is the source term which calculated based on the scalar dissipation and the pdf model.

2.8 Boundary Conditions

I. Inlet

This problem has two different inlets:

- Fuel
- Oxidizer

The fuel velocity is modeled as it is explained in section (4.3) with the ambient temperature and the mean mixture fraction of one.

For the oxidizer, the value of the mean mixture fraction is equal to zero.

II. Outlet

The outlet is a pressure outlet which means the products are entering the atmospheric pressure and it is modeled as:

$$P_{outlet} = 0$$

III. Symmetry

The meaning of the symmetry is that the gradients normal to the boundary are zero so both sides of the boundary have identical values.

IV. Walls

In the case of the walls there is 2 consideration:

- Thermal condition: Constant temperature or constant flux.
- Momentum conditions: slip or no-slip condition.

2.9 Solver

Choosing the proper solver and solution method is very important in the accuracy and convergence of the solutions. A brief type of each solver is reported in this section.

Pressure-velocity coupling	**Coupled**
Gradient	Least square cell-based
Pressure	PRESTO!
Momentum	Second-order upwind
Turbulent kinetic energy	Second-order upwind
Turbulent dissipation energy	Second-order upwind
NOx modeling	Second-order upwind
Energy	Second-order upwind
Mean/Variance mixture fraction	Second-order upwind

Table 2-2 Solution methods.

2.9.1 Coupled Pressure-Velocity

As a brief view of the solving methods, there are two options to implement:

- Segregated
- Coupled

In segregated solvers, the momentum equation is solved and the pressure value is derived from the correction factors.

As it is illustrated in Figure 2.4 Coupled based algorithm. solves the momentum and continuity equation simultaneously.

Generally segregated solvers provide faster iteration times and slower convergence (based on the number of iteration) while the coupled solver is slow. Getting advantage of the solving method illustrated in 2.10 makes coupled algorithm very feasible.

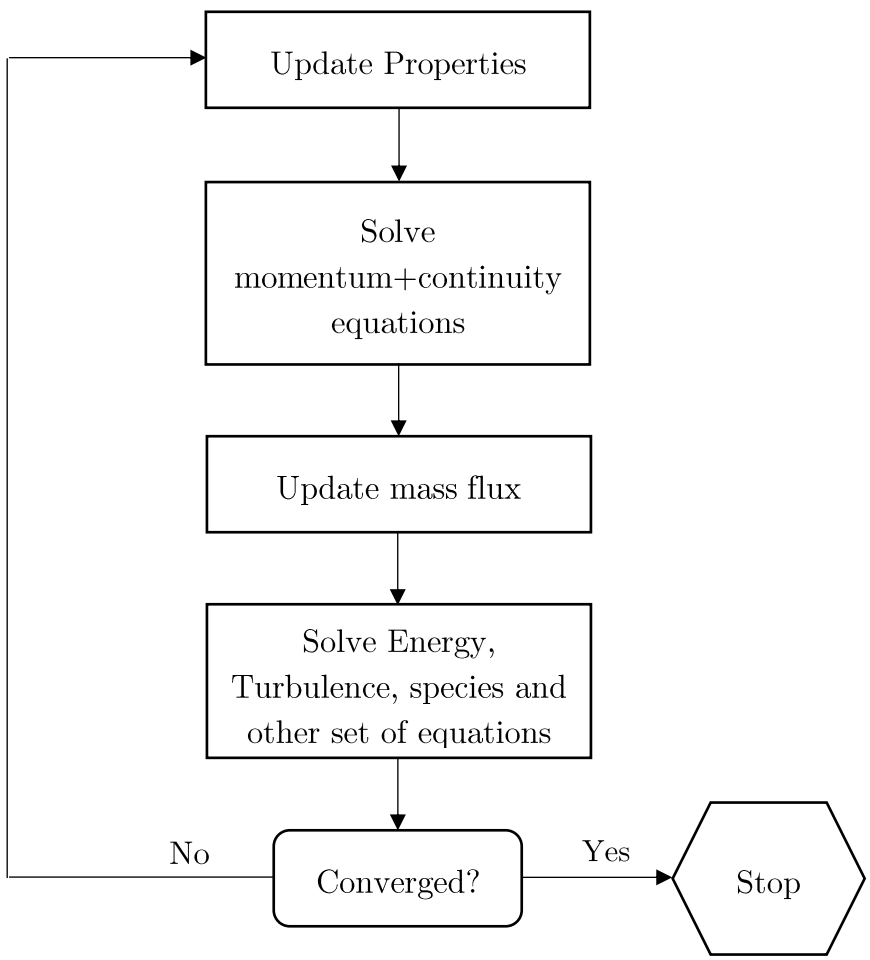

Figure 2.4 Coupled based algorithm.

2.9.2 Least Square Cell-Based

In this method the change in cell values between E_i and E_{i+1} is computed as:

$$(\nabla\varphi)_{E_i} \cdot \Delta r_{i,i+1} = (\varphi_{i+1} - \varphi_i) \tag{2.46}$$

By calculating the abovementioned equation for all the cells a general system of equations will be calculated for each cell, which the stiffness matrix depends on the geometry.

$$[J](\nabla\varphi)_i = \Delta\varphi \tag{2.47}$$

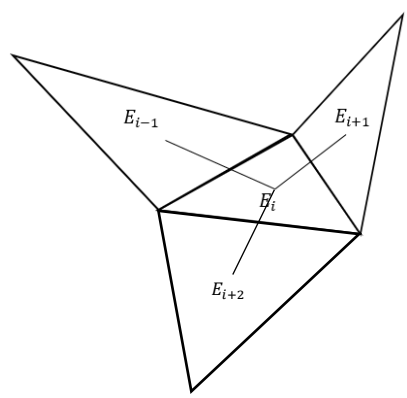

Figure 2.5 Cell centroid evaluation.

2.9.3 Second-Order Upwind

To use the second order model for the aacuracy of the solved values, a multi dimensional linearization method is used. According to this method a high accuracy is achieved by creating a taylor expansion on the cell face about the cell centroid. In this model the face value is calculated using the:

$$\phi_{face} = \phi + \nabla\phi.\vec{r} \tag{2.48}$$

Where the values are calculated using 2.9.2.

2.10 Temporal Solution

The coupled set of equations are solved until the steady flow state. The temporal state of the equations is calculated by an implicit or an explicit algorithm. The two methods are explained in the next sessions. As a brief explanation, in the explicit method, the time step is determined by the CFL condition. To have an accurate time stepping in the calculations, explicit model uses the same time step in all the cells of the computational grid (it is called global time step), The method which is used in this thesis work is implicit time-stepping which is explained in detail.

2.10.1 Implicit Time Stepping (Pseudo Transient)

In general (unsteady flow) to solve any equation there is a need to do discretization both in space and time. In an equation such as:

$$\frac{\partial}{\partial t}\int_V W\,dV + \Gamma\frac{\partial}{\partial \tau}\int_V QdV + \oint [F - G]\cdot dA = \int_V HdV \tag{2.49}$$

The t denotes physical-time (which is used for unsteady flow) and τ is a pseudo-time used in the time-marching procedure (for steady-state or unsteady flow).

2.10.1.1 Pseudo Time Step Calculation

The automatic fluid time scale for fluid zones is calculated using the minimum of the different time-scales:

$$\Delta T_{fluid} = \text{Min}\,(\Delta T_U, \Delta T_p\ \ , \Delta T_g, \Delta T_{rot}, \Delta T_{compress}) \tag{2.50}$$

Each of these time scales is calculated using the length scale and fluid velocity. It is tried to demonstrate how is it calculated by giving an example using the ΔT_U. A detailed explanation is present in the ANSYS Fluent theory guide[3].

$$\Delta T_U = \frac{0.3L_{scole}}{Max(U_{bc}, U_{domain})} \tag{2.51}$$

$$L_{scale} = MAX(L_{vol}, L_{ext}) \tag{2.52}$$

And the definition of each length scale is defined as:

$$L_{vo1} = \sqrt[3]{V} \tag{2.53}$$

$$L_{ext} = MAX(L_X, L_y, L_Z) \tag{2.54}$$

L_X, L_y, L_Z are respectively the maximum length of the elements.

The advantage of using this method is it helps to converge very much.

2.11 Meshing

Discretization in space is a very important step in numerical modeling. The combination of the elements in the space is the representation of the problem.

Having a mesh with high quality and low skewness will lead to better convergence and faster solution results. According to the Fluent theory guide range of skewness, less than 90 is acceptable.

$$Skewness = \frac{Optimal\ Cell\ Size - Cell\ Size}{Optimal\ Cell\ Size} \tag{2.55}$$

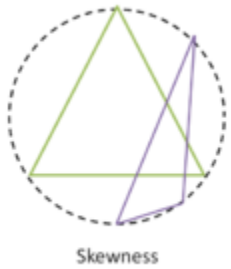

Figure 2.6 Graphical representation of an optimal cell (in green).

3. Bluff-Body Burner

To be able to develop and optimize models to study any combustion, there is a need to understand and verify the numerical turbulence models, combustion models, and NOx models with an experimental case. The best study and research which has initiated in the late 90s at the University of Sidney on different fuels and different bluff-body burners is a good candidate.[11]

The burner which is a ceramic body is placed in the middle of a wind tunnel to feed it with constant air (Oxidizer) and fuel. The presence of this burner (bluff-body burner) next to the co-flow creates a recirculation zone that helps to stabilize the flame and makes it easy to measure and examine it. At high velocities of the fuel, the flame can penetrate and pass through the recirculation zone, unlike any other pilot flames. The flame can continue and extinguish at a far distance from the fuel jet. This extinction of the flame highly depends on the turbulence interaction and chemistry modeling of the combustion. The flame may reignite again in further distance due to turbulence interaction. Generally, there are three main zones which are: stabilization, extinction, and re-ignition zones.[12]

Figure 3.1 Schematic drawing of a bluff-body combustor and measuring locations. represents the schematic drawing of the bluff-body and the measurement planes.

In this chapter, a brief explanation about the bluff-body burner, geometry, boundary conditions, and experimental database is provided.

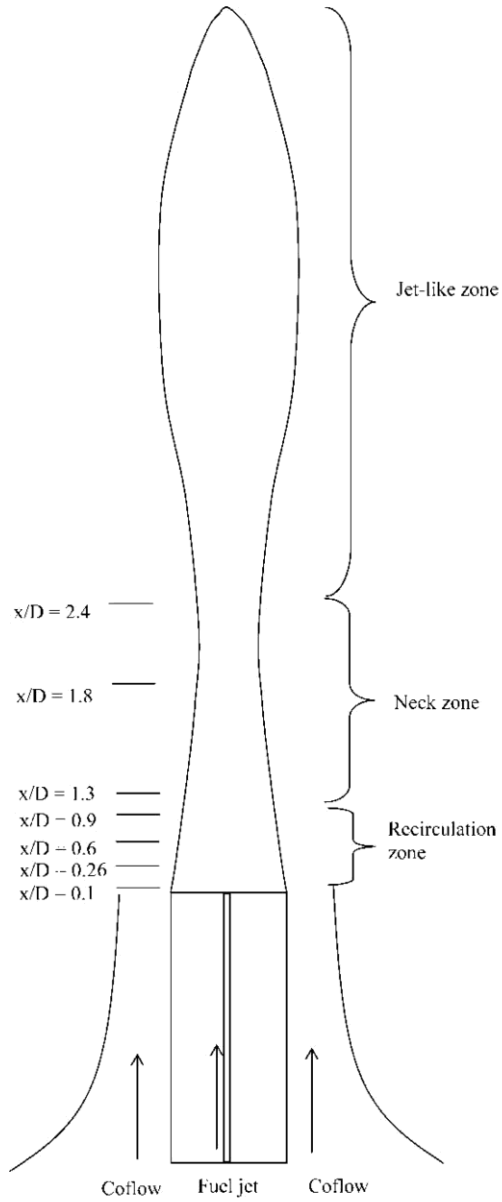

Figure 3.1 Schematic drawing of a bluff-body combustor and measuring locations.

3.1 Geometry and Boundary Conditions

Bluff-body burners produced and tested with different diameter sizes of D_b, and fuel jet diameters, D_j. The stability factor of these burners are provided using an indicator based on the ratio of the fuelt jet and cow-flow velocity. The length of the recirculation zone is about one bluff body diameter (around 1.2 times). It is

stated that the addition of H_2 to the CH_4 fuel is intended to create a recirculation zone that is clean from soot. It is observed in the case of using pure CH_4 the soot formed in the recirculation zone travels to the upper levels and interferes with the Raman signals.[12]

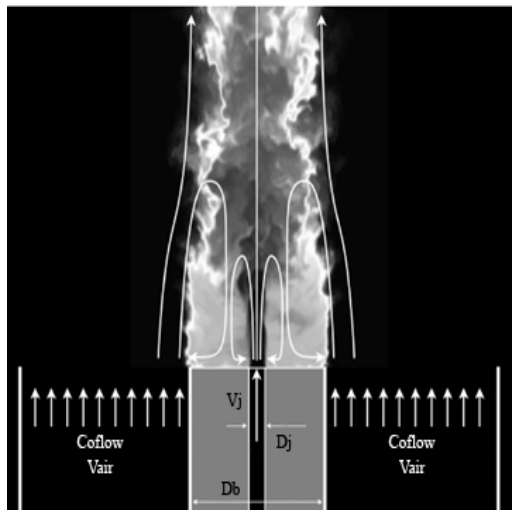

Figure 3.2 View of the HM bluff-body burner.

U_e (External ambient co-flow velocity), is very significant in the mixing. Higher velocities lead to higher gas momentum around the burner and bluff-body, leading to a significant amount of pinching in the necking zone. The free stream of the cowflow has turbulence equal to 2% and velocity is 40 $\frac{m}{s}$.

U_j: Fuel jet velocity. This velocity is present in two different experimental tests, for HM1 flame 118 $\frac{m}{s}$ of bulk velocity (not developed flow) and for the HM2 flow this velocity is 176$\frac{m}{s}$. The exact calculation of these velocities is reported in section (4.3)

Flame	Fuel	U_j/U_e	Z_{st}
HM1	CH4/H2	118/40	0.05
HM2	CH4/H2	178/40	0.05

Figure 3.3 Flame characteristics.

D_j: Fuel jet diameter. Simply the inner diameter of the central fuel jet, ($D_j = 3.6$ mm).

D_b - Bluff-body diameter. The diameter of the ceramic face ($D_b = 50$mm).

The mixture is CH4/H2 (50/50 % by vol.). As it is stated the methane which is used here is CNG and it contains 10% of different hydrocarbons, but all the data is calculated based on the pure CNG.

Using the formula:

$$Y_{CH_4} = \frac{\rho_{CH_4}}{\rho_{CH_4} + \rho_{H_2}} \tag{3.1}$$

$$Y_{H_2} = \frac{\rho_{H_2}}{\rho_{CH_4} + \rho_{H_2}} \tag{3.2}$$

The mass fractions are calculated at the 300K, and 1atm condition.

3.2 Flame Characteristic

The visual appearance of the flame was observed over a wide range of values of mean external air velocity, $\overline{u}$ and mean jet velocity, $\overline{u}$. It was found that three basic flame shapes, depending mainly on the ratio $\overline{u}/\overline{u}$, could be observed[11]:

I. Flame A (Figure 3.4) is a short flame that is controlled by the recirculation induced by the oxidizer. Oxidizer creates a strong recirculation zone which dissipated all the fuel very fast (Why it is very short).
II. Flame B is a middle-state flame, which has the same velocity as the oxidizer and the fuel. This equality makes it not to extend (still fast dissipation).
III. Flame C is dominated by the central fuel jet. The fuel velocity is high enough (relative to the oxidizer) that it can penetrate and extends the flame.

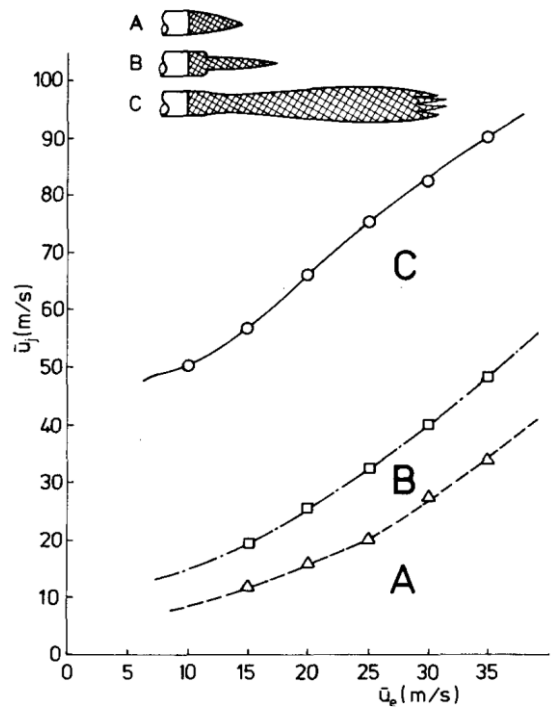

Figure 3.4 Flow characteristics of the natural gas diffusion flame stabilized by a bluff-body

Between the above-mentioned cases, flow type C has a large significance to study. The reason is the penetration of the jet flow is very important due to turbulence interaction with the combustion. To understand it, there is a need to look back to the different methods which were explained before to model the combustion. This extends of the flame can cause some partially-equilibrium and non-equilibrium species start to form

At low jet velocities flame, C is an all-yellow quasi-cylindrical flame. As the fuel velocity is increased by keeping the co-flow constant the flame starts to extend, and then to blow off in the blue neck region while the yellow recirculating flame is still stabilized on the nozzle.

The start of puffing is taken as the blow-off limit of the flame. Figure 3.5 shows the blow-off limits of the natural gas flames respectively and illustrate the visual appearance of the flames at conditions dose to these limits. The. A clean blow-off limit is obtained when the face of the bluff body is free from soot. In region I, at low values of U_e, only hot gas exists in the recirculation zone and the flame is conical in shape and shows little luminosity due to soot. In region II, the

recirculating vortex entrains fuel to form a yellow flame lifted off from the face of the bluff body, and in region III, at high enough U_e, a yellow recirculating flame is stabilized on the bluff body. The "sooty blow-off limit" obtained when the face of the bluff body is covered with soot.[11]

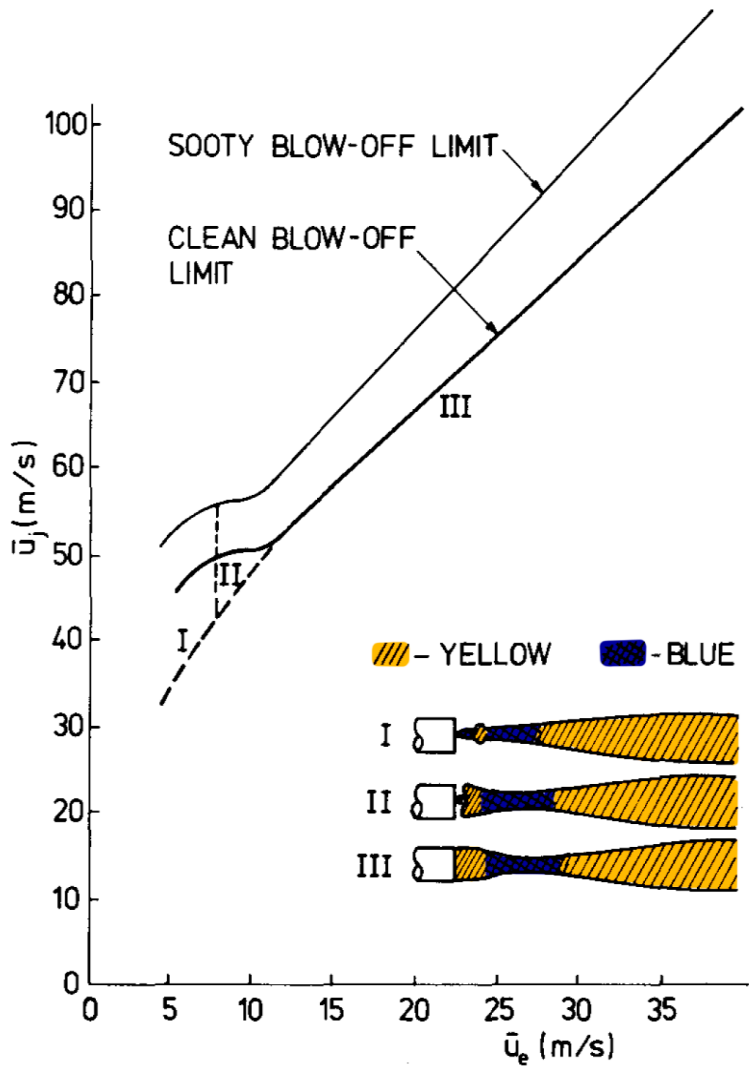

Figure 3.5 Blow-off limits for the natural gas turbulent diffusion flame stabilized by a bluff body.

3.3 Measurements

The study of gaseous combustion requires space and time-resolved measurements of temperature and species concentrations. Intrusive probe measurements of time-averaged temperature and major species concentrations have been made in sooting and non-sooting flames by many researchers. Such techniques can perturb the flow and are subject to potential errors due to, for example, catalytic effects on thermocouples and inadequate quenching in the sampling probe. More important, in turbulent flames, time-averaged measurements are obtained, and these give little insight into the actual combustion process.

A piloted burner developed at the University of Sydney has been installed in the Sandia Turbulent Diffusion Flame Facility, where all the measurements were performed. A schematic of the test section is shown in Figure 3.6.[13]

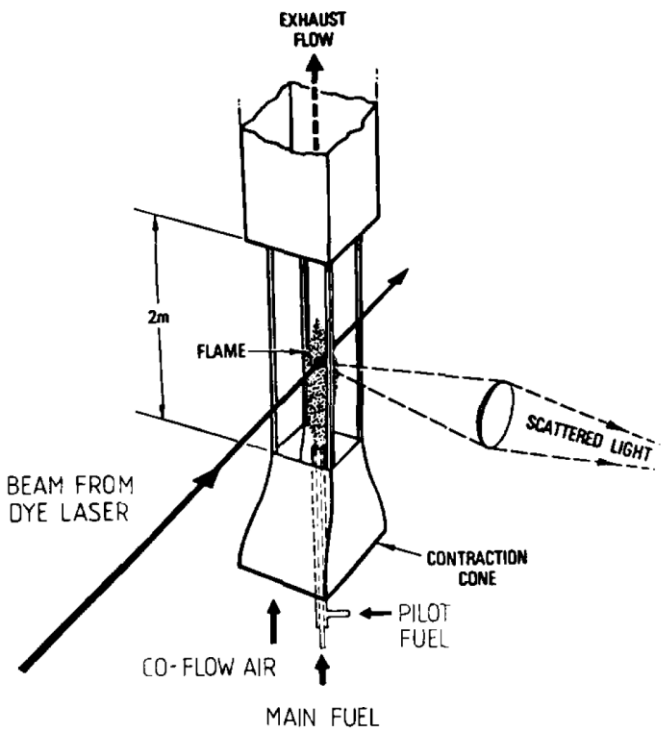

Figure 3.6 Schematic of the experimental test setup for the piloted flame burner at the Sandia Combustion Research Facility.

The method to measure the temperature and species concentrations is the scattered Raman method, a detailed theoretical treatment of Raman scattering can be found in Ref. [14].

3.4 Measurements Uncertainty

To be able to develop any numerical model and compare the results with the experimental data, it is necessary to consider and understand the errors and uncertainties in experiments.

As reported by Dally et al.[15] the measurement errors associated with bluff-body burners are due to many different issues such as shot noise, electronic noise, set-up of the optical instruments, resolution errors, interference between Raman signals, the fluorescence errors from soot production, and some other calibration issues.

The available reports for the measurements of CH_4/H_2 flames are provided in the table. The errors due to signal interference and the resolution errors are not considered in the evaluations. As it is explained before the excess of the H_2 to the methane helps to reduce soot, so the issues with florescent interference are almost negligible. Most interference errors are associated with CO measurements which are around 10%.

Species	%Mass fraction	%Error
O_2	4.0	10.0
N_2	75.0	0.8
CO_2	8.0	4.5
CO	2.0	9.0
H_2	0.5	12.5
H_2O	11.0	5.0

Figure 3.7 Errors associated to different species.

In the next chapter, the CFD modeling and the results are compared with this experimental set and results to examine the Turbulence interaction of the non-premixed combustion.

4. CFD Model and Results

The objective of this chapter is to model the buff-body which is tested experimentally at the University of Sidney using two turbulence models: Realizable and Standard K-epsilon models. According to the previous studies over the bluff-body burners, there are some suggestions for the standard k-epsilon.[16]

After performing a grid size study over the HM1 flame, the effect of the different turbulence models, combustion models are compared with experimental results of the species mass fraction, mean mixture fraction, and temperature.

Later on, the same model is applied for HM2 flame with a different characteristic to examine the existing model.

4.1 Geometry and Mesh

The geometry is designed using the CAD software to represent the real physical test. As it is already explained in the Bluff-Body Burner section the physical set is composed of two main part:

- Ceramic bluff-body with central fuel injection jet.
- Air blow off.

The designed geometry is presented in

To reduce the computational time, the geometry is divided into 4 using the 2 symmetry planes.

After defining the governing equations and the 3D geometry, the next task is to convert the algebraic domain to a computer solvable domain using volume discretization. The method for this study is using the hybrid mesh.

A Hybrid mesh is a type of mesh that contains some structured and unstructured grids to be to represent the curves and details in a very efficient manner.

The reasons why this method is adopted are:

- This type of mesh has very efficient computational performance due to others.
- Due to its unstructured characteristic, it is possible to choose different grid sizes for the computational domain. in this study, the zone which is called the recirculation zone requires very dense mesh.
- Compare to some other methods this type of mesh provides the convergency in solution.

4.2 Mesh optimization

To define the mesh for computations it is required to check and evaluate the mesh quality. The quality of the mesh which is indicated by mesh skewness, mesh quality, and mesh size (density) affects the solution precision and rate of convergence.

Choosing a very coarse mesh can lead to a very poor prediction while a very dense mesh can end to convergence issues and very high computational time.

To optimize the mesh, a grid dependence study is done. To do this study the combustion model with the standard k-epsilon suggested by Hossain [16] is applied to the geometry with different grid sizes and quality to find the optimum mesh for further studies.

As it is reported in Table 4-1, the study is done over 6 different mesh cases. The first mesh has the lowest density while the last one represents the highest. It is worth mentioning that case number 5 has very dense mesh in the recirculation zone to study the effect of mesh size in different zones.

Mesh Case	Minimum Size	Skewness	#Elements	#Nodes
1	5mm	0.2493	383870	83514
2	3mm	0.2469	60400	13003
3	2mm	0.2430	87580	18289
4	1mm	0.2287	317587	60584
5	0.5-1 mm*	0.2203	1163903	209405
6	0.5mm	0.2200	2224463	407489

Table 4-1 Different mesh profiles.

As it is represented in Figure 4.1, the mesh size is visualized for all the cases. Creating different zones helps significantly with faster solutions.

As it is represented in Figure 4.2 the results of each mesh case for maximum mixture fraction at 120mm, the temperature at 45mm, and velocities at 5mm and 13mm display how higher mesh profile number 6 has a good resolution.

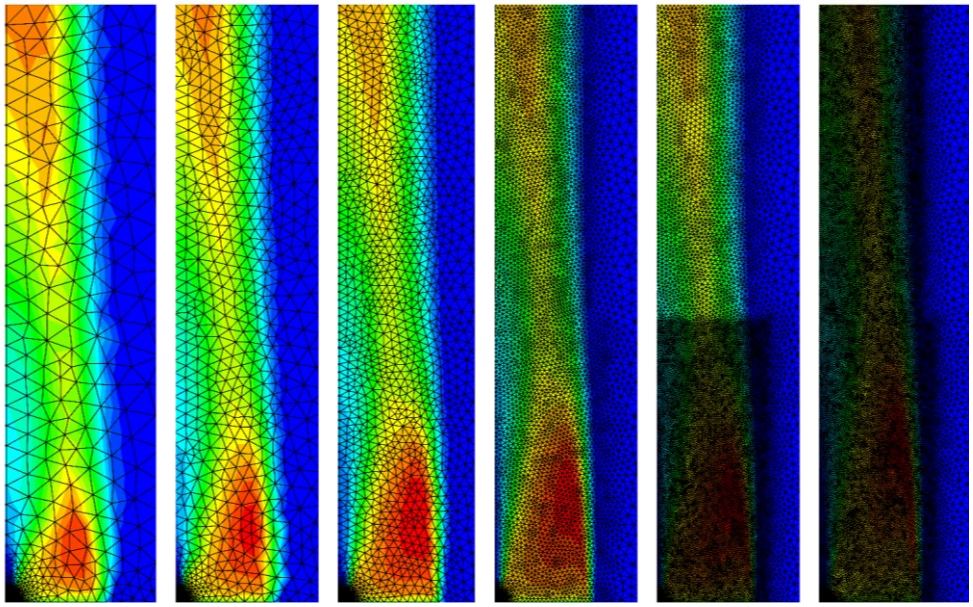

Figure 4.1 Contours of the mesh size.

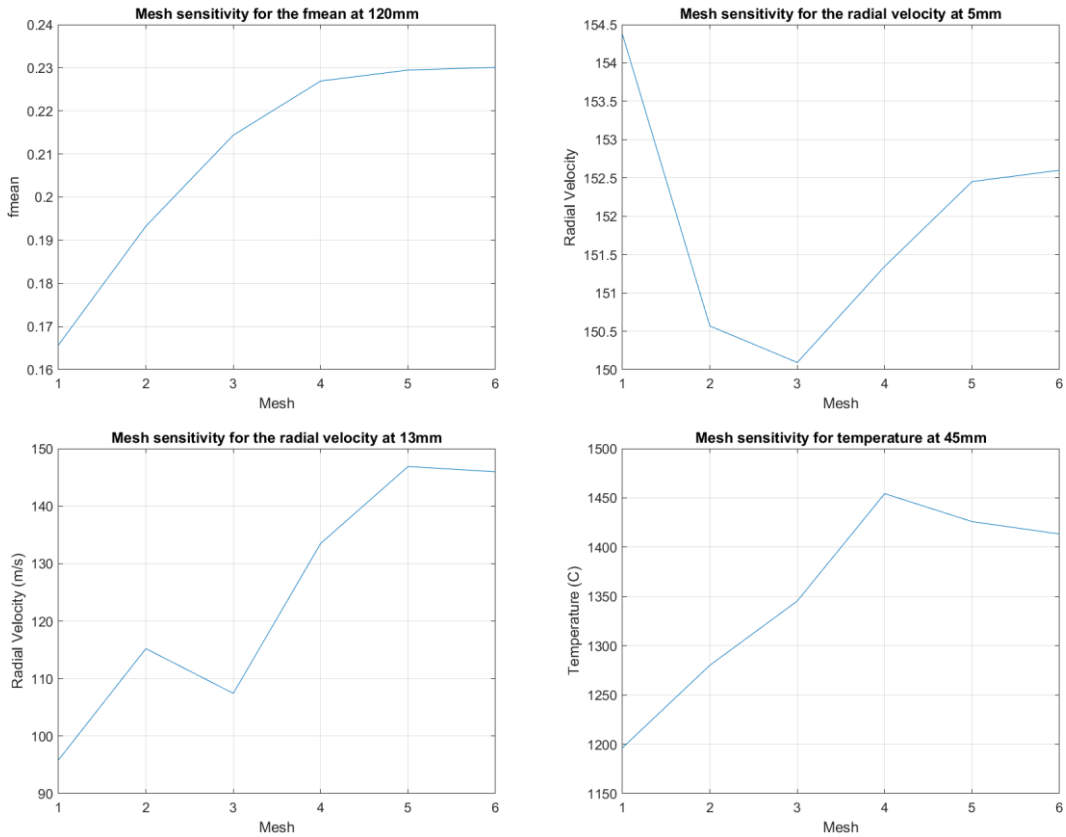

Figure 4.2 Convergence plots for the mesh optimization studies.

Figure 4.3 illustrates how grid size and mesh density increases the computation time.

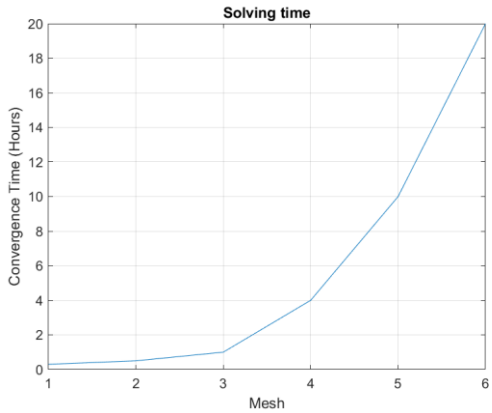

Figure 4.3 Mesh size and the solving time.

Figure 4.4, Figure 4.5, and Figure 4.6 is a graphical representation of the mean mixture fraction, temperature, and turbulent kinetic energy for mesh cases 1, 2, 3, 4, and 6.

It is obvious that having big elements in the recirculation zone and especially jet flow forces the model to have a flat-like prediction for the mean mixture fraction. Due to this error, the combustion process is much faster and causes very poor predictions.

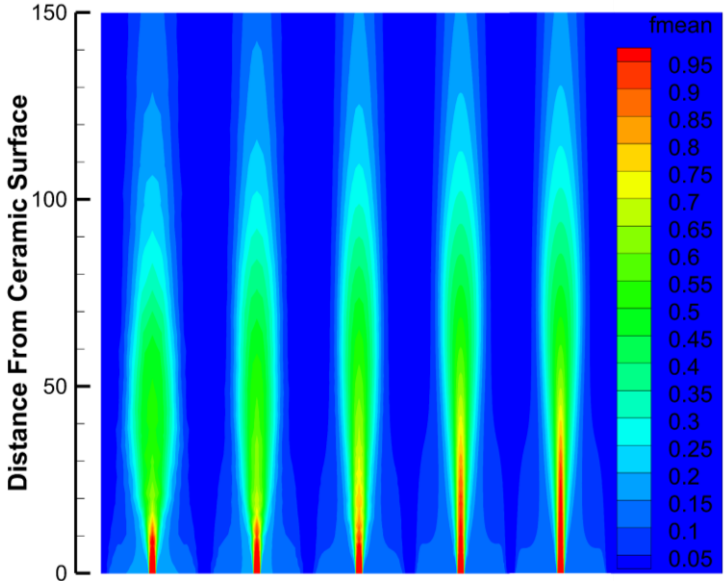

Figure 4.4 Contours of mean mixture fraction for different mesh densities (coarse mesh left).

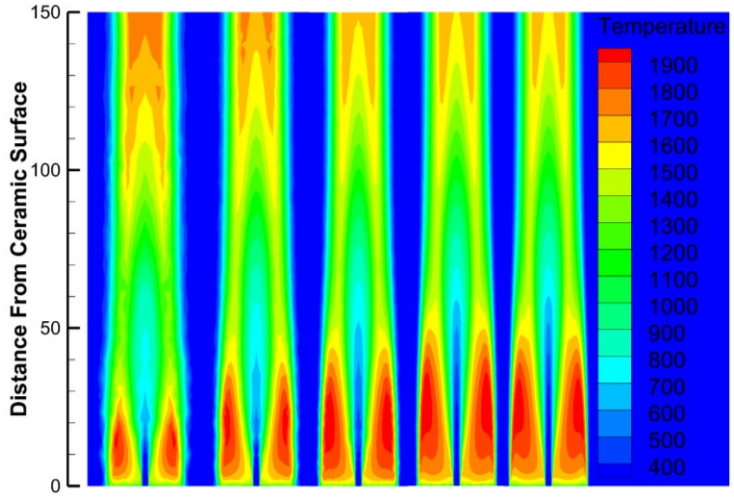

Figure 4.5 Contours of temperature for different mesh densities (coarse mesh left).

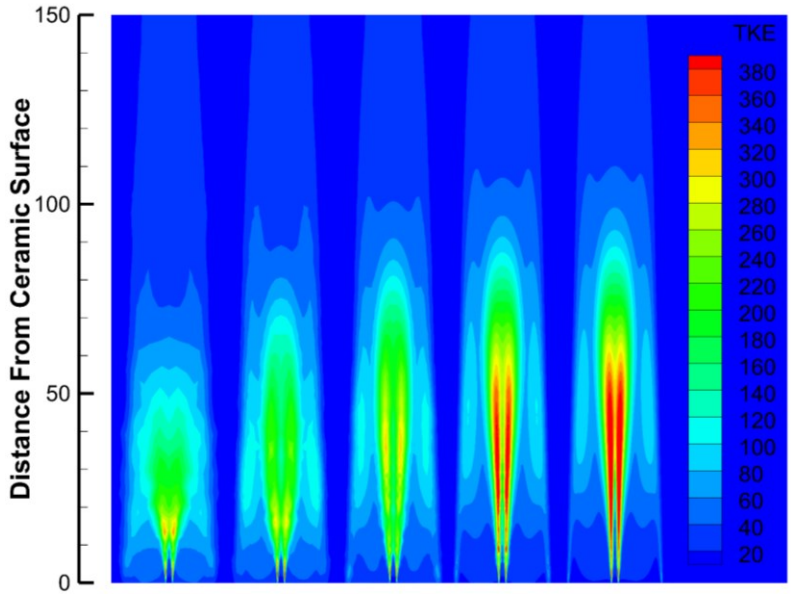

Figure 4.6 Contours of TKE for different mesh densities (coarse mesh left).

Even though mesh profile #4 has an adequate prediction, all the studies are done using mesh profile #6.

4.3 The velocity profile in the jet outlet

One of the main challenges for this study is to model the velocity fields with high accuracy. The importance of the accuracy in the velocity field is that a very slight change in the momentum equation can have a huge impact on turbulent interaction and the combustion process.

To full fill this issue there are two solutions:

- Considering the fuel pipe geometry and solving the equations (no data about the size of the pipe is available).
- Defining the velocity profile of the jet outlet.

The implemented method for this study is the second solution considering fully developed flow in a pipe with a diameter equal to 3.6 mm due to a decrease in the number of elements and CPU hours.

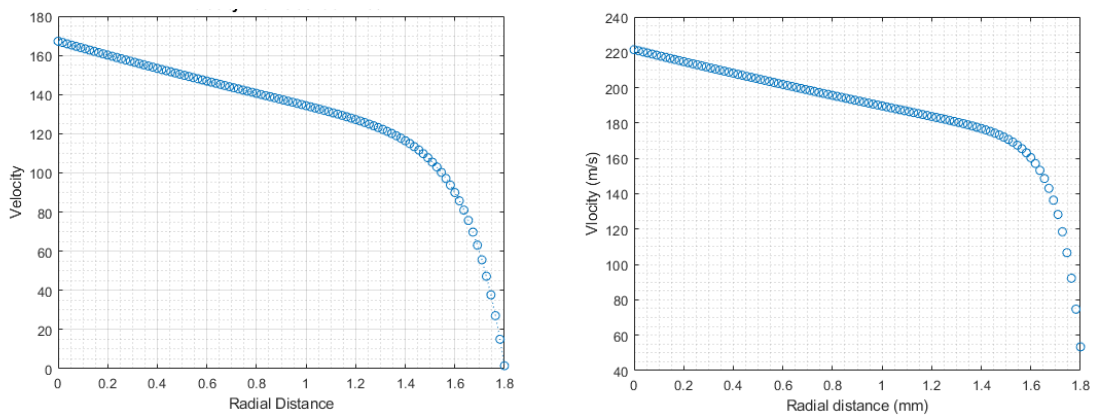

Figure 4.7 Velocity profile of the fuel jet for the HM1-HM2 flame.

By performing a CFD study in the pipe the velocity profile of the jet is solved according to Figure 4.7. As is evident in the figure, the velocity of the jet increases to 168 $\frac{m}{s}$ in the jet center.

The same study and method are used for the HM2 flame. As presented above the maximum value of the velocity in the jet increases up to 221 $\frac{m}{s}$.

4.4 Study using the default realizable k-e model

Due to the characteristic of the non-premixed combustion, having a proper turbulence model has a significant impact on the prediction of the thermal field and the species. As it is explained in 2.4 Realizable k-epsilon model provides a very realistic model.

By computing the previously mentioned case using this model the results did not make sense. Considering the Hossain works [16] it is required to find a proper turbulence coefficient to predict the decay rate of the fuel properly.

The default model provides a very fast decay rate for the fuel, which causes to have faster combustion. In the next section, the method of optimization and the results of optimization is reported in detail.

4.5 Optimization of the realizable k-e model

To find the proper coefficient for the turbulence model it is required to run the model with different values of $C_{2\epsilon}$ and monitor the mean mixture fraction at 120mm. By comparing different results, 1.75 gives the best estimation for the decay rate of the fuel jet. As it is observed before (even if it was not the aim of the study) poor prediction in the flow field causes errors in the mean mixture fraction value.

Looking into Figure 4.9 underprediction of the mean mixture fraction means the fuel is consumed by the combustion process. The reason behind this issue is solved by the modification.

Figure 4.12 and Figure 4.13 which are the represents of the flow field demonstrate how this modification leads to an adequate prediction.

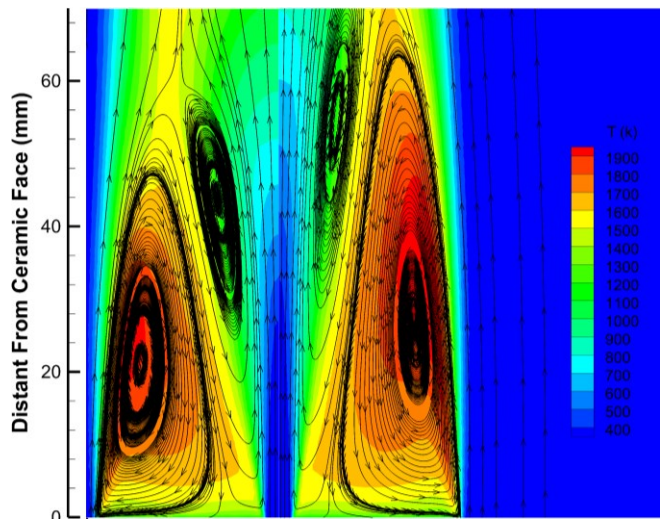

Figure 4.8 Temperature contour of the default(left) and modified K-epsilon model.

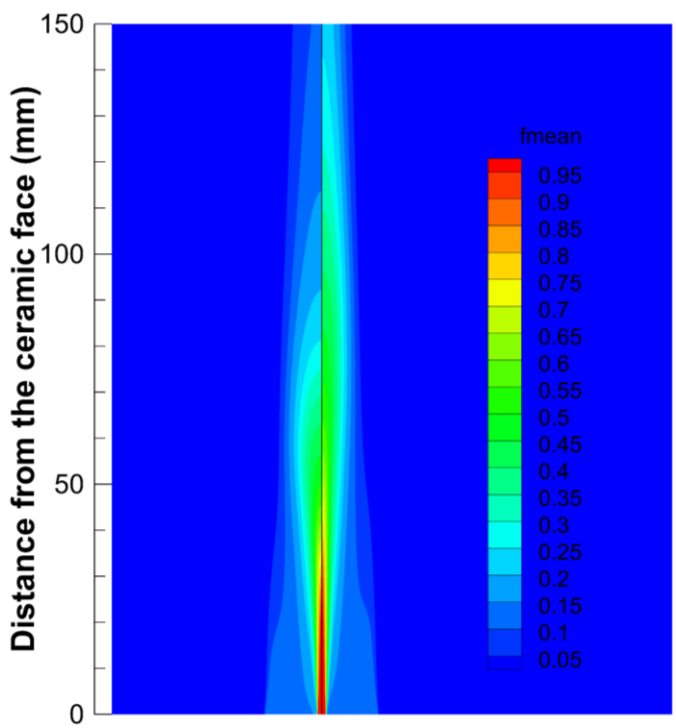

Figure 4.9 Mean mixture fraction contour of the default(left) and modified K-epsilon model.

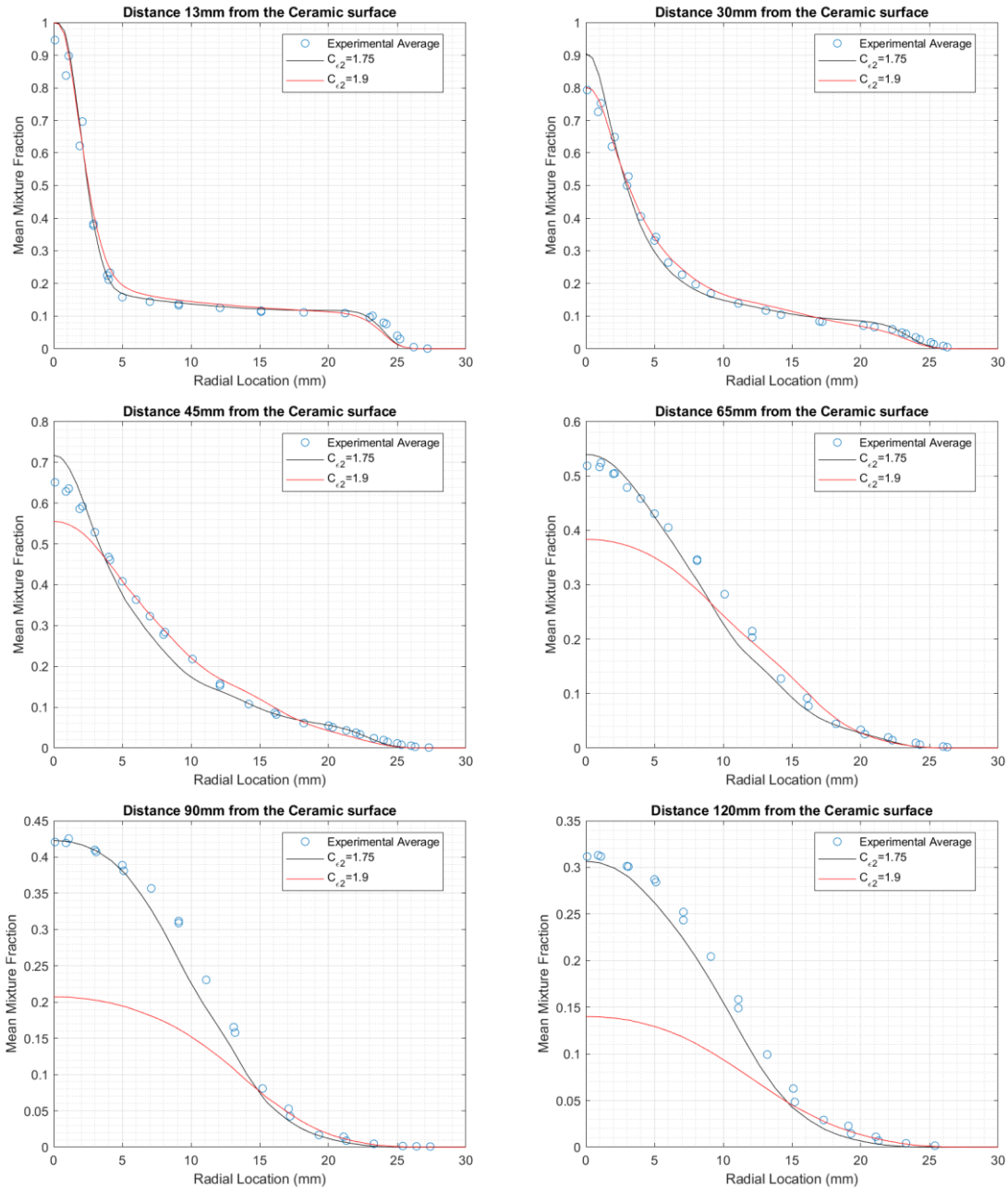

Figure 4.10 Radial profile of the mean mixture fraction.(modified and default turbulence model).

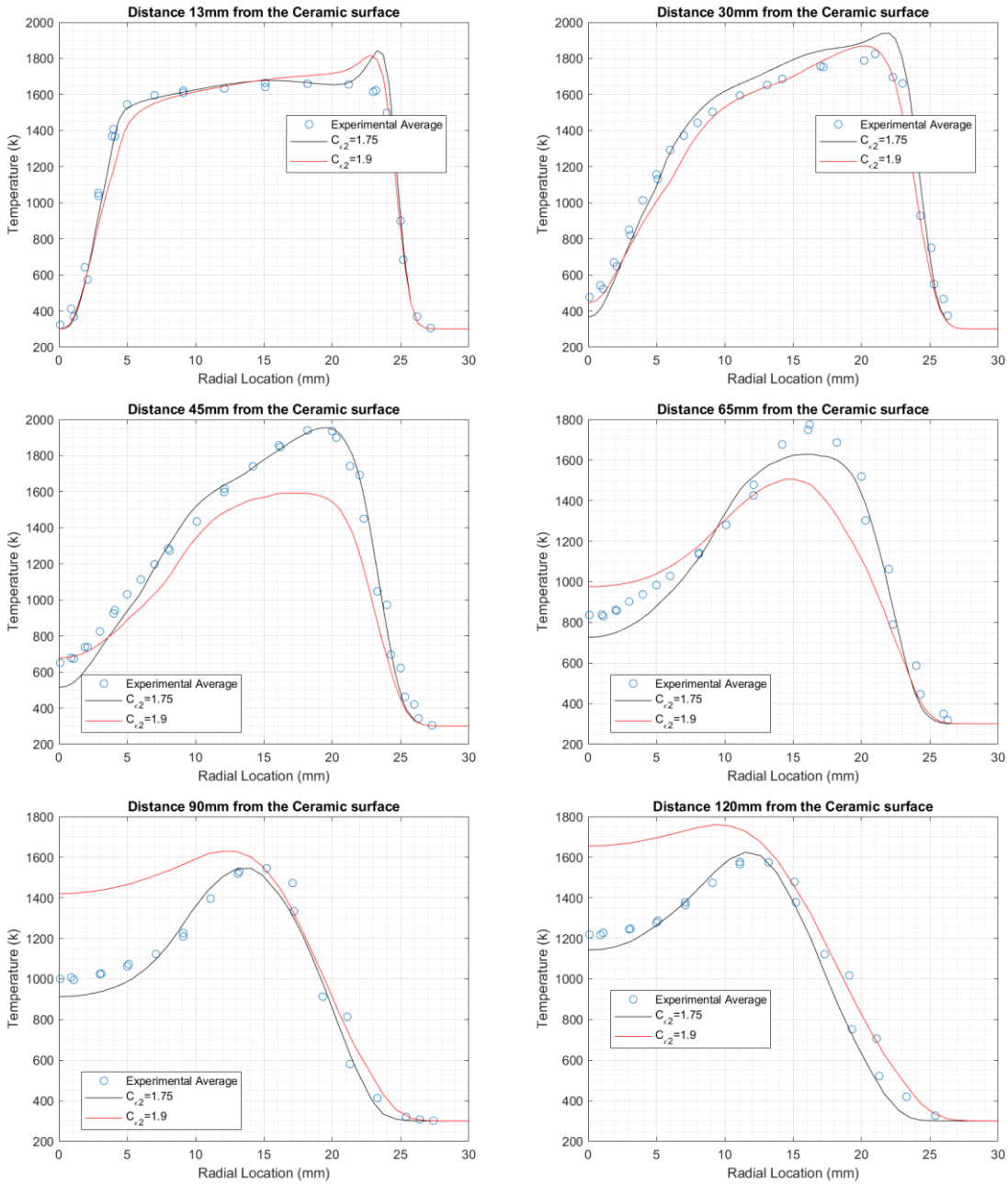

Figure 4.11 Radial profile of the temperature.(modified and default turbulence model).

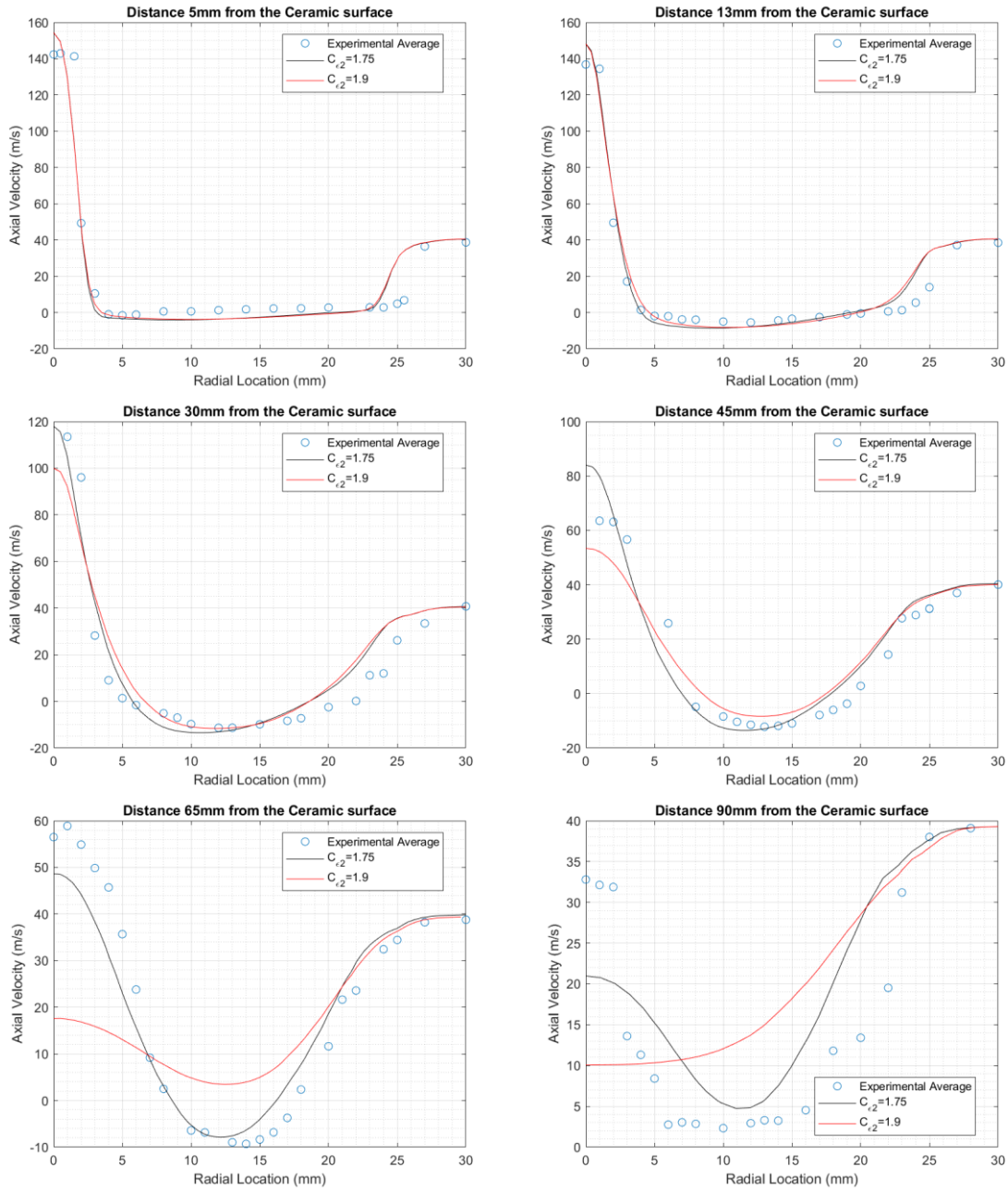

Figure 4.12 Radial profile of axial velocity.(modified and default turbulence model).

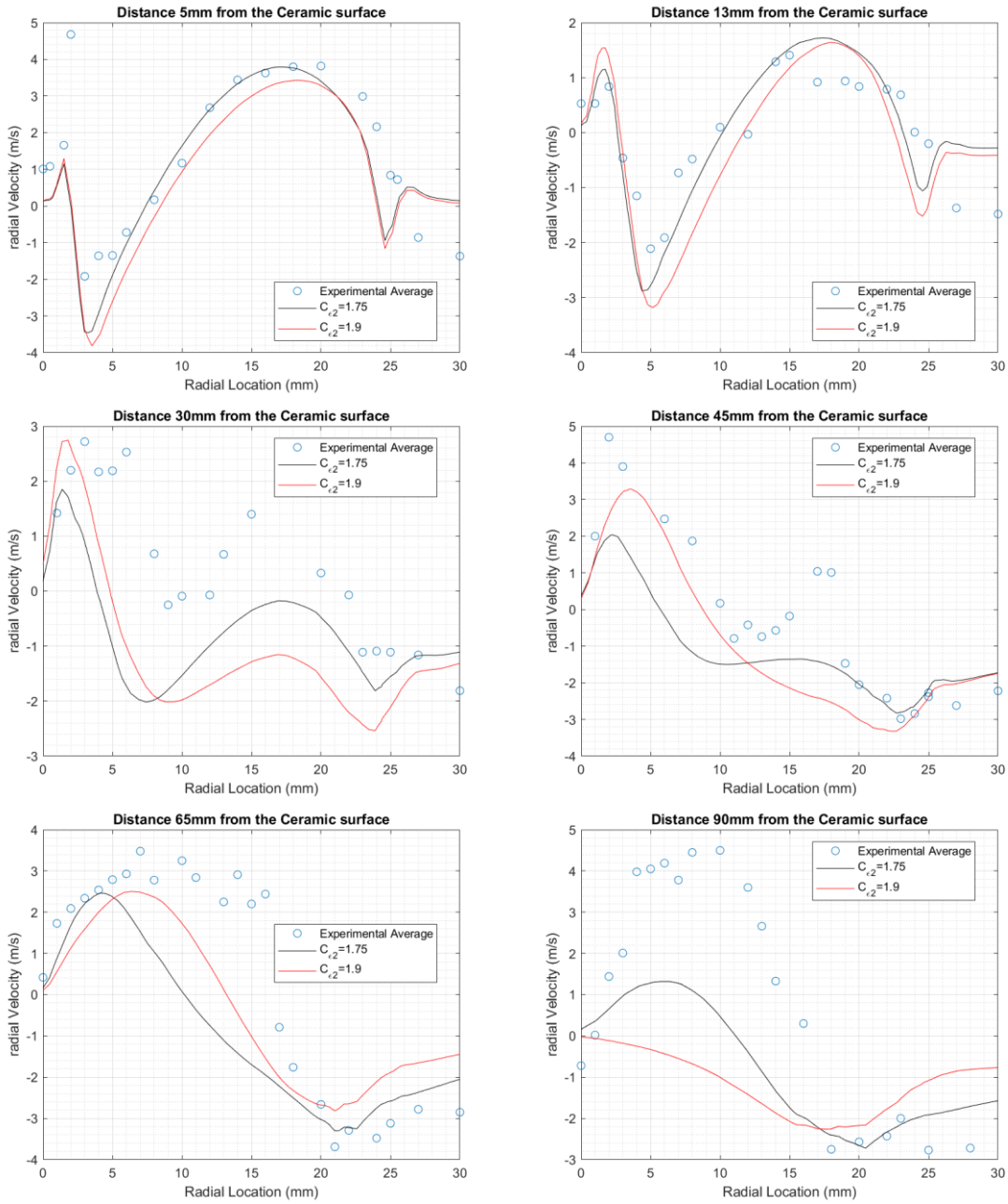

Figure 4.13 Radial profile of the radial velocity.(modified and default turbulence model).

4.6 Comparison between the Standard and Realizable k-e model

The comparison of measurements and the numerical predictions for two turbulence models with experimental results are provided here. It is important to have a good estimation of the flow and consequently mean mixture fraction because all the other estimations are highly affected by it. Considering the low stoichiometric mixture fraction for the methane/hydrogen (0.05) any error in this part can cause fast/slow combustion and very big error in the temperature field and the combustion products.

Figure 4.14 illustrates how the mean mixture fraction is predicted by both the models. Both of them predicted the mean mixture fraction very accurately, but the realizable model can provide more realistic behavior for the fmean in the higher distance from the ceramic surface. The effect of very slight errors become more evident by comparing Figure 4.14 and Figure 4.15. In the closer distances from the ceramic surface, even the slightest errors (0.01) in the mean mixture fraction causes significant temperature overprediction (around 200K). The reason behind this problem as explained before is that the fuel reacts in this zone and produces more heat. By looking into the 90mm and 120mm it is noticeable how this error increases by adding the effect axially.

In Figure 4.16 the axial velocity is predicted quietly acceptable for both cases but due to the higher decay rate of the standard model, the velocity decreases much faster than it should do and causes to shift the combustion into the recirculation zone.

Figure 4.17 shows how the radial velocity is predicted by both of the models. Again realizable can predict it accurately so the structure of the recirculation zone is much more realistic.

Figure 4.18 and Figure 4.19 are providing a side by side view of the mean mixture fraction and the temperature field. The standard model is some sort of compressing the combustion into the recirculation zone and makes a poorer prediction compared to the realizable model. This is very important for other steps which are NOx

modeling and Soot modeling since these models are highly sensitive to the temperature fields.

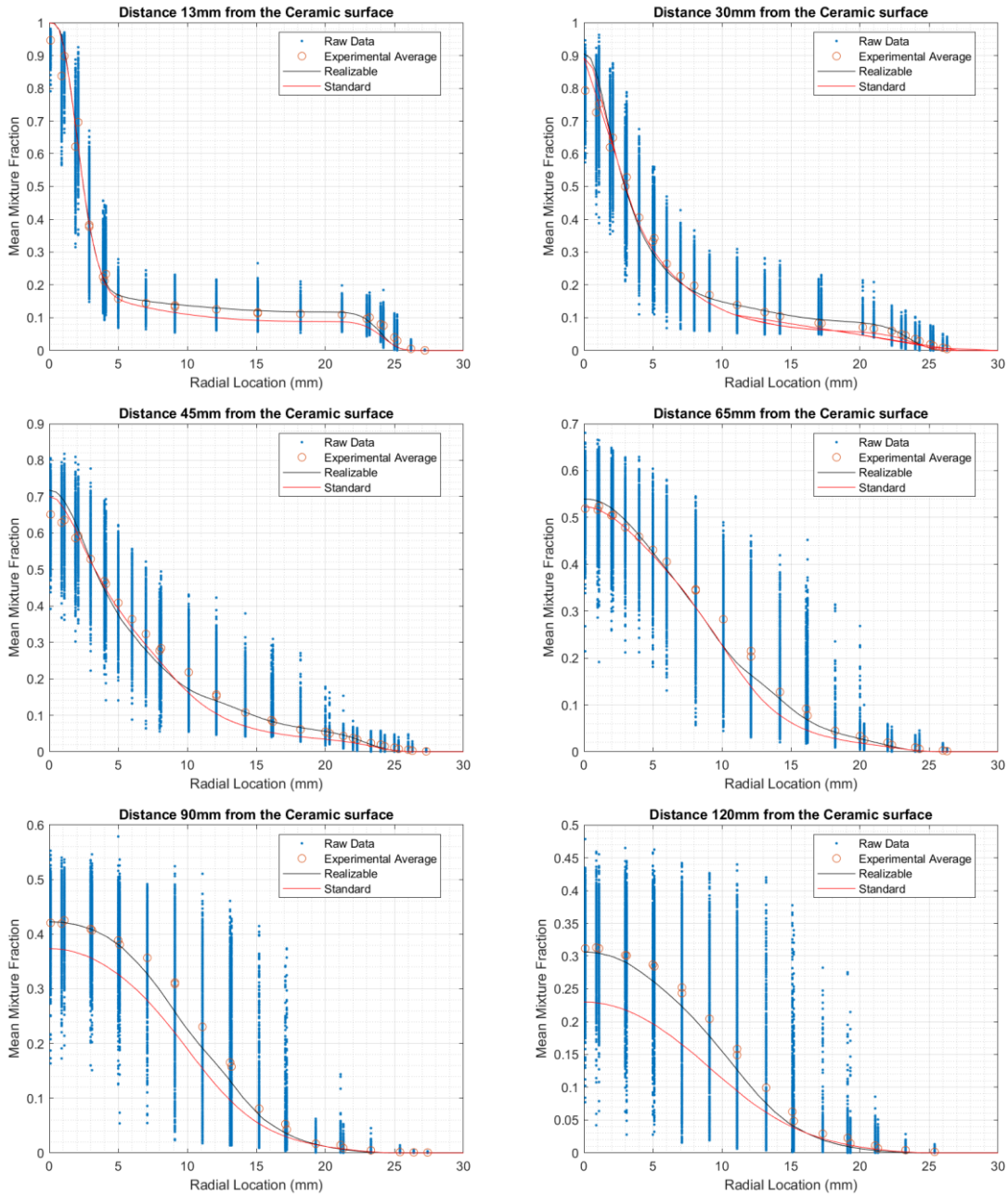

Figure 4.14 Radial means of mean mixture fraction.

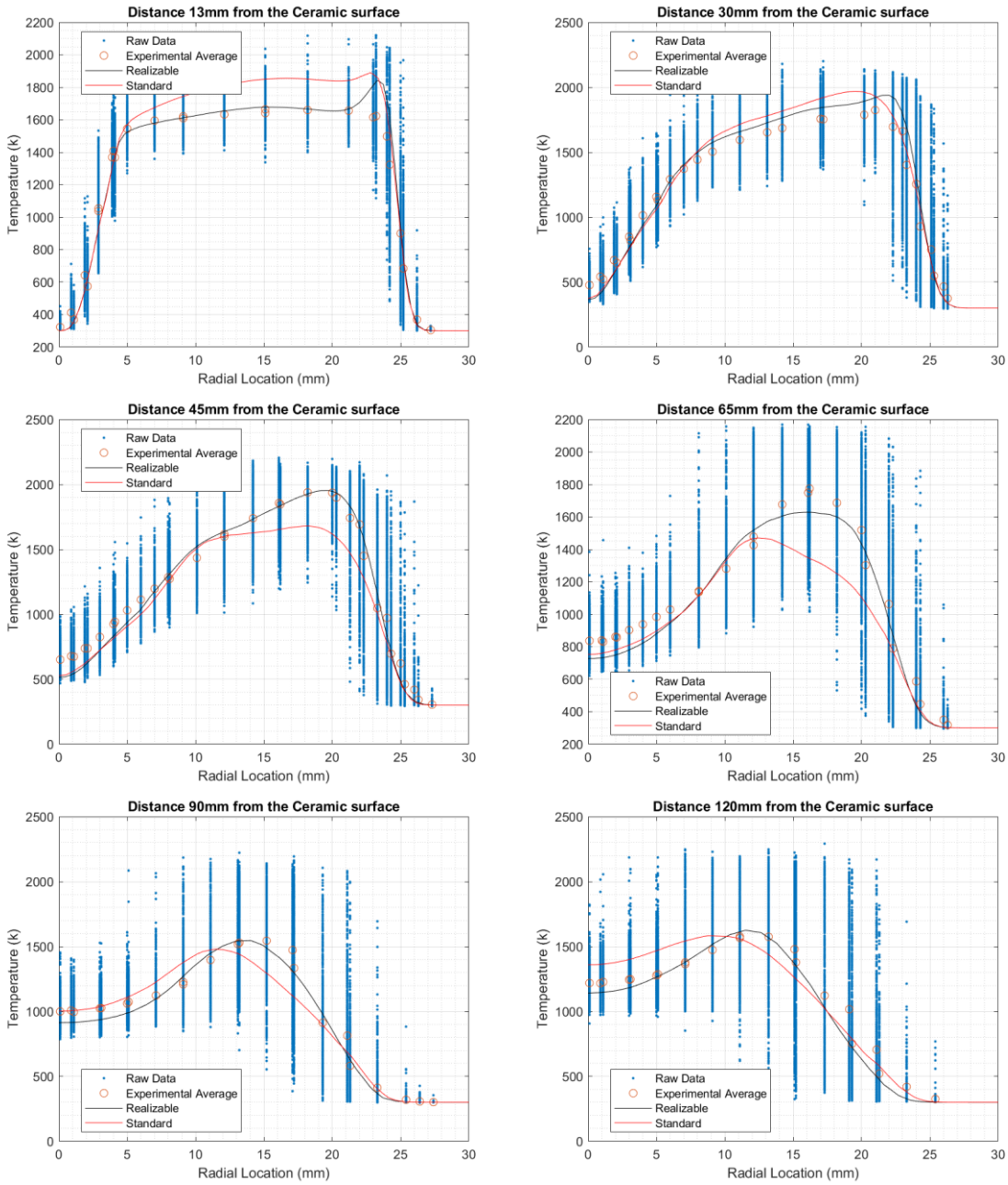

Figure 4.15 Readial mean of temperature.

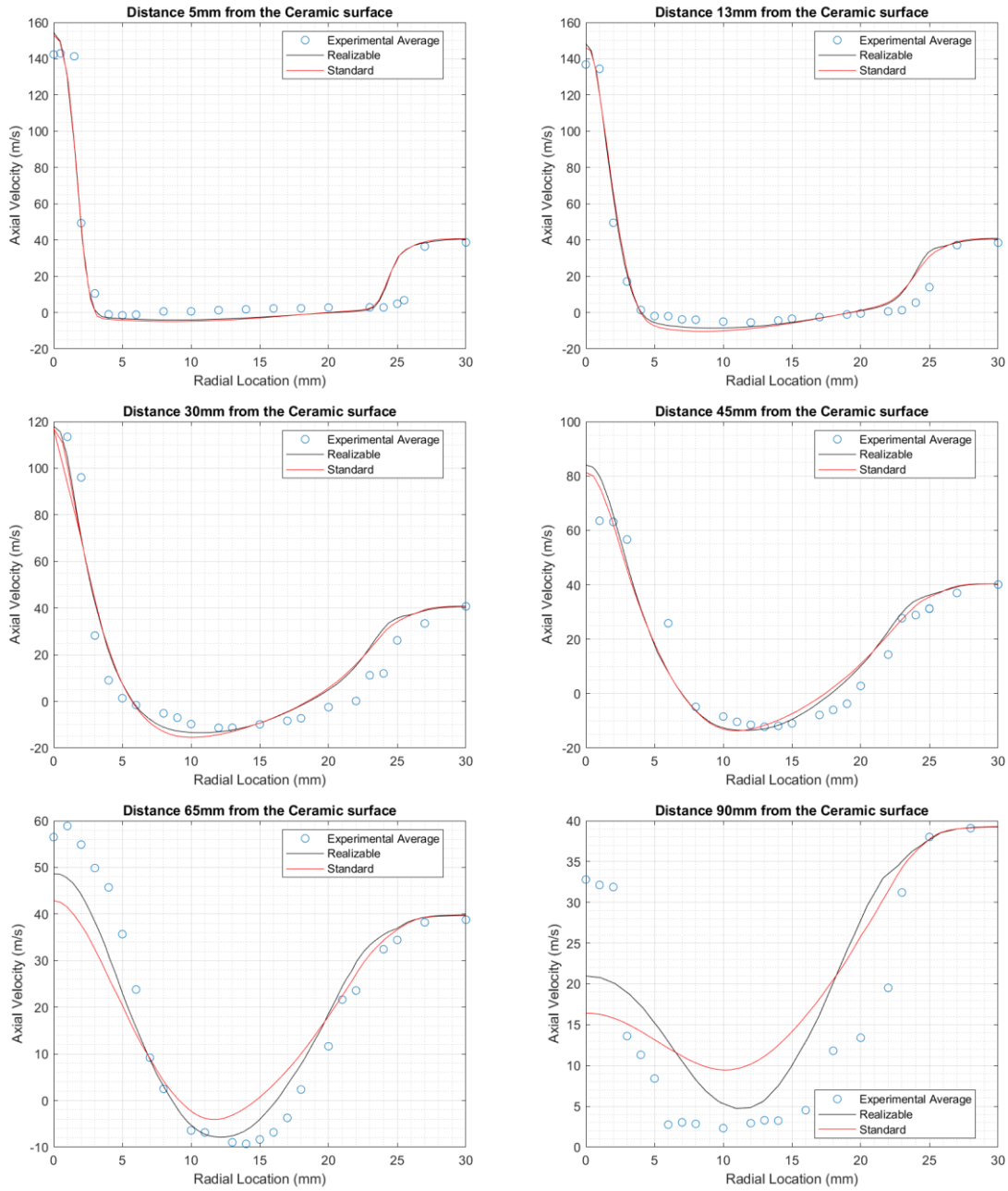

Figure 4.16 Radial means of the axial velocity.

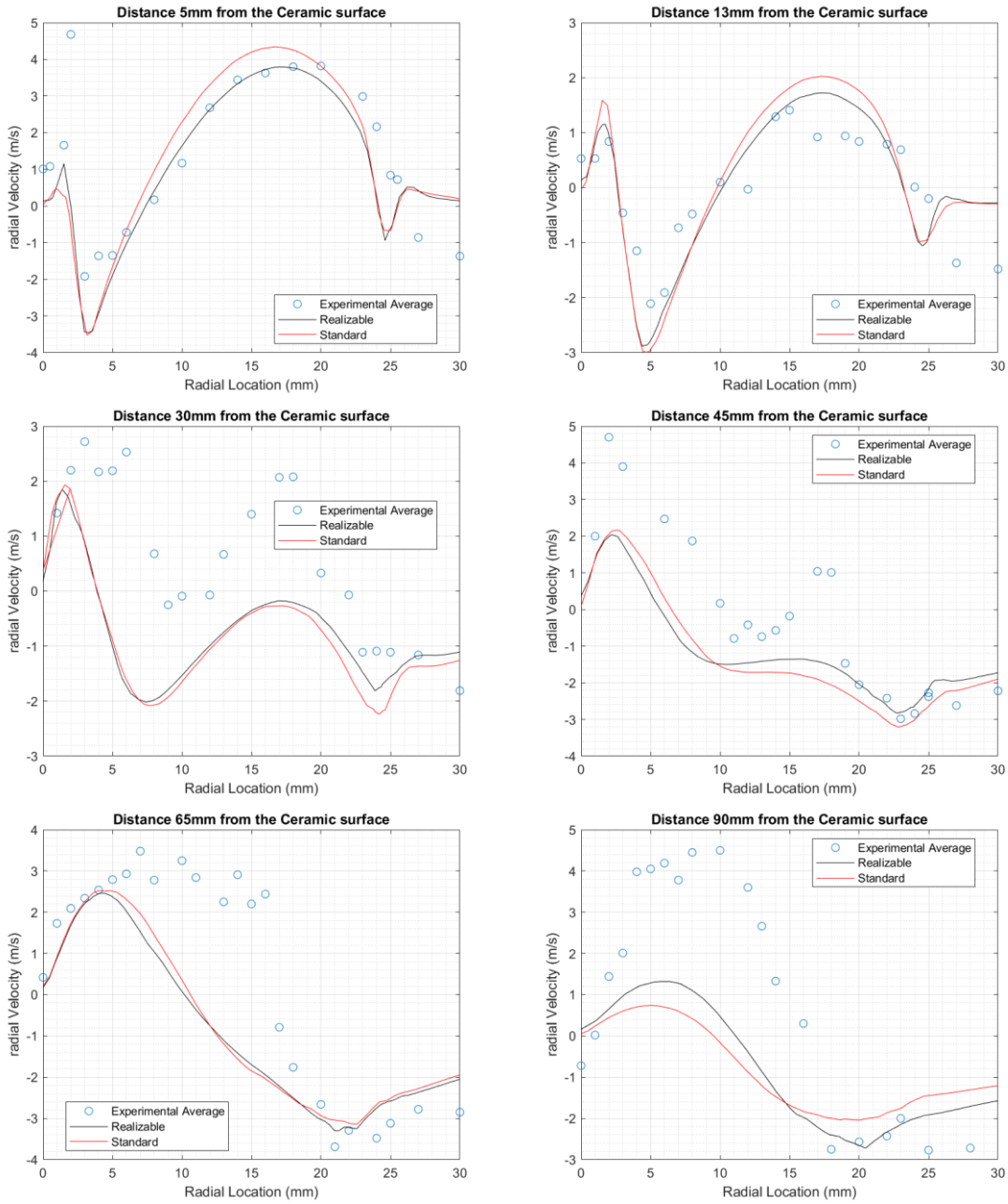

Figure 4.17 Radial means of the radial velocity.

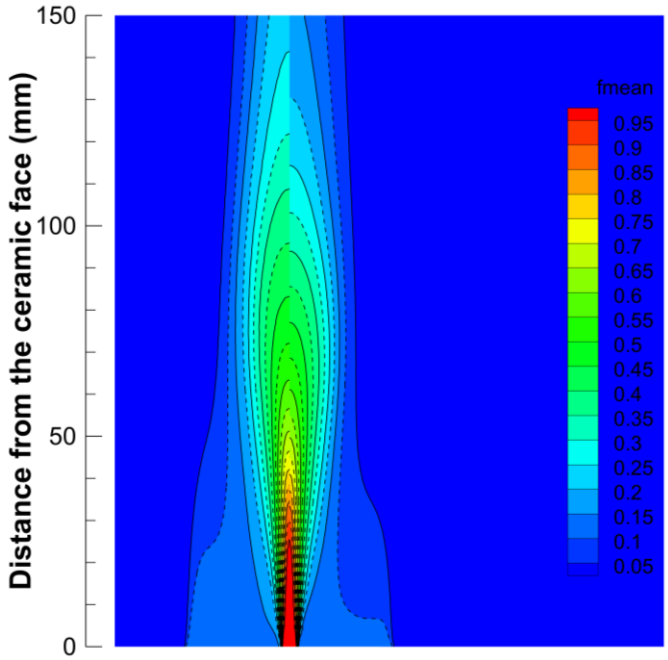

Figure 4.18 Mean mixture fraction contour. Realizable-Standard k-epsilon model.

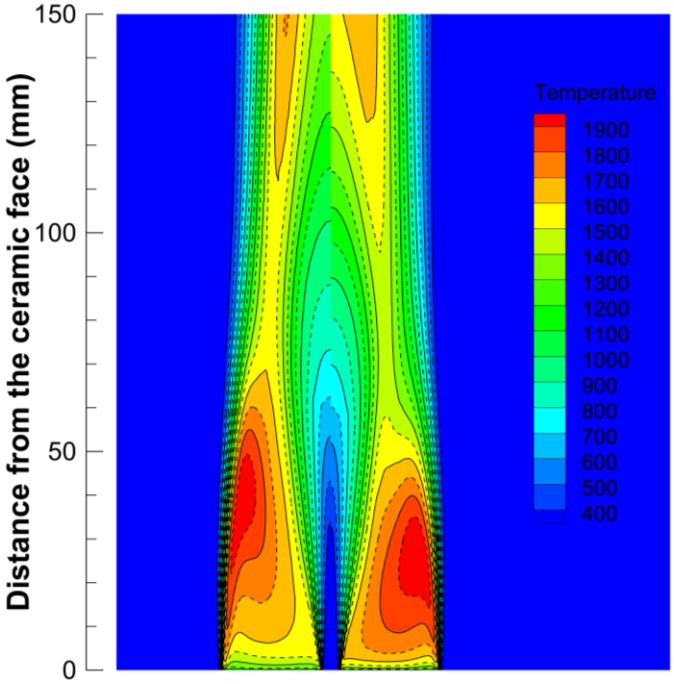

Figure 4.19 Temperature contour. Realizable-Standard k-epsilon model.

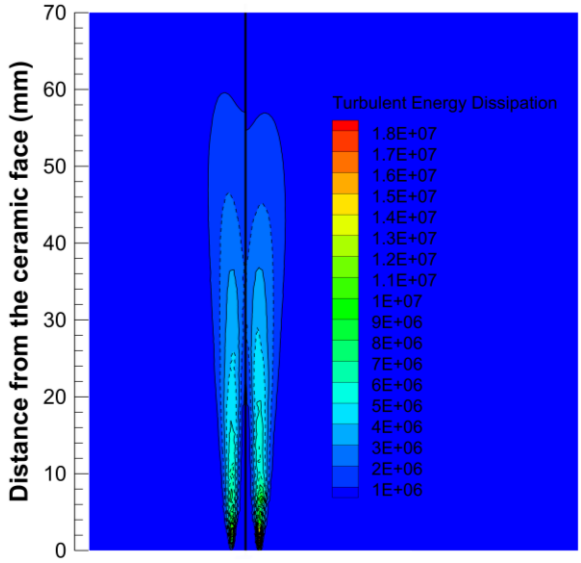

Figure 4.20 Turbulent energy dissipation contour. Realizable-Standard k-epsilon mode.

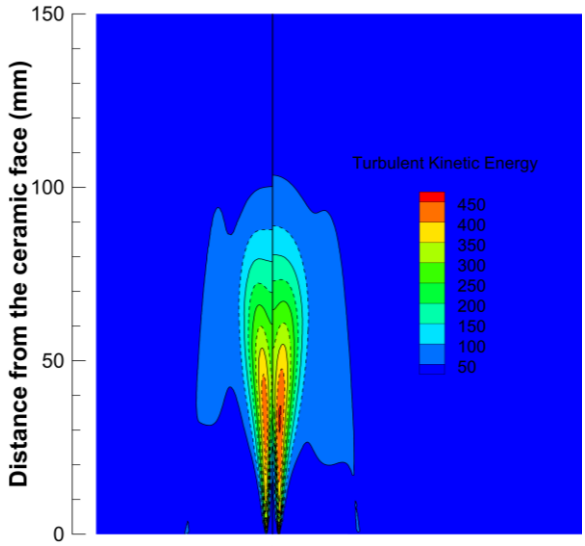

Figure 4.21 Turbulent kinetic energy contour. Realizable-Standard k-epsilon mode

4.7 Comparing The Flamelet Model With The Equilibrium Model

As it is explained in Section (2.5.1) and (2.5.2) the chemical equilibrium does not consider the heat gain/loss in the combustion. All the variables are calculated using the only and only mean/variance mixture fraction. By looking into the mean mixture fraction contour represented in Figure 4.22 and radial means presented in Figure 4.24 it is evident that the mean mixture fraction is more or less identical in both cases especially in the regions close to the recirculation zone. The reason behind this similar prediction is explained in the second chapter, the mean mixture fraction is solved based on the flow field which can be illustrated by looking into Figure 4.24.

But looking into the temperature profiles in Figure 4.23 and the chemical equilibrium provides a very unrealistic prediction. The reason behind this issue is only addressed in the method of solving the combustion.

Figure 4.40 and Figure 4.41 shows the O2 and N2 percentage. Both of the cases were able to predict very well, but the equilibrium model was performing a better prediction for the oxidizer which is quite interesting.

As it is explained in previous chapters about methane combustion, methane has a slow kinetic compared to other hydrocarbons. Looking into Figure 4.30 and Figure 4.31 shows how the chemical equilibrium fails in the prediction of the H2 combustion. The steady flamelet model has a very good prediction of the H2 combustion and consequently higher H2O which is due to the slower process of the Methane. Flamelet model has a minor under prediction which is due to GRI.MECH kinetic library.

Figure 4.32 compares the CO in both cases. Due to a higher rate of combustion dedicated to methane in equilibrium, the product of its combustion (CO) is highly overestimated which makes this model failed for methane combustion next to other fuels.

Figure 4.33 shows a slight overprediction of the CO2 at 90mm and 120mm in the case of the flamelet model. The reason behind this can be due to the “steady”

flamelet model which does not take into account the partially in equilibrium species.

Figure 4.34 shows how well the flamelet model can predict OH combustion. Chemical equilibrium fails in this part.

It is noticeable by looking into Figure 4.35 the agreegate NO prediction is acceptable and it shows how the thermal NOx is modeled due to good predictin of the temperature profile.

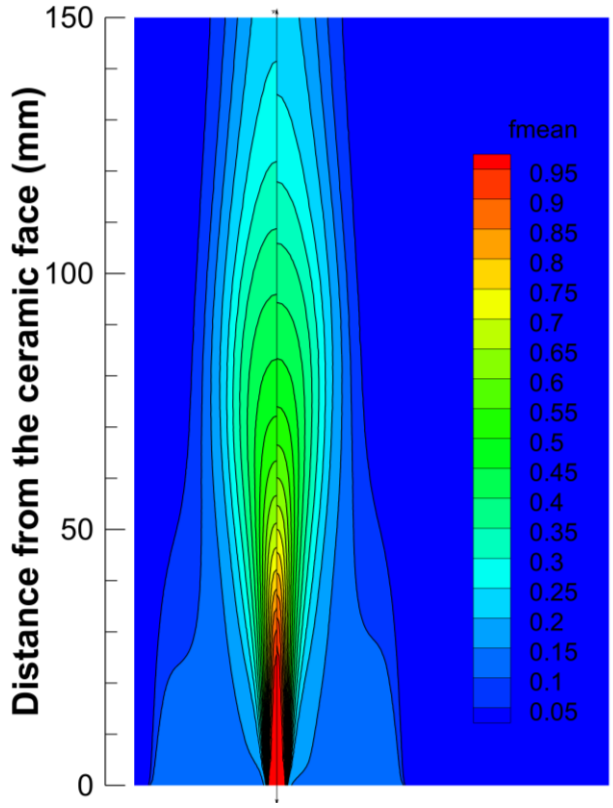

Figure 4.22 Mean mixture fraction contour (left flamelet model and right chemical equilibrium model).

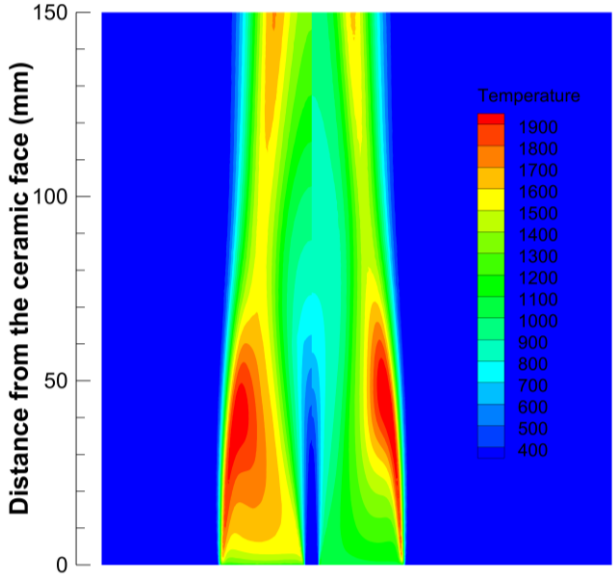

Figure 4.23 Temperature contour (left flamelet model and right chemical equilibrium model).

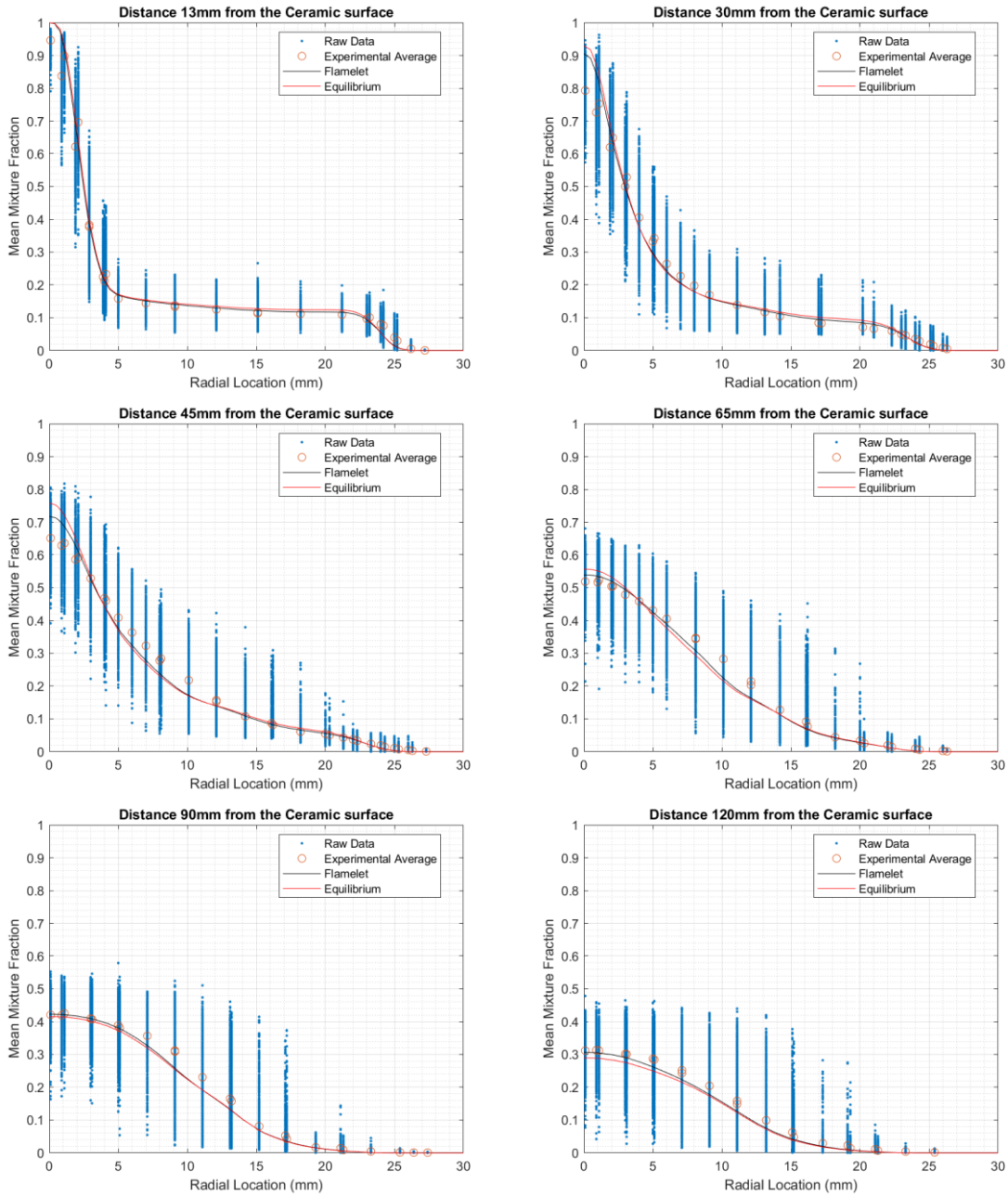

Figure 4.24 Radial profile of the mean mixture fraction in the HM1 flame.

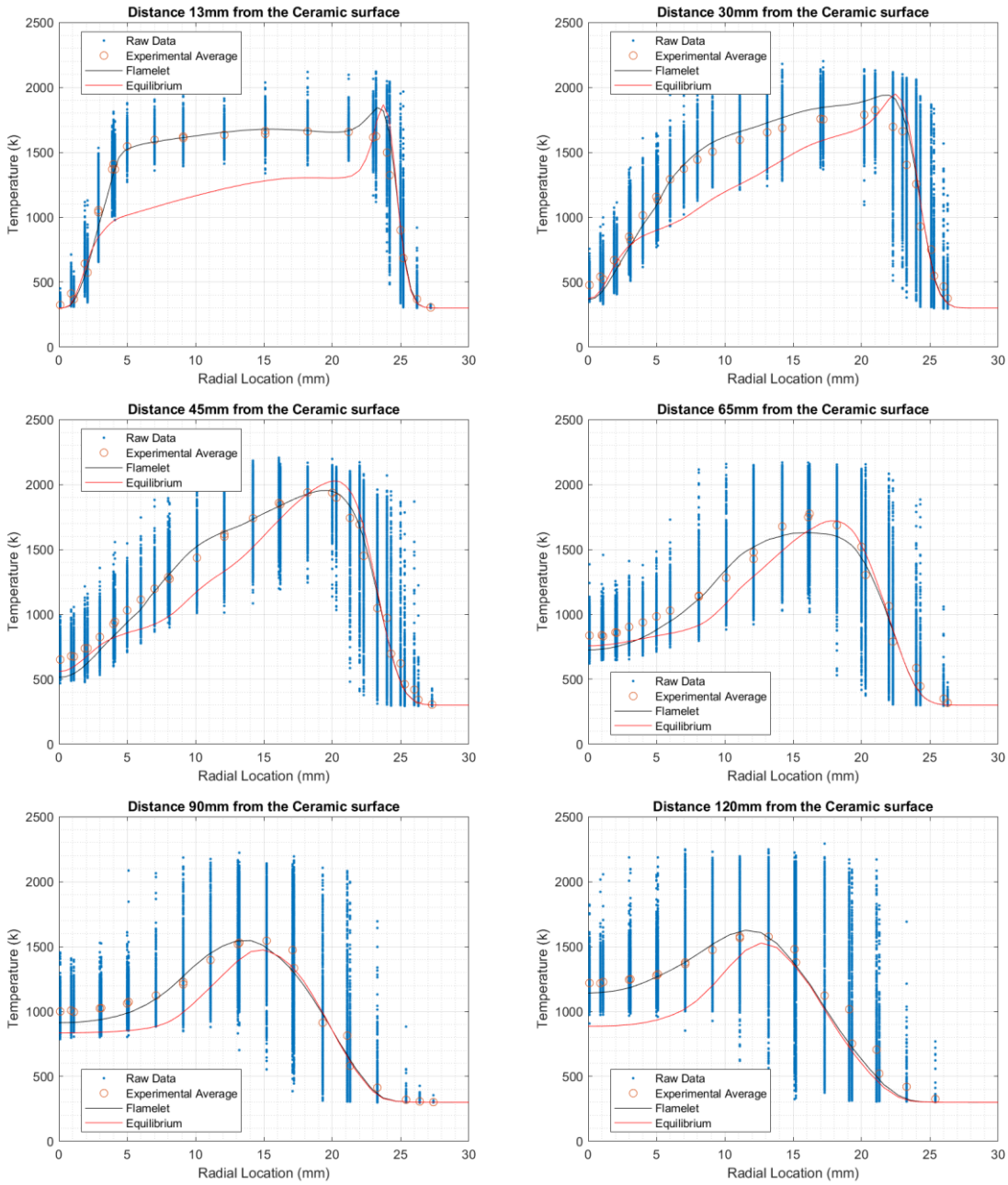

Figure 4.25 Radial profile of the temperature in HM1 flame.

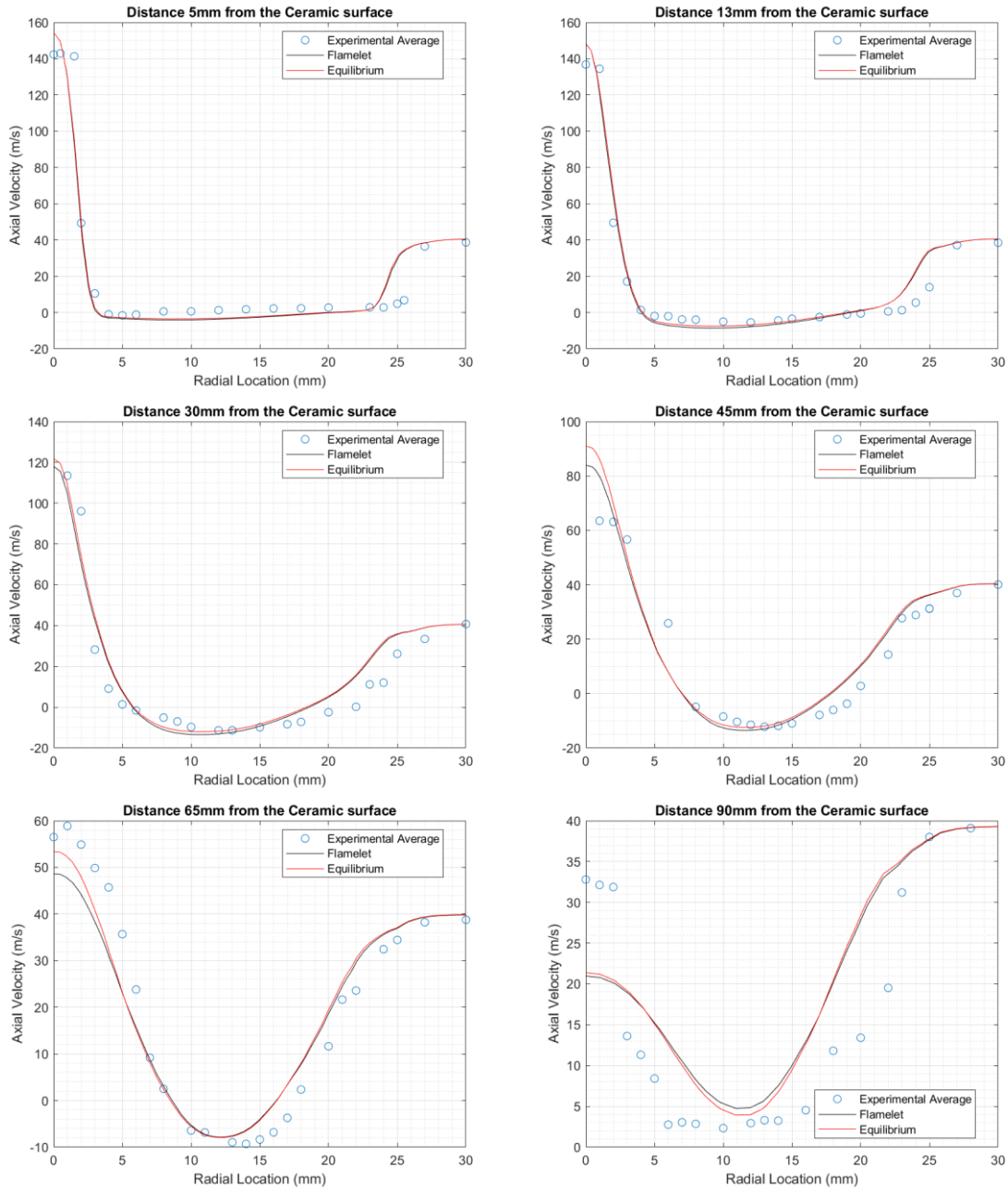

Figure 4.26 Radial profile of the axial velocity in HM1 flame.

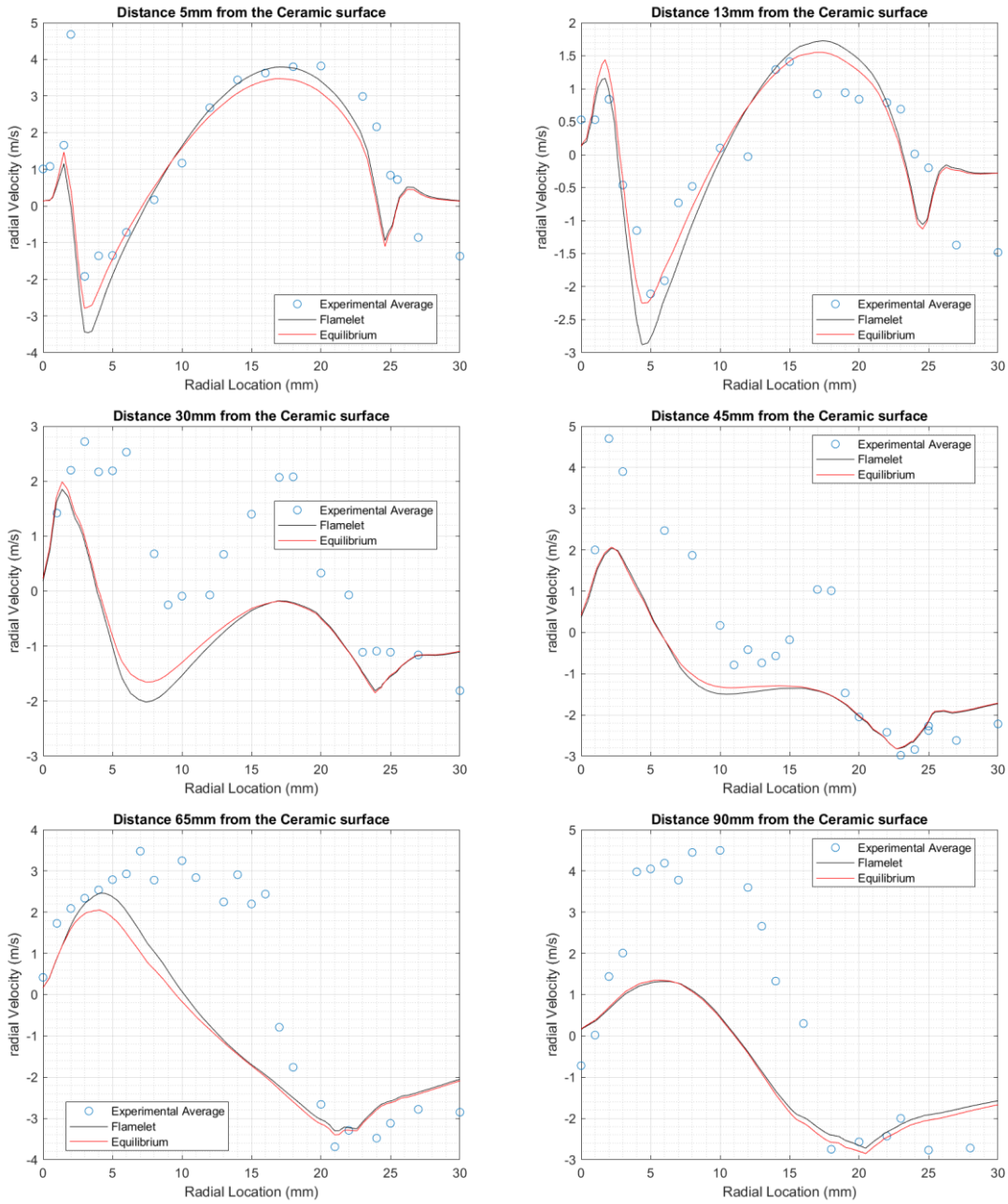

Figure 4.27 Radial profile of the radial velocity in HM1 flame.

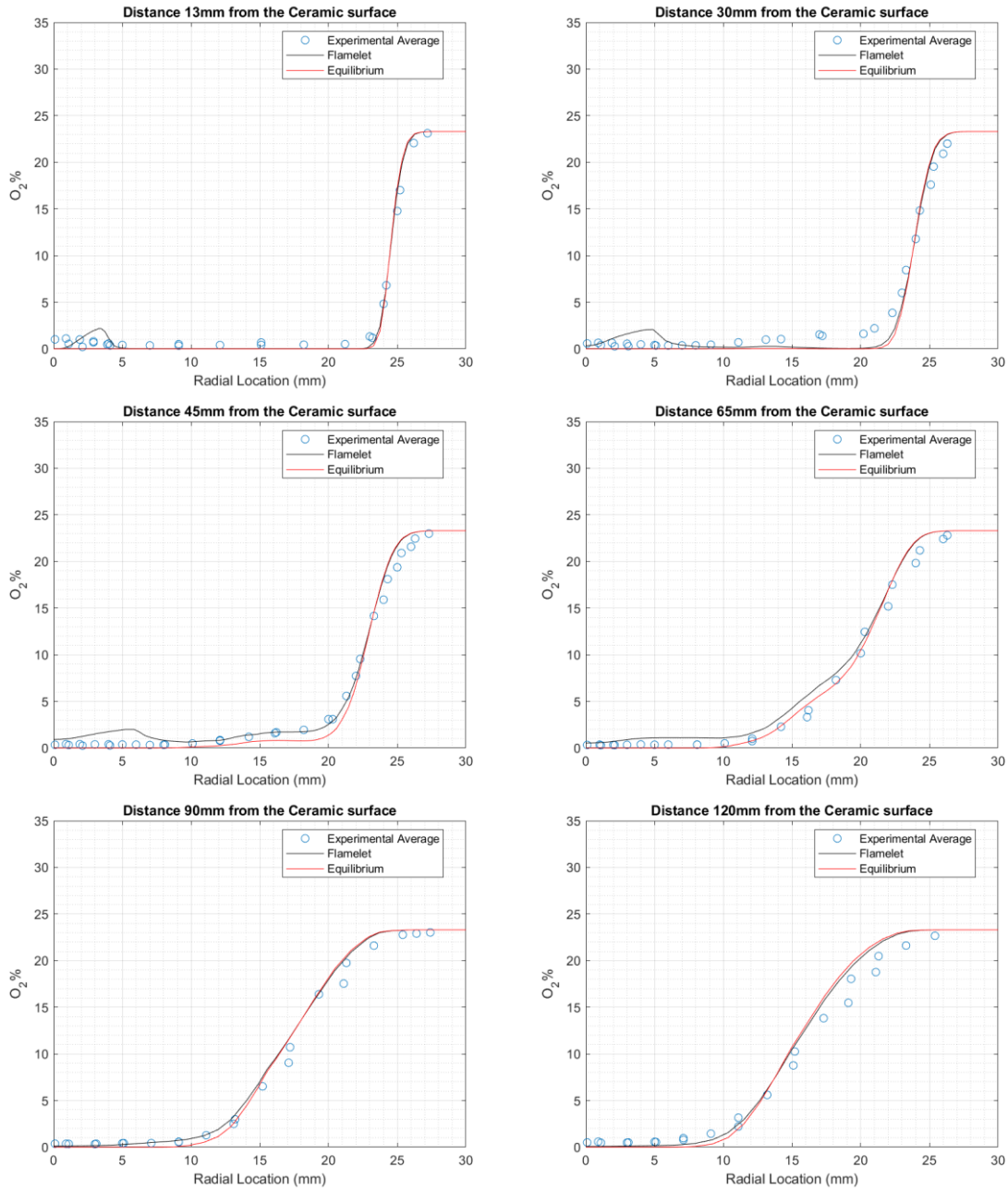

Figure 4.28 Radial profile of the O2 in HM1 flame.

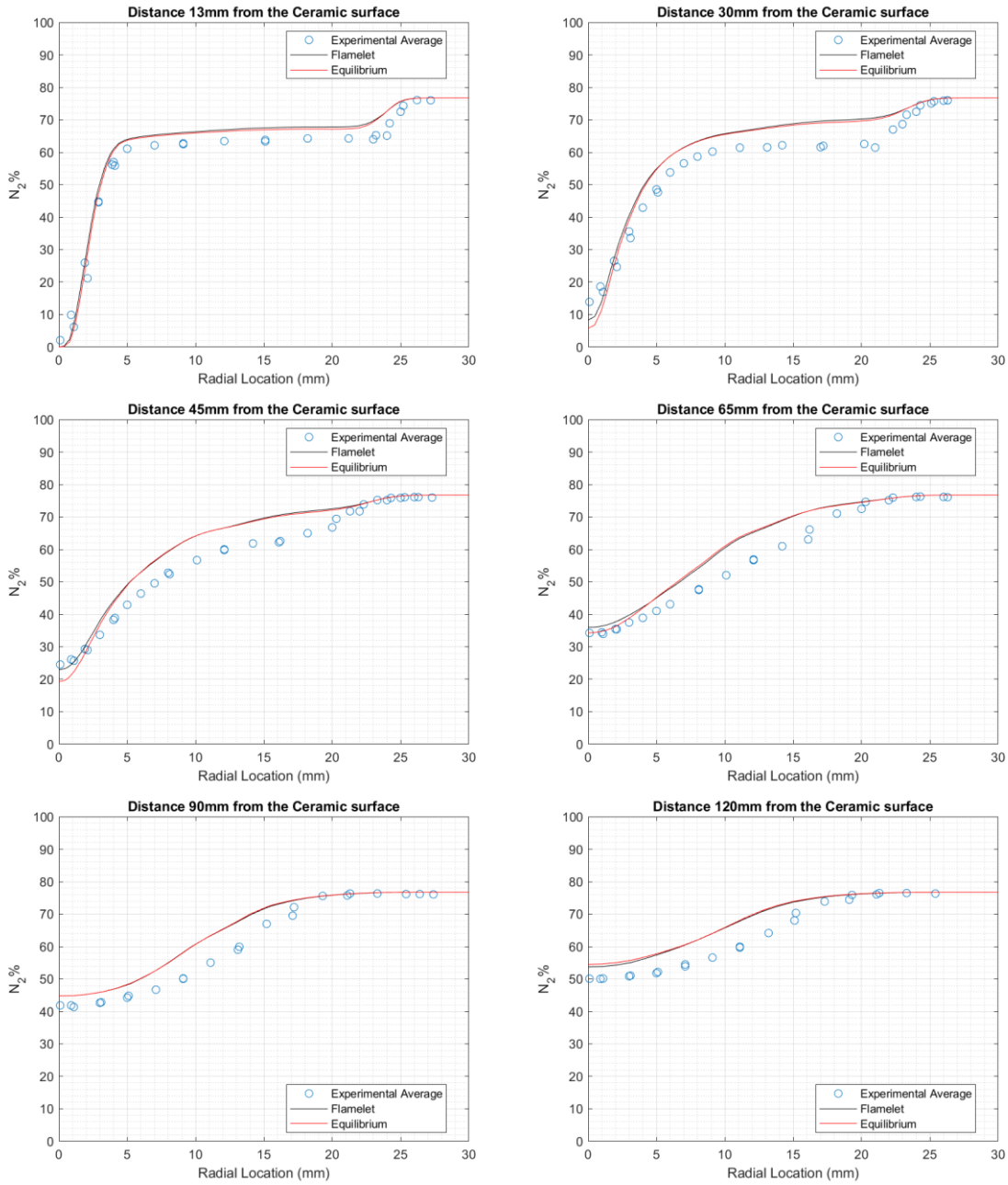

Figure 4.29 Radial profile of the N2 in HM1 flame.

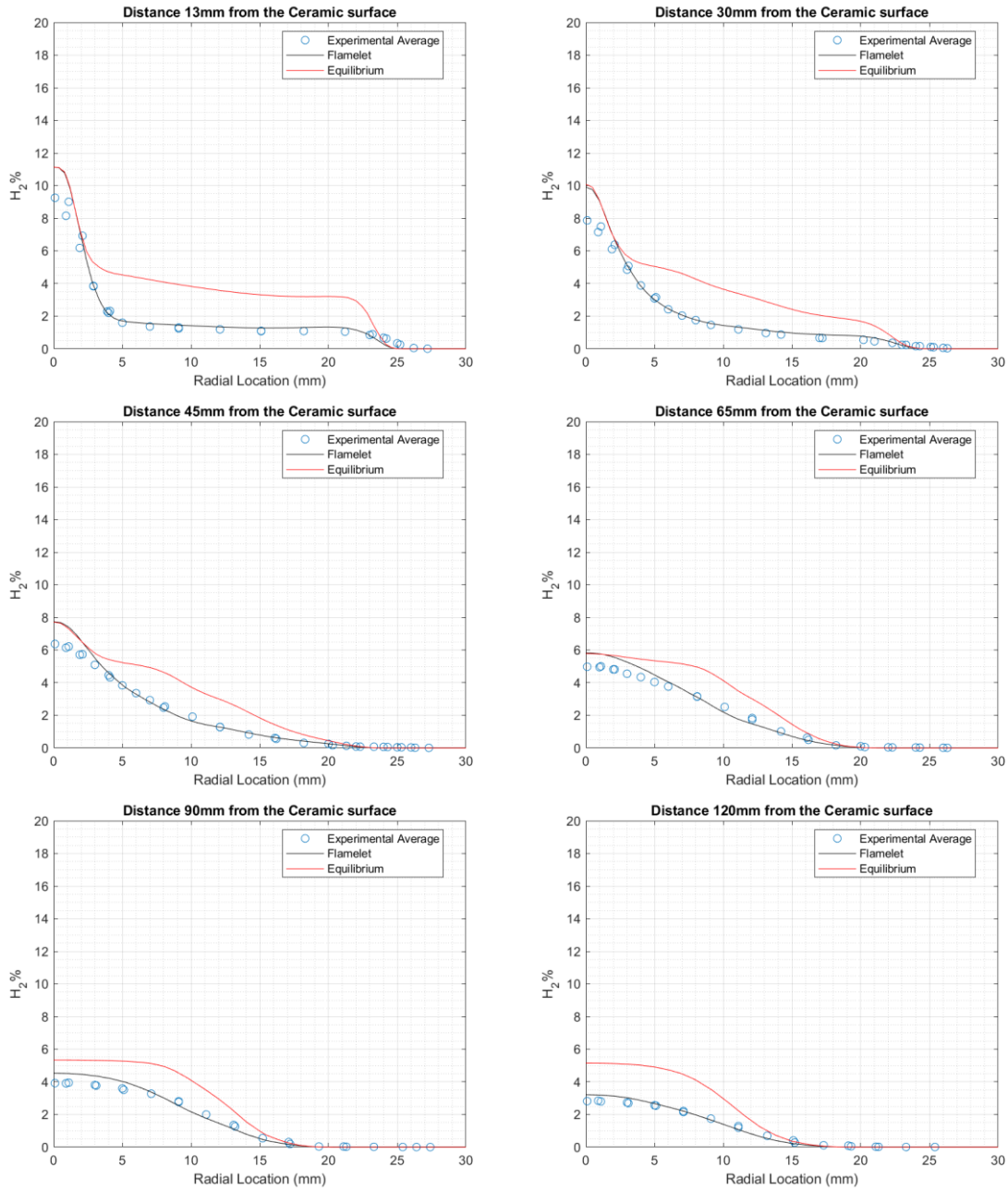

Figure 4.30 Radial profile of the H2 in HM1 flame.

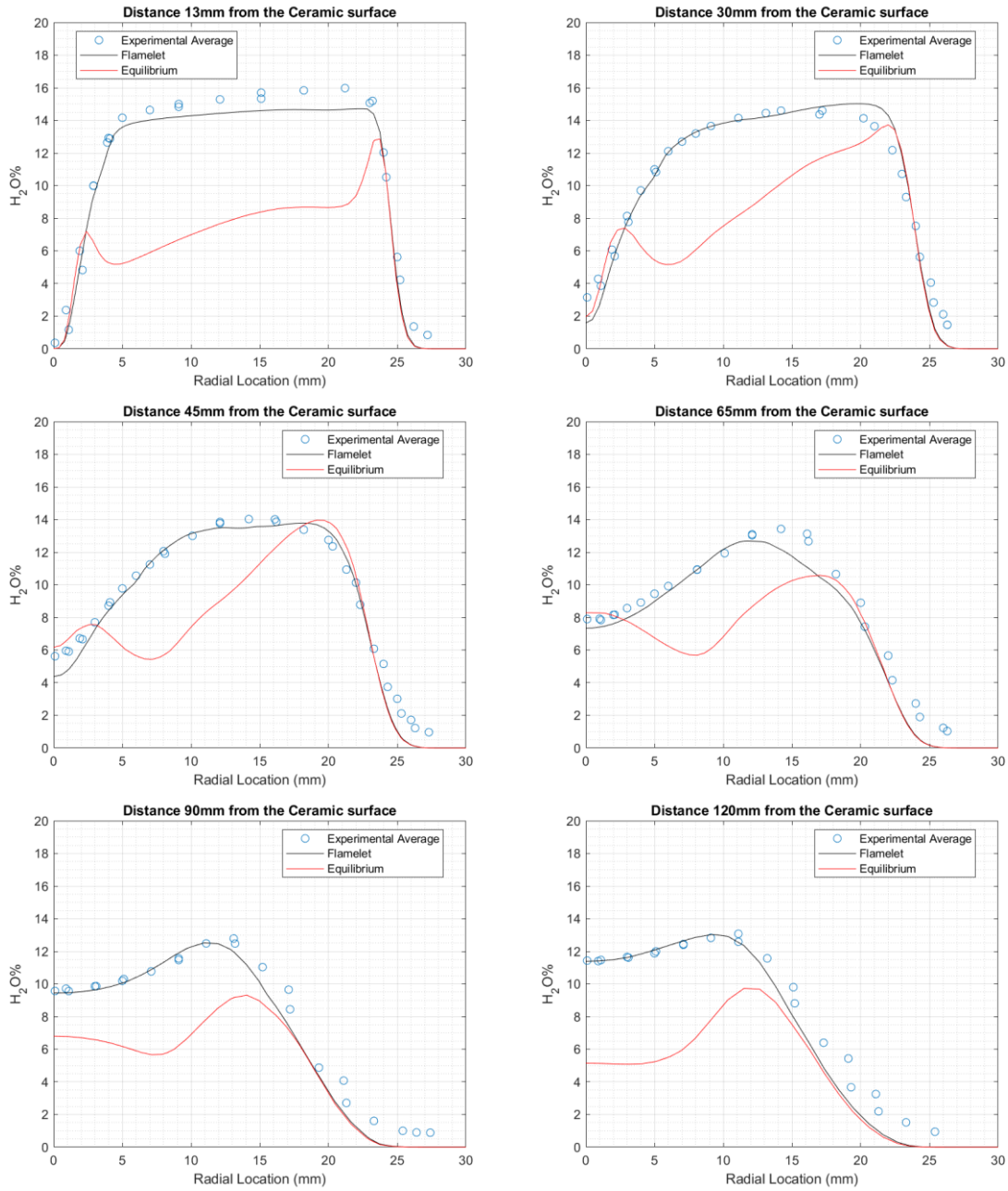

Figure 4.31 Radial profile of the H2O in HM1 flame.

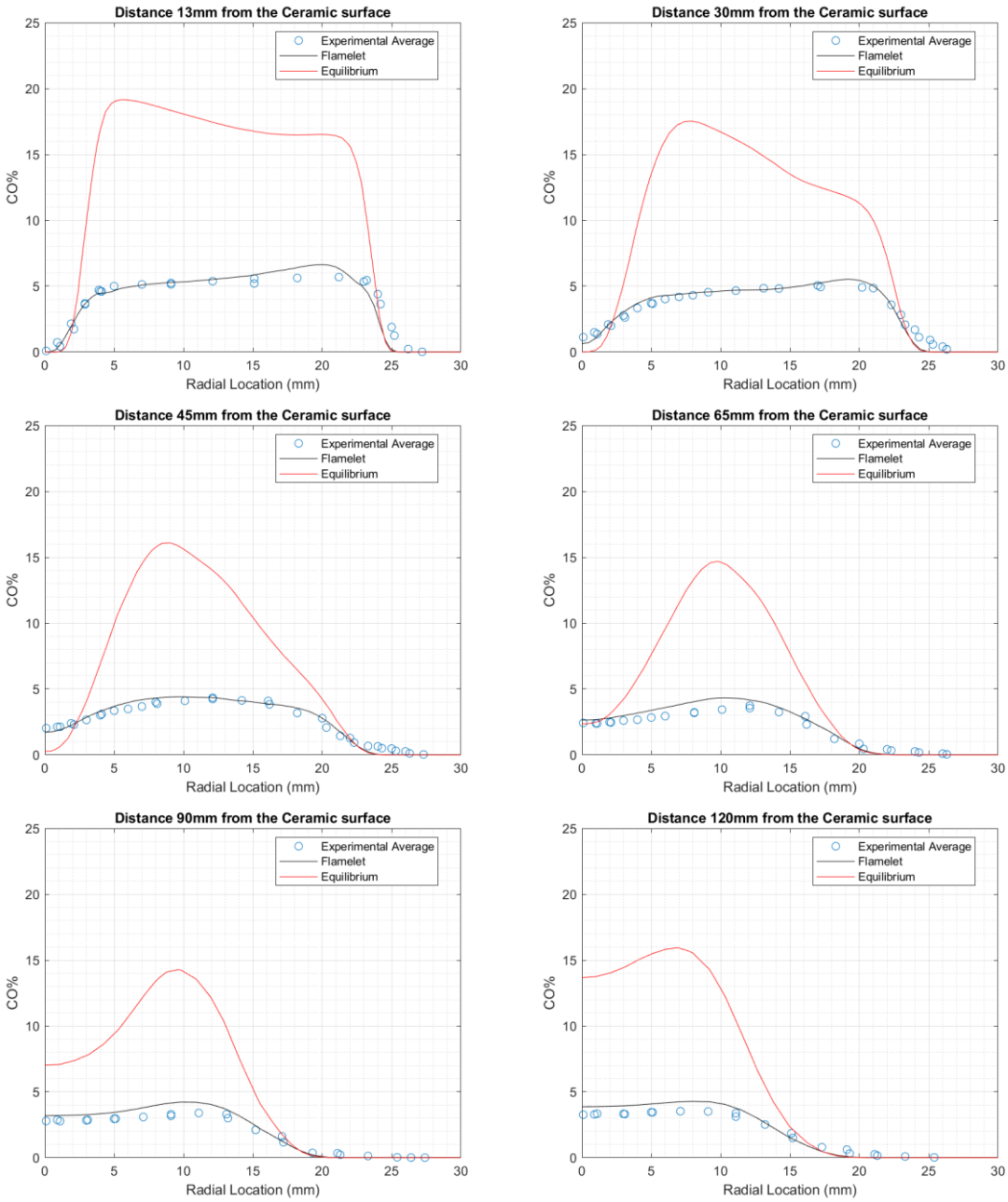

Figure 4.32 Radial profile of the CO in HM1 flame.

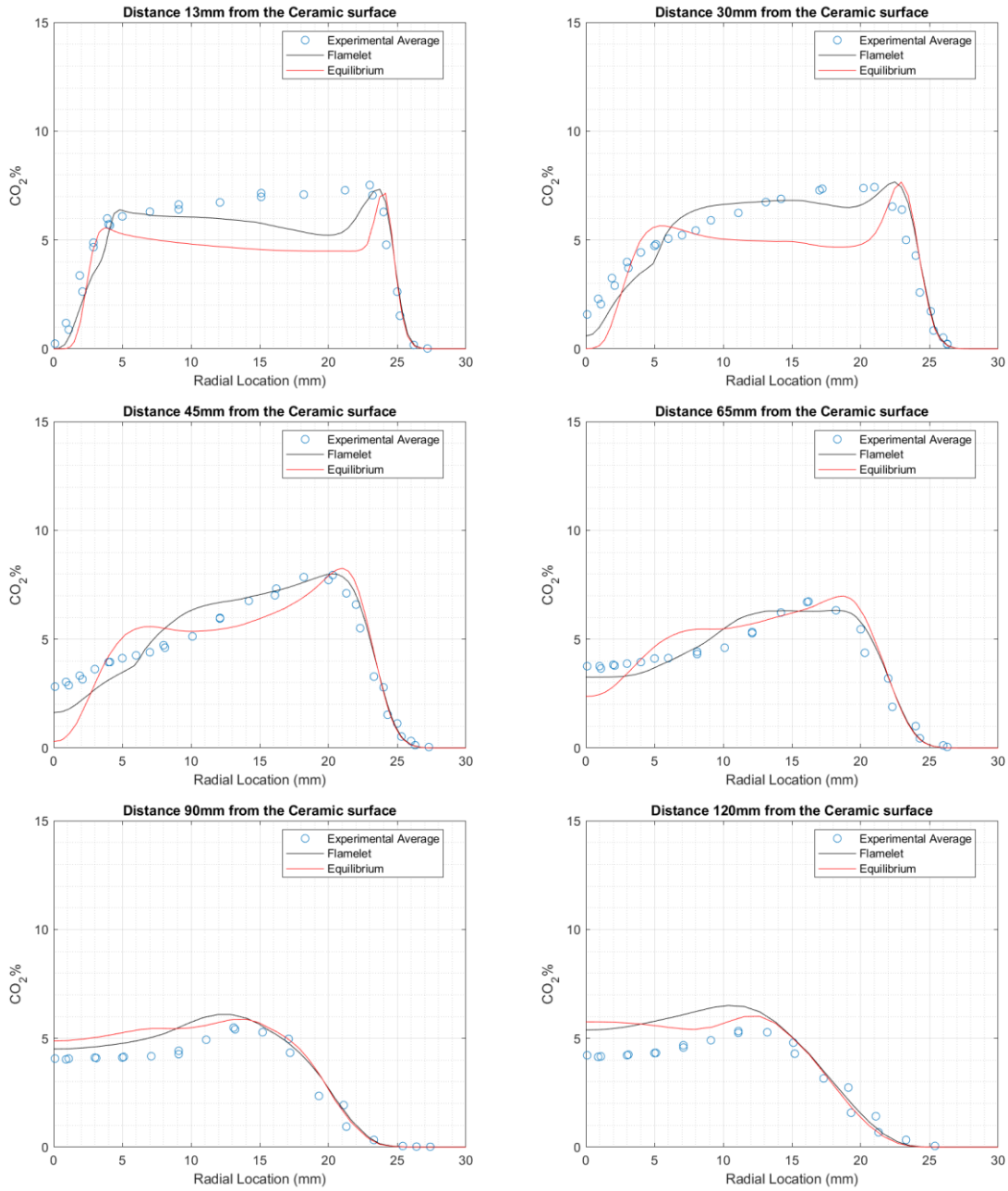

Figure 4.33 Radial profile of the CO2 in HM1 flame.

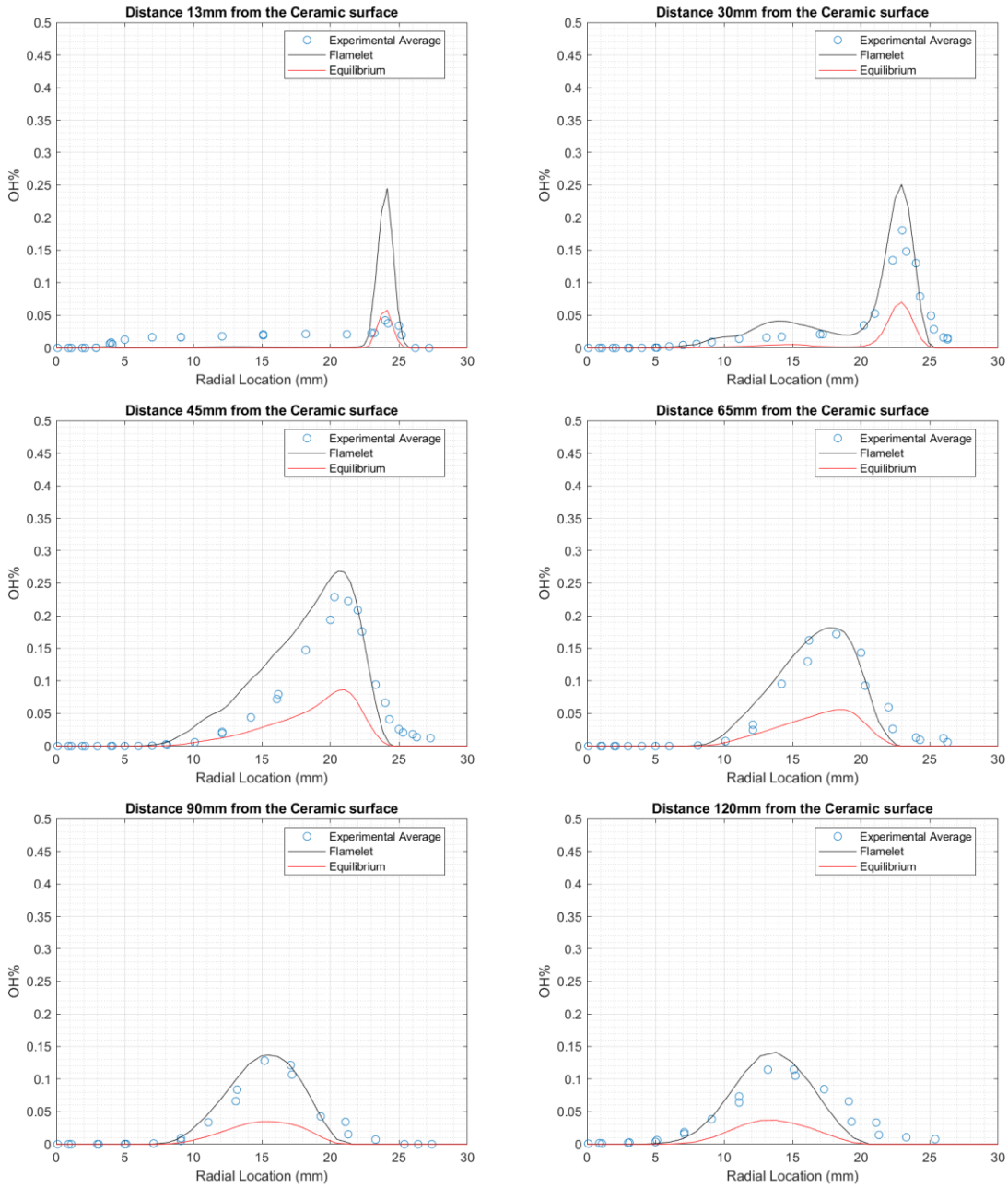

Figure 4.34 Radial profile of the OH in HM1 flame.

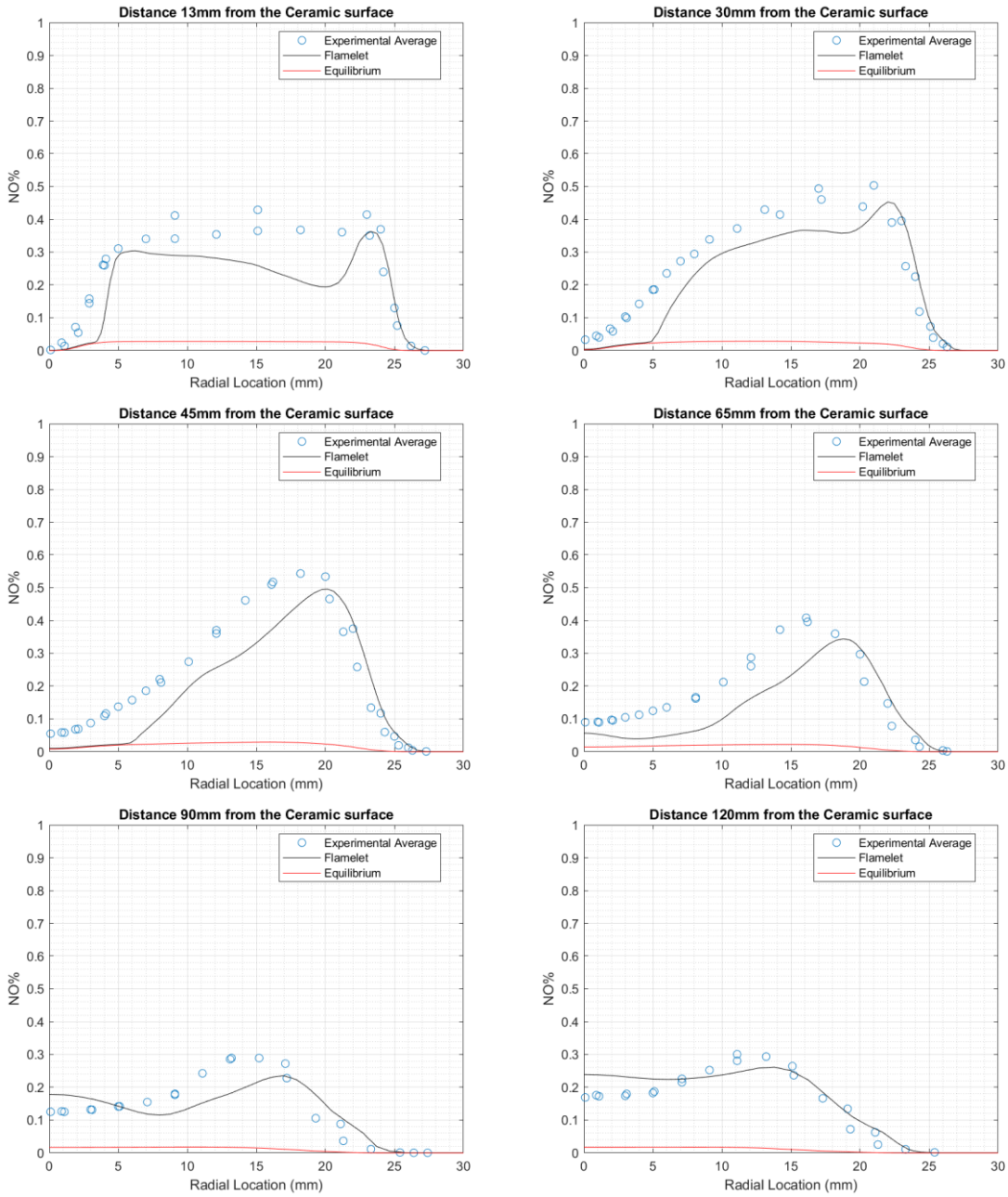

Figure 4.35 Radial profile of the NO (×100) in HM1 flame.

4.8 HM2 flame

In previous sections, the difference between different turbulence models and combustion models is explained in detail. It is noticeable how the realizable k-epsilon model and steady flamelet model is capable of adequate prediction of the CH_4/H_2 combustion. HM2 flame is a good candidate to see how does the model perform in case of a different blow-off velocity. In this section the comparison of measurements and the numerical predictions for two HM2 flame (mean velocity of 178 $\frac{m}{s}$ and 75% of blow-off velocity) with experimental results are provided.

The mean mixture fraction in Figure 4.38 is predicted very well which means the model can solve the flow field identical with the experimental results. Unfortunately, there are no data to compare the velocity fields like the previous case (HM1 flame). It is necessary to address the issue with slight over predicton in the recirculation zone, which means that the computed results considers the combustion less in this zone.

Figure 4.39 shows how the temperature field is adequately well predicted. A slight under-prediction of the temperature can be the result of the under-prediction in the mean mixture fraction which shows the significance of flow field importance and turbulence interaction.

Looking into the O_2 profile reported in the Figure 4.40 shows overestimation in the recirculation zone that is the indicator of the underprediction in the combustion. This shows how the low stoichiometrc ratio of this fuel (0.05) can cause big errors in the species values.

The aggregate prediction of the H2 and the H2O is acceptable just there is a slight under-prediction in the recirculation zone which is illustrated in Figure 4.43 and Figure 4.42.

Generally, the trend of the CO2 and CO is very similar to the experimental result. There are some errors in different zones which are due to non-equilibrium species and kinetic library.Figure 4.44 and Figure 4.45 shows how the average results become realistic by increasing the distance from the recirculation zone.

Even though the OH prediction is not identical with experimental data Figure 4.46 shows how the peak of the OH% is the same. In other regions the prediction is good.

The NO is predecited well enough considering the dependence of the model on the temperature values.

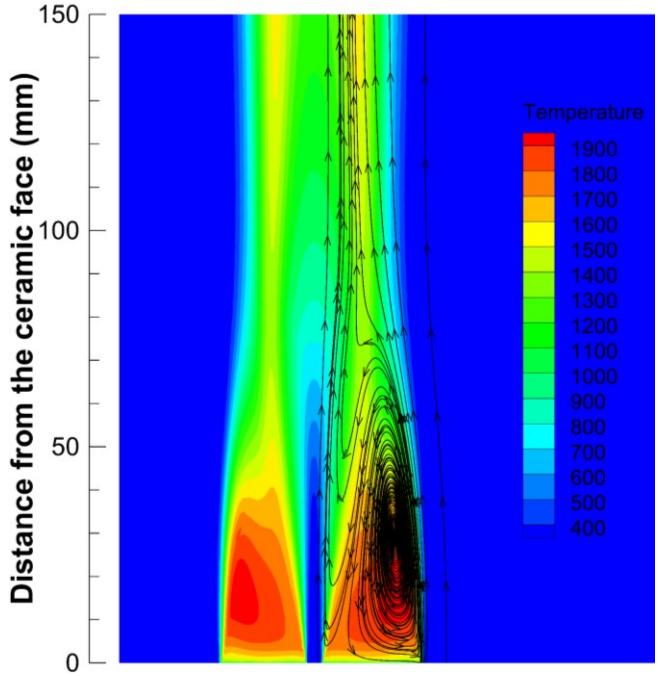

Figure 4.36 Temperature contour of the HM2 flame.

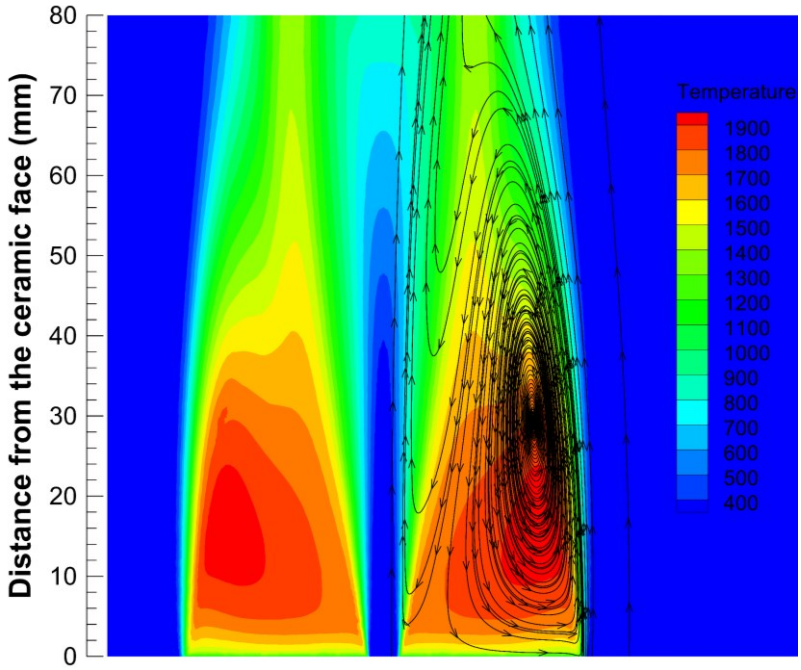

Figure 4.37 Temperature contour of the recirculation zone in HM2 flame.

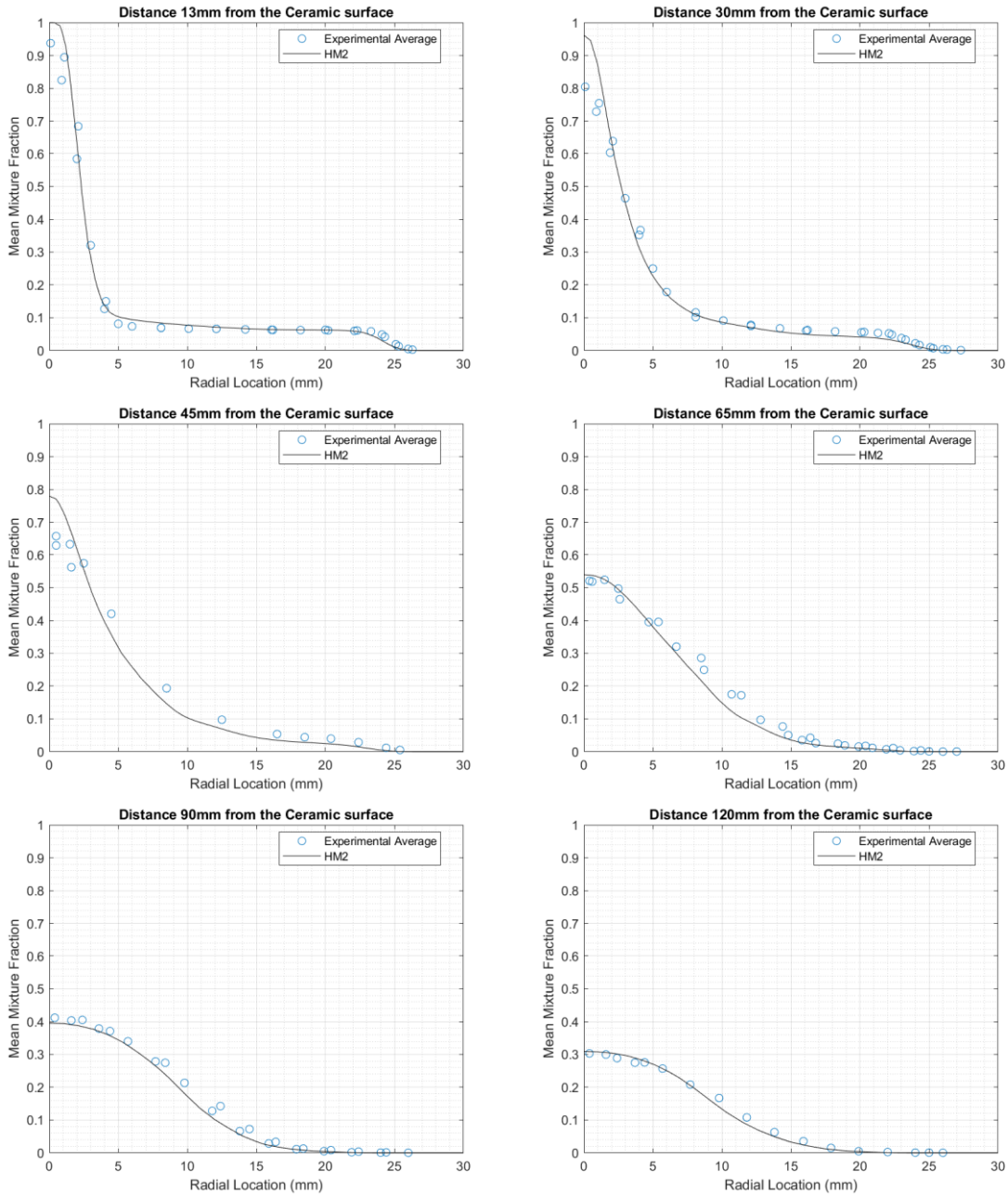

Figure 4.38 Radial profile of the mean mixture fraction in the HM2 flame.

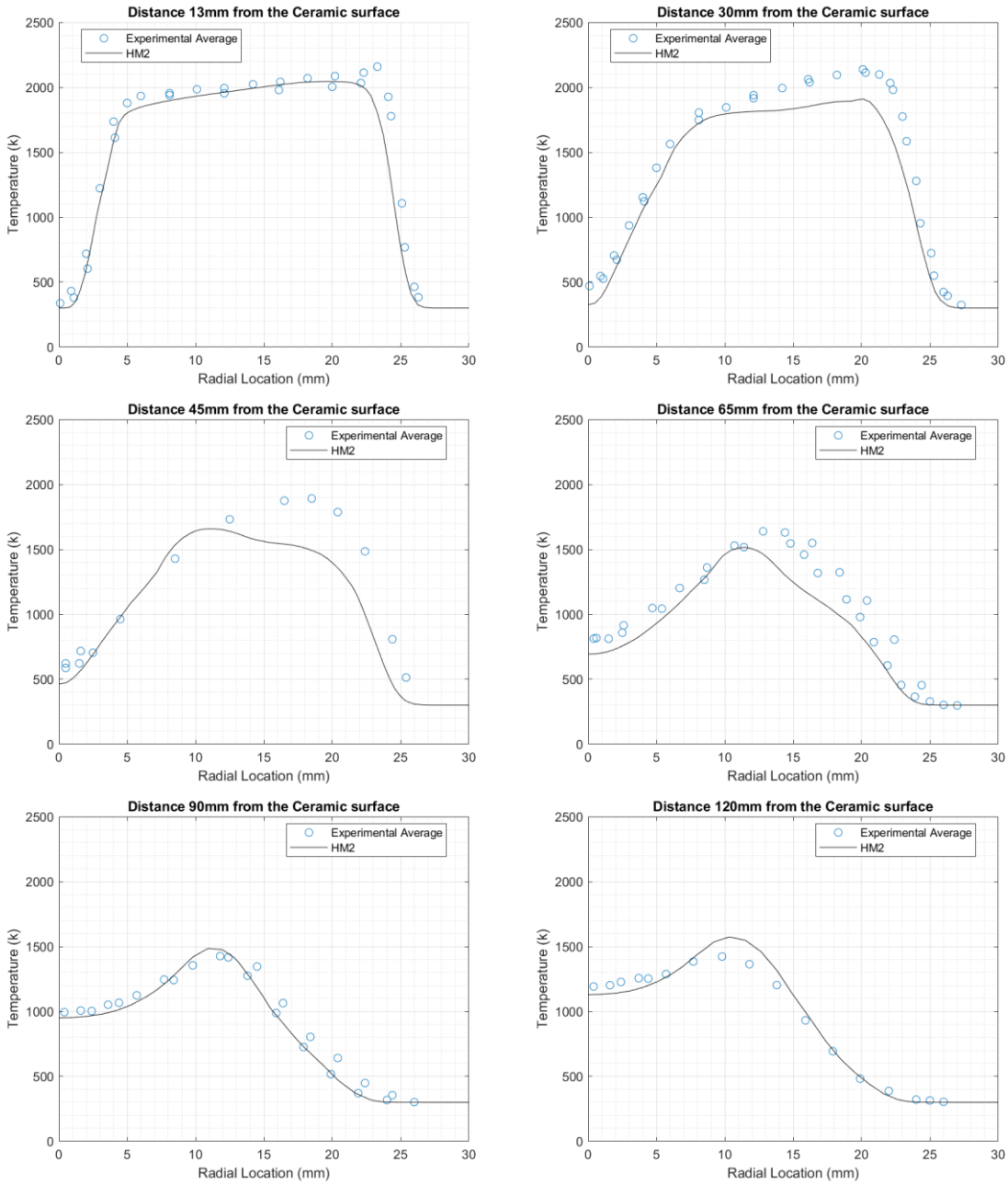

Figure 4.39 Radial profile of the temperature in the HM2 flame.

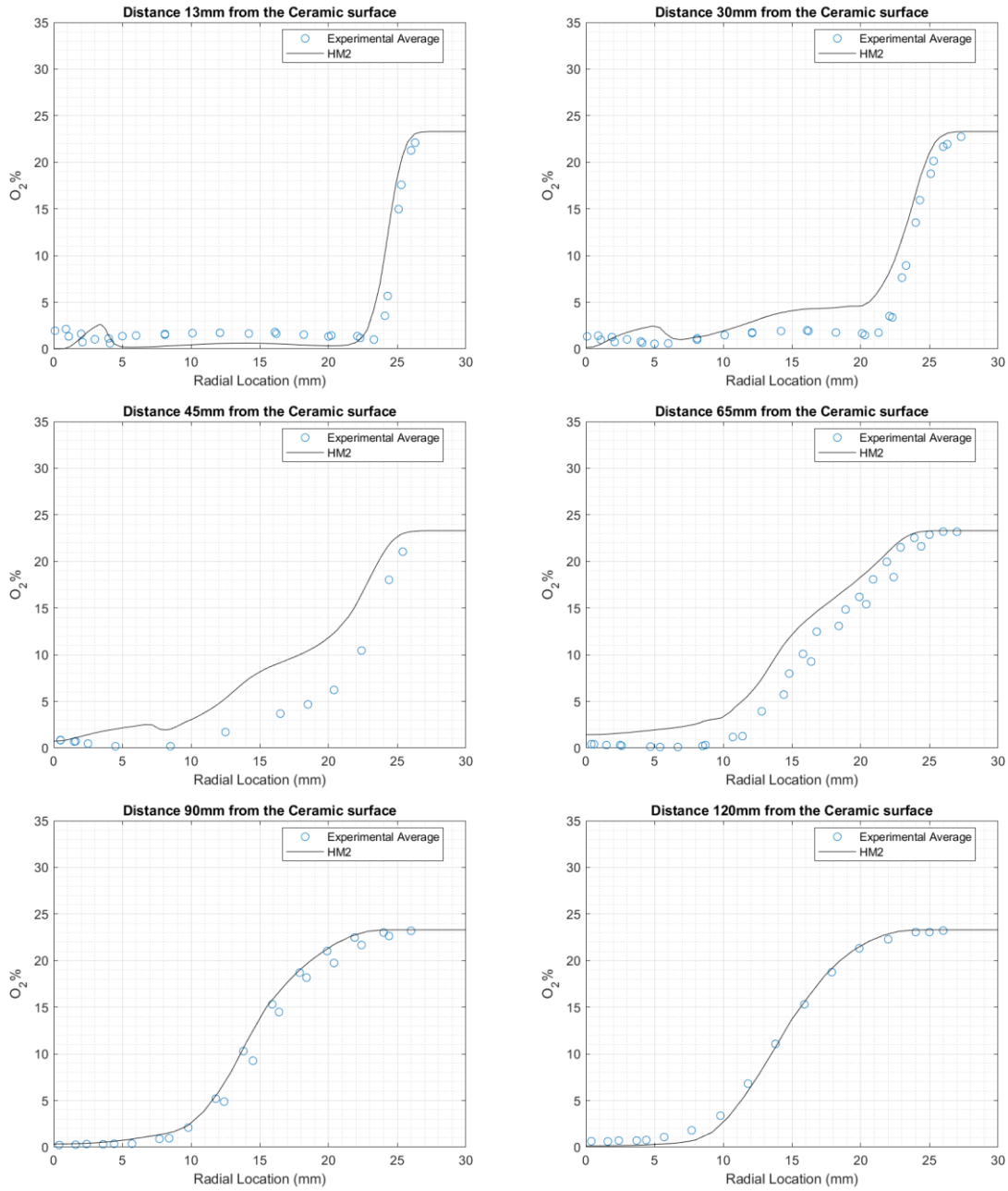

Figure 4.40 Radial profile of the O2 in the HM2 flame.

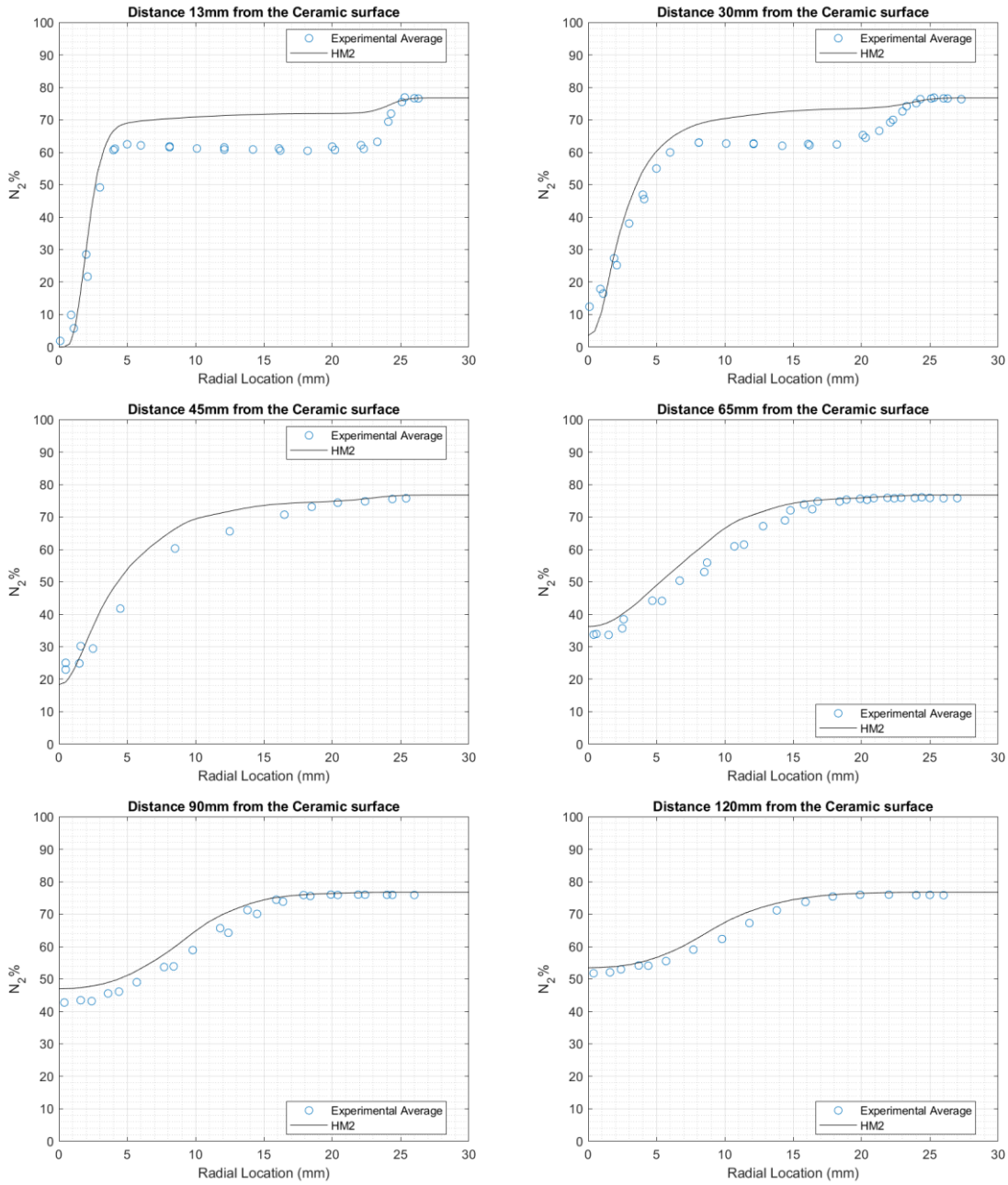

Figure 4.41 Radial profile of the N2 in the HM2 flame.

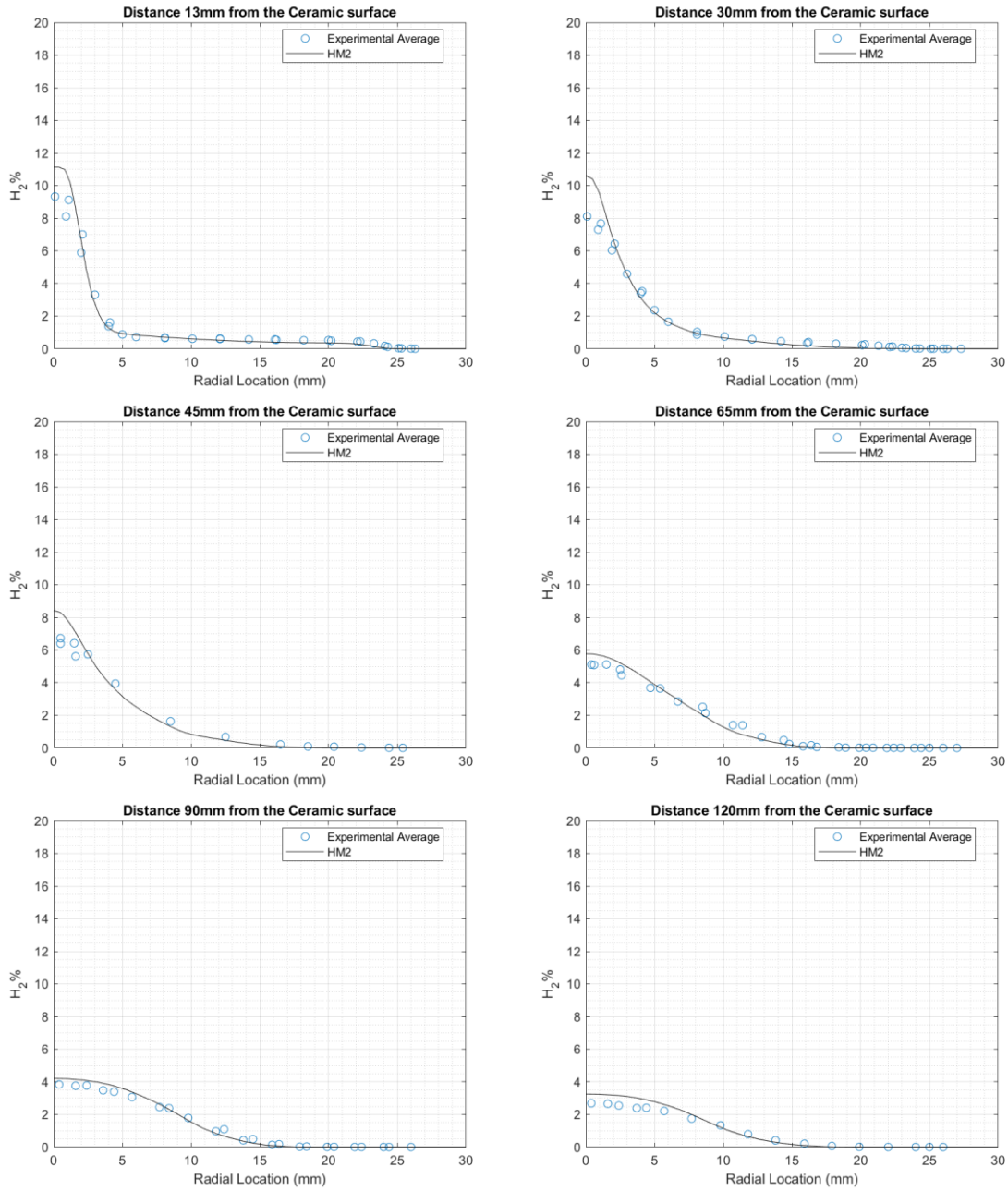

Figure 4.42 Radial profile of the H2 in the HM2 flame.

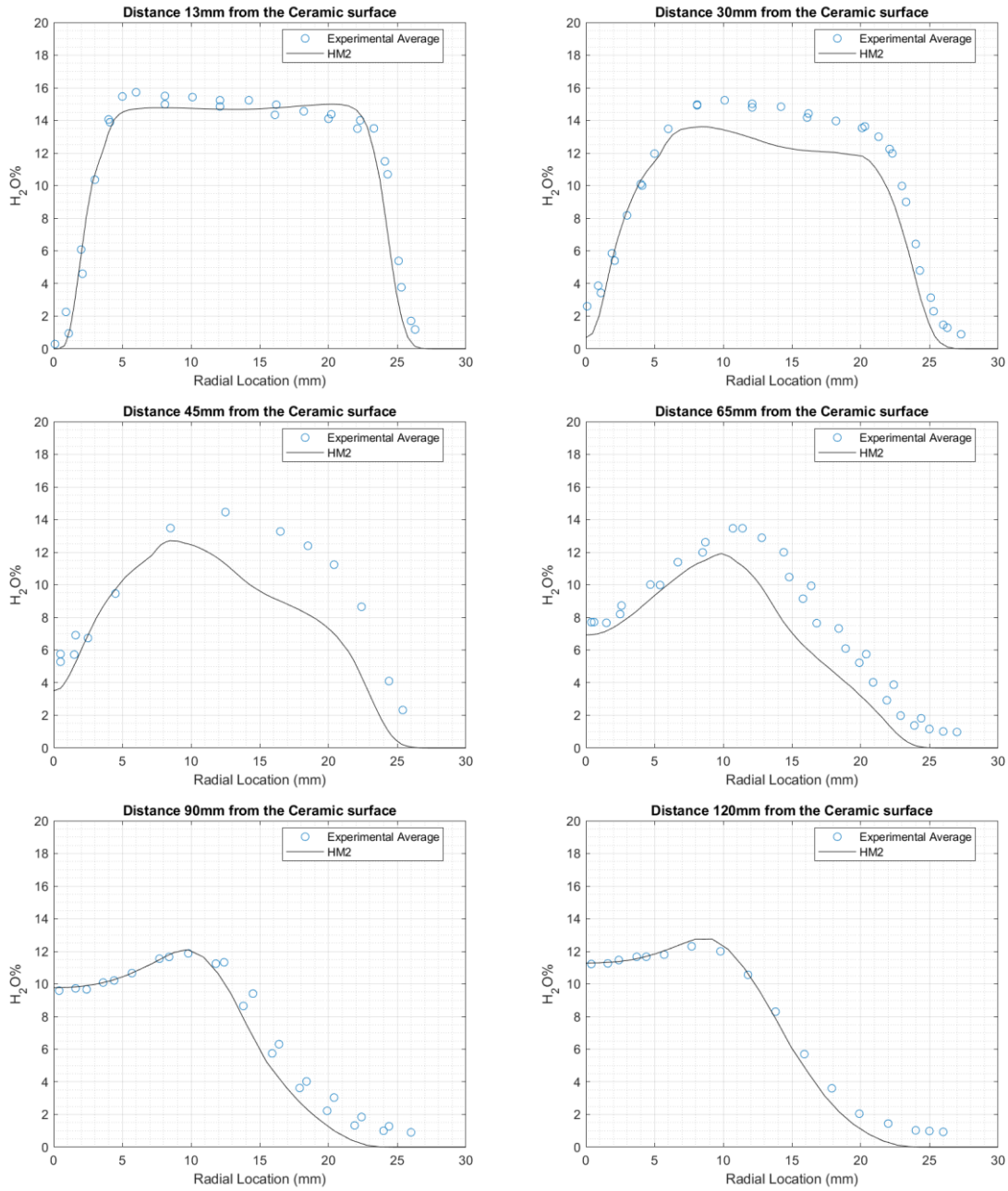

Figure 4.43 Radial profile of the H2O in the HM2 flame.

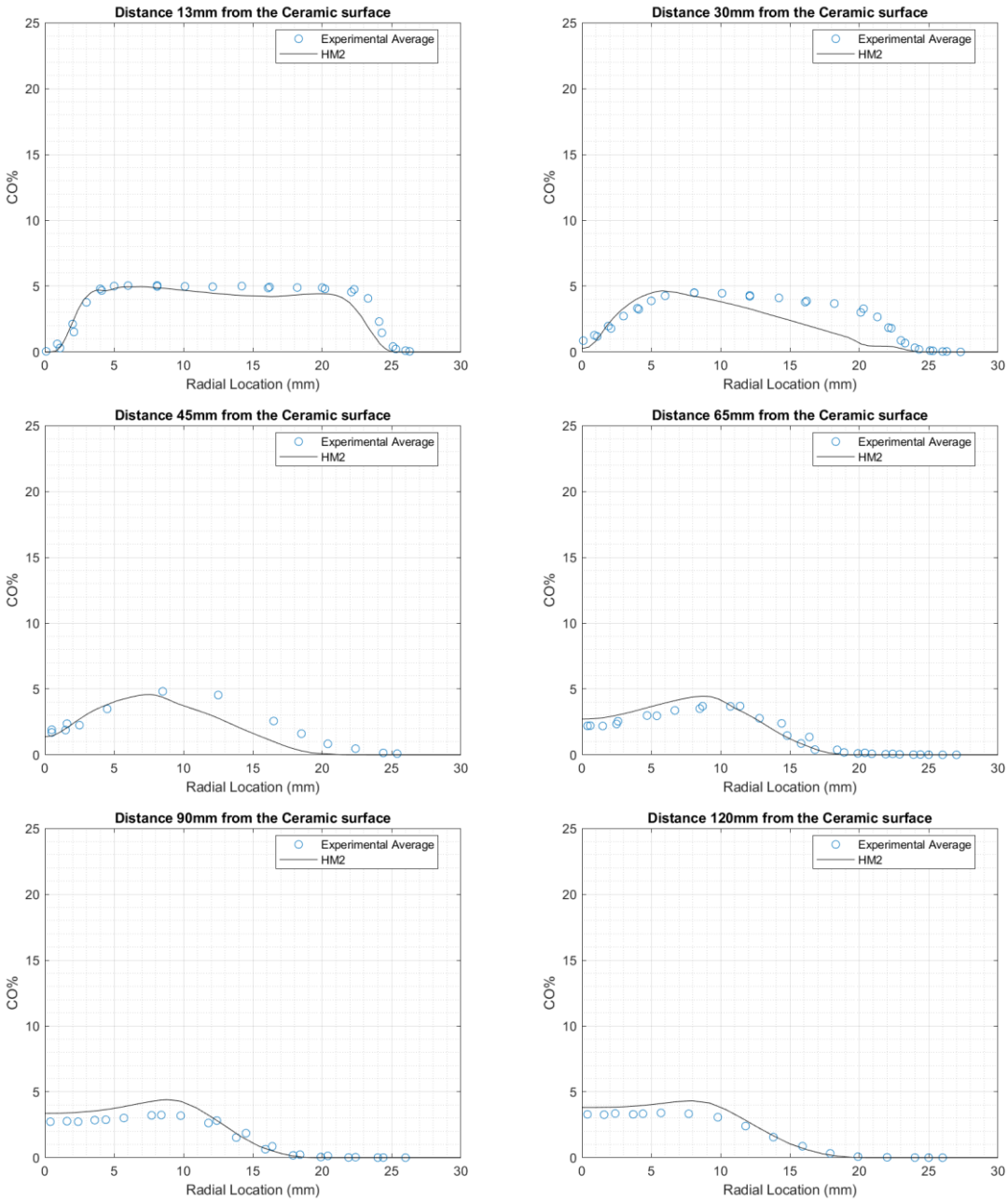

Figure 4.44 Radial profile of the CO in the HM2 flame.

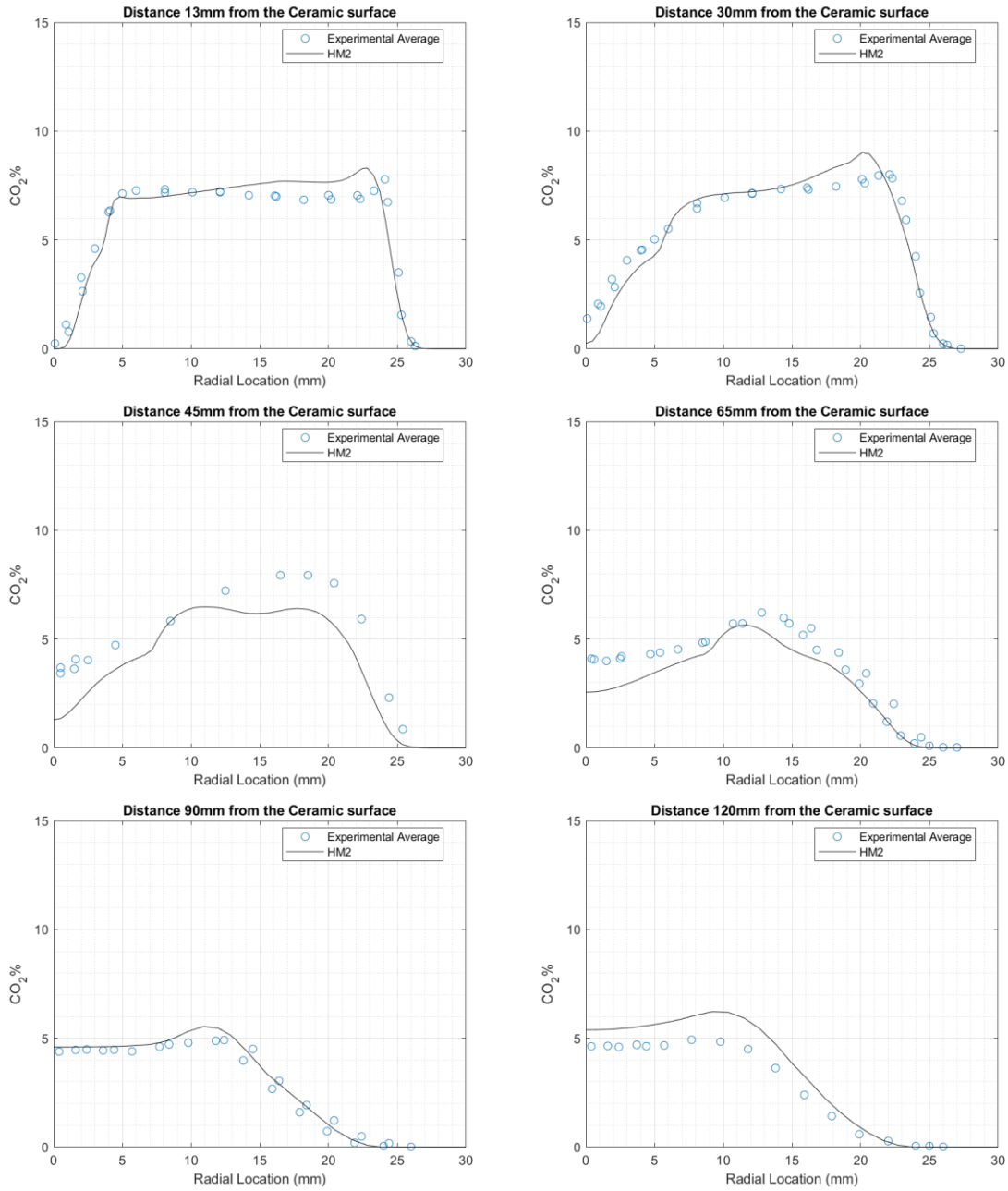

Figure 4.45 Radial profile of the CO2 in the HM2 flame.

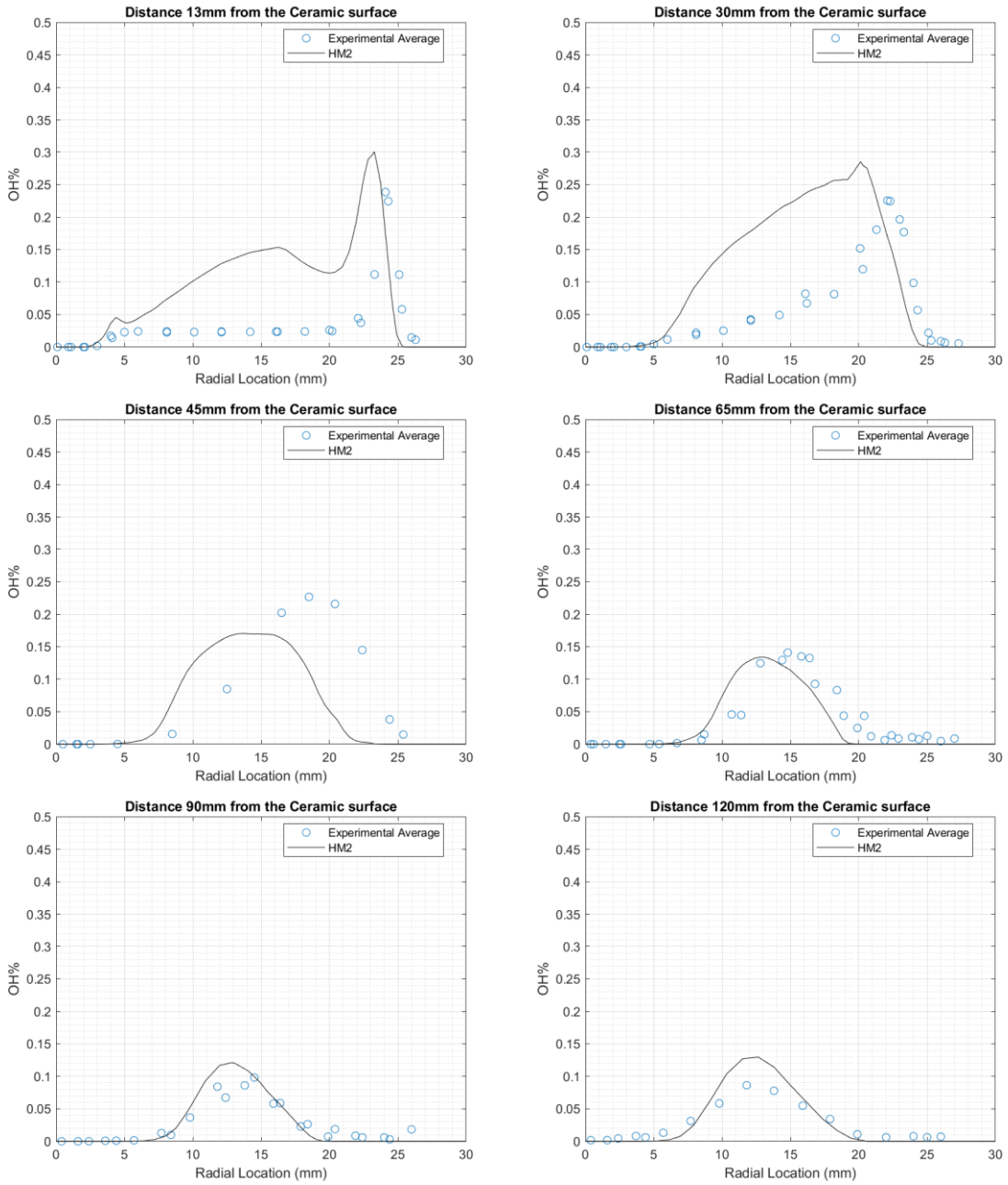

Figure 4.46 Radial profile of the OH in the HM2 flame.

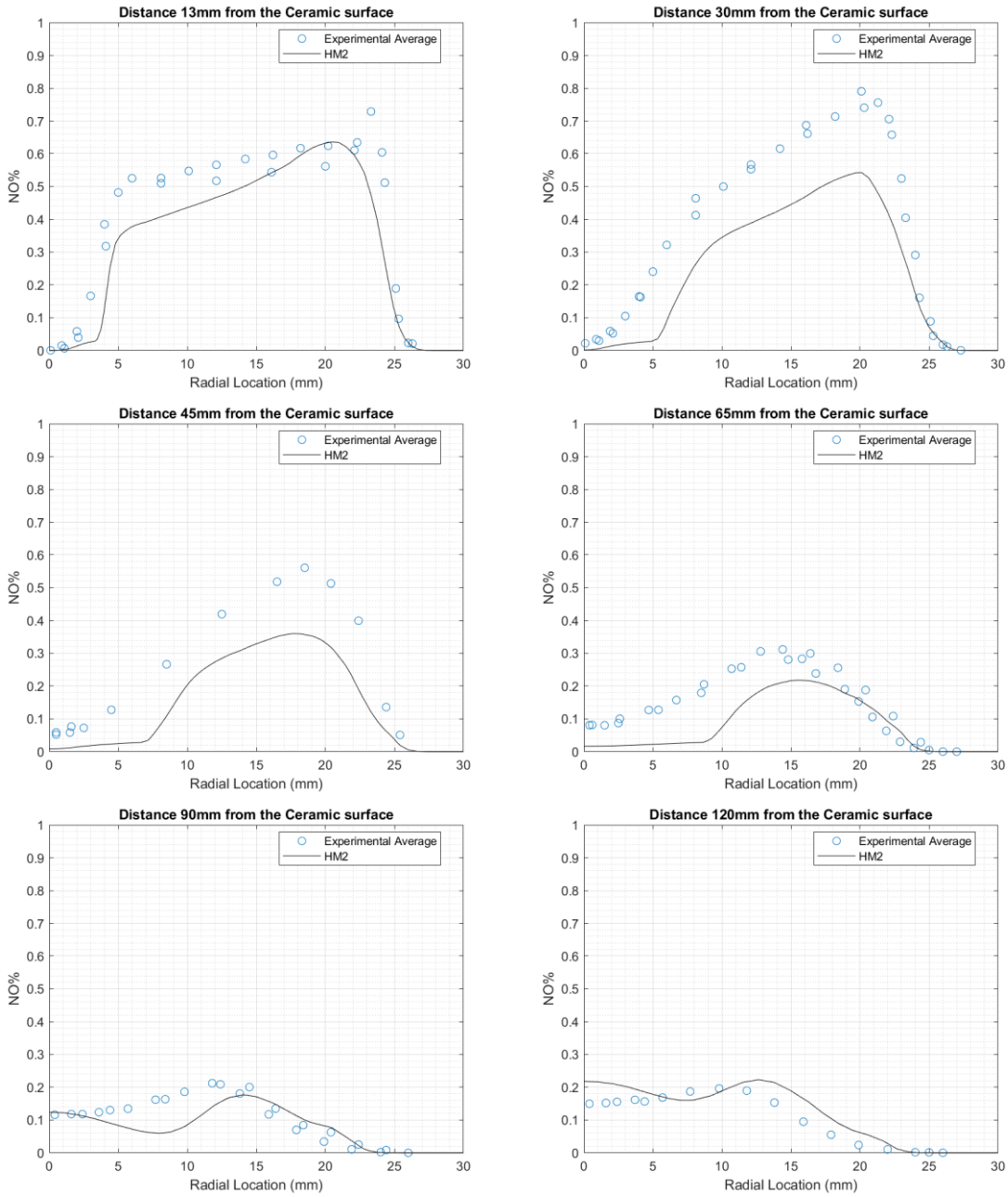

Figure 4.47 Radial profile of the NO (×100) in HM2 flame

4.9 Comparison of HM1 and HM2 flames

The comparison between these two flames by presenting the temperature contours and the streamlines shows how the jet velocity can effect the recirculation zone and the combustion.

As is evident in Figure 4.48 by increasing the jet velocity the temperature decreases in the recirculation zone. This decrease in temperature can cause local extinction which will reignite again. This is the reason behind the "puff" like sound which was observed in the experimental test.

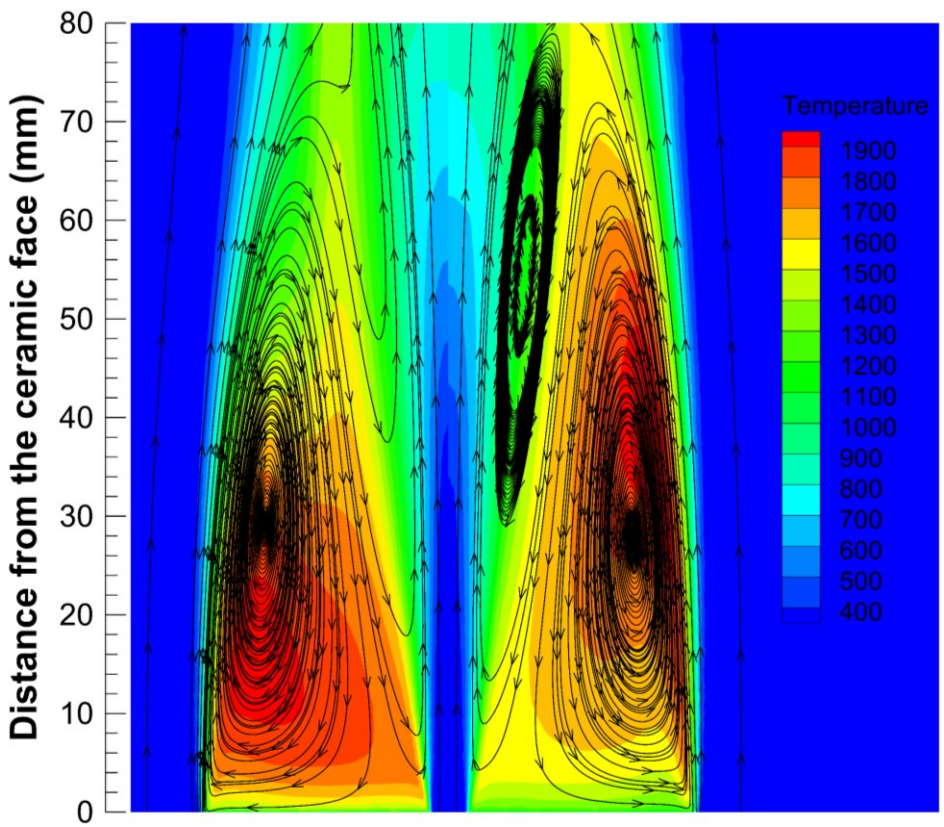

Figure 4.48 Recirculation zone. (HM2-HM1)

Comparing the results presented for both the cases are explaining how the combustion is less accurately predicted in the HM2 flame compared to HM1 flame. As it is studied by P.J.Coelho [17] suggests that the results obtained by the unsteady diffusion flamelet model are in closer agreement with experimental

measurements compared to the steady diffusion flamelet model specially in the fuel rich zone (recirculation zone).

Another study to show more in detailed this effect is suggested by F.Chitgarha [18] explains how the results are deferring by increasing the jet velocity. This study suggests that performing an unsteady calculation can predict the results very close to the measurements.

5. Conclusion and Recommendations

The initial goal of this thesis was to develop a CFD model for the non-premixed combustion and compare the results with the available experimental data to understand the effectiveness of the model in predicting the combustion for future studies related to heavy duty combustor TG20.

During this thesis work the non-premixed combustion of CH_4/H_2 is studied using different chemical models and turbulent models with different grid sizes, the following results can be drawn:

1. The grid sensitivity shows that grid sizes less than 1mm are suitable for good predictions, and the lower grid sizes in the recirculation zone are beneficial.
2. As it is suggested by the other researchers a modification of the standard $k-\epsilon$ model is necessary to predict the flow, same as this suggestion the realizable model is modified and presented a better prediction compared to previous studies.
3. Comparing the data extracted by the equilibrium and the partially in equilibrium for the species it can be said that steady diffusion flamelet model can predict the species with high accuracy in the low velocity flames compared to the high velocity flames.
4. The presented model can predict different flames as well.

As a recommendation for the future works it can be good to study the model with unsteady model to include the non-equilibrium species specially in high velocity flames, as well as performing similar studies on other fuels with different stoichiometric ratio and the kinetics.

6. Bibliography

[1] J. M. Donbar, J. F. Driscoll, and C. D. Carter, "Reaction zone structure in turbulent nonpremixed jet flames—from CH-OH PLIF images," *Combust. Flame*, vol. 122, no. 1–2, pp. 1–19, 2000.

[2] S. R. T. and Others, *Introduction to combustion*. McGraw-Hill Companies, 1996.

[3] ANSYS FLUENT, "ANSYS Fluent Theory Guide," *ANSYS Inc., USA*, vol. 15317, no. November, pp. 1–759, 2013.

[4] S. Som, P. K. Senecal, and E. Pomraning, "Comparison of RANS and LES turbulence models against constant volume diesel experiments," 2012.

[5] A. D. Canonsburg, "ANSYS Fluent Tutorial Guide," no. January, 2017.

[6] K. N. C. Bray, "Laminar flamelets in turbulent flames," *Turbul. React. flows*, 1994.

[7] M. Mansha, A. R. Saleemi, B. M. Ghauri, and N. Ramzan, "Development and testing of a detailed kinetic mechanism of natural gas combustion in internal combustion engine," *J. Nat. Gas Chem.*, vol. 19, no. 2, pp. 97–106, 2010, doi: 10.1016/S1003-9953(09)60039-6.

[8] P. Saxena and F. A. Williams, "Testing a small detailed chemical-kinetic mechanism for the combustion of hydrogen and carbon monoxide," *Combust. Flame*, vol. 145, no. 1–2, pp. 316–323, 2006, doi: 10.1016/j.combustflame.2005.10.004.

[9] and Z. Q. Gregory P. Smith, David M. Golden, Michael Frenklach, Nigel W. Moriarty, Boris Eiteneer, Mikhail Goldenberg, C. Thomas Bowman, Ronald K. Hanson, Soonho Song, William C. Gardiner, Jr., Vitali V. Lissianski, "GRI-Mech 3.0," 1999. http://www.me.berkeley.edu/gri_mech/.

[10] S. Bonturi, M. Pourkashanian, A. Williams, G. Oskam, and C. Wilson, "NOx formation in counter-flow opposed-jet diffusion CH4/air flames," *Combust.*

Sci. Technol., vol. 121, no. 1–6, pp. 217–233, 1996.

[11] A. R. Masri and R. W. Bilger, "Turbulent diffusion flames of hydrocarbon fuels stabilized on a bluff body," *Symp. Combust.*, vol. 20, no. 1, pp. 319–326, 1985, doi: 10.1016/S0082-0784(85)80517-8.

[12] "BLUFF-BODY FLOWS AND FLAMES," *The University of Sydney*. http://web.aeromech.usyd.edu.au/thermofluids/bluff.php.

[13] R. W. Dibble, A. R. Masri, and R. W. Bilger, "The spontaneous raman scattering technique applied to nonpremixed flames of methane," *Combust. Flame*, vol. 67, no. 3, pp. 189–206, 1987, doi: 10.1016/0010-2180(87)90095-2.

[14] D. A. Long, *Raman spectroscopy*. New York: McGraw-Hill International, 1977.

[15] B. B. Dally, A. R. Masri, R. S. Barlow, and G. J. Fiechtner, "Instantaneous and mean compositional structure of bluff-body stabilized nonpremixed flames," *Combust. Flame*, vol. 114, no. 1–2, pp. 119–148, 1998.

[16] M. Hossain and W. Malalasekera, "A combustion model sensitivity study for CH4/H2 bluff-body stabilized flame," *Proc. Inst. Mech. Eng. Part C J. Mech. Eng. Sci.*, vol. 221, no. 11, pp. 1377–1390, 2007, doi: 10.1243/09544062JMES336.

[17] P. J. Coelho and N. Peters, "Unsteady modelling of a piloted methane/air jet flame based on the Eulerian particle flamelet model," *Combust. Flame*, vol. 124, no. 3, pp. 444–465, 2001.

[18] F. Chitgarha and A. Mardani, "Assessment of steady and unsteady flamelet models for MILD combustion modeling," *Int. J. Hydrogen Energy*, vol. 43, no. 32, pp. 15551–15563, 2018.